THE MARTIAN ATMOSPHERIC BOUNDARY LAYER

A. Petrosyan,[1] B. Galperin,[2] S. E. Larsen,[3] S. R. Lewis,[4] A. Määttänen,[5] P. L. Read,[6] N. Renno,[7] L. P. H. T. Rogberg,[6] H. Savijärvi,[8] T. Siili,[9] A. Spiga,[4,10] A. Toigo,[11] and L. Vázquez[12]

[1]   The planetary boundary layer (PBL) represents the part of the atmosphere that is strongly influenced by the presence of the underlying surface and mediates the key interactions between the atmosphere and the surface. On Mars, this represents the lowest 10 km of the atmosphere during the daytime. This portion of the atmosphere is extremely important, both scientifically and operationally, because it is the region within which surface lander spacecraft must operate and also determines exchanges of heat, momentum, dust, water, and other tracers between surface and subsurface reservoirs and the free atmosphere. To date, this region of the atmosphere has been studied directly, by instrumented lander spacecraft, and from orbital remote sensing, though not to the extent that is necessary to fully constrain its char-acter and behavior. Current data strongly suggest that as for the Earth's PBL, classical Monin-Obukhov similarity theory applies reasonably well to the Martian PBL under most conditions, though with some intriguing differences relating to the lower atmospheric density at the Martian surface and the likely greater role of direct radiative heating of the atmosphere within the PBL itself. Most of the modeling techniques used for the PBL on Earth are also being applied to the Martian PBL, including novel uses of very high resolution large eddy simulation methods. We conclude with those aspects of the PBL that require new measurements in order to constrain models and discuss the extent to which anticipated missions to Mars in the near future will fulfill these requirements.

1. INTRODUCTION

[2]   The Martian planetary boundary layer (PBL) comprises those layers of the atmosphere closest to the surface, within which interactions between the atmosphere and the surface itself are dominant. In practice, this represents the lowest 1–10 km of the atmosphere, within which surface-driven intense convection may take place, with convective plumes and vortices rising to heights in excess of 5–10 km during the day [*Haberle et al.*, 1993a; *Larsen et al.*, 2002; *Hinson et al.*, 2008]. At night, convection is inhibited and radiative cooling produces a stably stratified layer at the surface, and the PBL reduces to a shallow layer forced by mechanical turbulence at the bottom of the stable layer. It is therefore a highly dynamic and variable region of the atmosphere at virtually all locations on Mars, with additional variability and dynamical phenomena induced by interactions with local surface topography.

[3]   The PBL is extremely important, both scientifically and operationally. It is the critical interface between the free atmosphere and the surface and regolith, mediating both short-term and long-term exchanges of heat, momentum, dust, water, and a variety of chemical tracers (such as argon and methane) between surface and subsurface and atmospheric reservoirs. It is also the region of the atmosphere through which landed and (at least potentially) airborne spacecraft need to pass through to reach their regions of operations. A clear and quantitative understanding of this part of the atmosphere, and the way in which it interacts

[1]Space Research Institute, Russian Academy of Sciences, Moscow, Russia.

[2]College of Marine Science, University of South Florida, St. Petersburg, Florida, USA.

[3]Risø National Laboratory, Technical University of Denmark, Roskilde, Denmark.

[4]Department of Physics and Astronomy, Open University, Milton Keynes, UK.

[5]LATMOS, Université de Versailles Saint Quentin, Guyancourt, France.

[6]Atmospheric, Oceanic and Planetary Physics, University of Oxford, Oxford, UK.

[7]Department of Atmospheric, Oceanic and Space Sciences, University of Michigan, Ann Arbor, Michigan, USA.

[8]Department of Physics, University of Helsinki, Helsinki, Finland.

[9]Earth Observation Division, Finnish Meteorological Institute, Helsinki, Finland.

[10]LMD, Université Pierre et Marie Curie, Paris, France.

[11]Johns Hopkins University Applied Physics Laboratory, Laurel, Maryland, USA.

[12]Departamento de Matemática Aplicada, Facultad de Informática, Universidad Complutense de Madrid, Madrid, Spain.

with the surface and free atmosphere, should therefore be a vital part of any program to explore and understand the past, present, and future Martian environment. Such an understanding will also enable reliable predictions to be made of environmental conditions encountered during spacecraft entries and operations, which are essential for mission safety and efficient design.

[4] At the present time, our understanding of the Martian PBL and ability to model it are strongly guided and influenced by studies of its terrestrial counterpart [*Larsen et al.*, 2002]. While this may be a valid initial approach, the Martian environment differs from that of the Earth in a number of important aspects. The much lower atmospheric pressure at the Martian surface may be significant, especially within the thin surface layer, affecting the details of heat, momentum, and mass fluxes. The range of conditions encountered in the Martian PBL may also be substantially more extreme than found typically on Earth, with diurnal contrasts from intensely convective conditions, accompanied by sustained superadiabatic thermal gradients, to very strongly stably stratified conditions during the night. Such widespread and extreme variability across the entire planet places extraordinary demands on predictive models to capture accurately and to compute implied vertical transports of heat, momentum, and tracers.

[5] This aspect of Martian atmospheric science has been comparatively neglected in recent exploration activities. One of the main sources of information on the Martian PBL continues to be the multiannual series of measurements from the Viking landers in the 1970s. The quality and consistency of these data sets have scarcely been superseded by any subsequent lander mission in recent years. The recent Mars Exploration Rovers (MERs) Spirit and Opportunity were not even equipped with the most basic of meteorological instrumentation to measure atmospheric parameters in situ, although the Miniature Thermal Emission Spectrometer (Mini-TES) remote sensing instrument has provided valuable information on low-level thermal structures in the PBL [*Smith et al.*, 2004, 2006]. In the context of the paucity of in situ observations, recent remote sensing measurements have therefore been a welcome complement. Of notable interest in this context are the recent estimates of boundary layer depth in various regions of Mars through radio occultations (ROs) on board Mars Express [*Hinson et al.*, 2008].

[6] In this paper, we provide an overview of the Martian PBL, covering the basic theory underlying the physics of atmospheric boundary layers, including how the boundary layers of Mars and the Earth are similar in some respects but differ in others, together with a reasonably comprehensive treatment of the body of observations available to characterize the PBL and the methods used to model it. Section 2 provides a short introduction to the basic concepts underlying boundary layer theory. Section 3 goes on to examine the key similarities and differences between the boundary layers on Mars and the Earth, introducing the critical parameters that determine them. Section 4 provides a detailed discussion of the body of observations that inform our knowledge of the Martian PBL. Section 5 surveys the

approaches used to capture the behavior of the Martian PBL in models, ranging in sophistication from simple conceptual models, based on bulk formulations of turbulent transports of heat and momentum, to more complex treatments of parameterized Reynolds stress and ultimately to large eddy simulation (LES) approaches. Section 6 considers the overall role of the PBL on Mars in the wider global circulation, including its role as interface between atmosphere and surface in moderating sources of atmospheric water vapor, dust, and other material tracers. Some concluding discussion and a summary of the paper is provided in section 7, including a consideration of where currently available observational information is inadequate and with some discussion of possible options for future measurements.

2. ATMOSPHERIC BOUNDARY LAYER PHYSICS

[7] The boundary layer is one of the key subdomains of the troposphere on Earth, where it has a thickness of order 1 km. Within this layer, the meteorological fields, such as wind velocity and temperature, adjust from their values in the free atmosphere toward values and spatial gradients determined by the surface (e.g., see Figure 1). For the Earth (though not necessarily for Mars; see sections 3 and 5), the heat transfer within this layer is directly related to the solar insolation at the planetary surface and may be carried via both sensible and latent heat fluxes. The momentum transfer in this layer is primarily due to drag forces acting on the free atmospheric motions as a result of the presence of the solid planetary surface. The proximity of the surface initiates mechanical and/or thermal instabilities that enhance the vertical transport and mixing in the boundary layer by the action of the ensuing turbulent motions. The resulting convective plumes and turbulent eddies transport momentum and trace species, mixing these quantities within the PBL. The sources of these instabilities are the vertical shear of the horizontal wind and the surface heating that produce turbulence via shear and convective instabilities, respectively. In this section, we discuss various types of boundary layers and their characteristics, along with terminology used in boundary layer meteorology.

[8] Generally, planetary atmospheric boundary layers can be divided into a number of different subregions, as indicated in Figure 1. Closest to the ground is the so-called "surface layer" defined by its proximity to the surface, i.e., $z/h \leq 0.1$, see Figure 1; here z is the vertical coordinate directed upward and h is the boundary layer height. In the surface layer, the vertical fluxes of heat and momentum are almost independent of height and vary by less than 10% of their mean magnitudes [*Monin and Yaglom*, 1975; *Stull*, 1988]. Above this layer is the bulk of the boundary layer, known as the "mixed layer," where strong mixing may take place up to the top of the boundary layer, which is typically characterized by a jump, $\Delta\Theta$, in potential temperature toward the free atmosphere. This jump is often not discontinuous but forms an "entrainment zone," within which mixing from below rapidly decays as air from the free atmosphere is entrained into the underlying flow. This
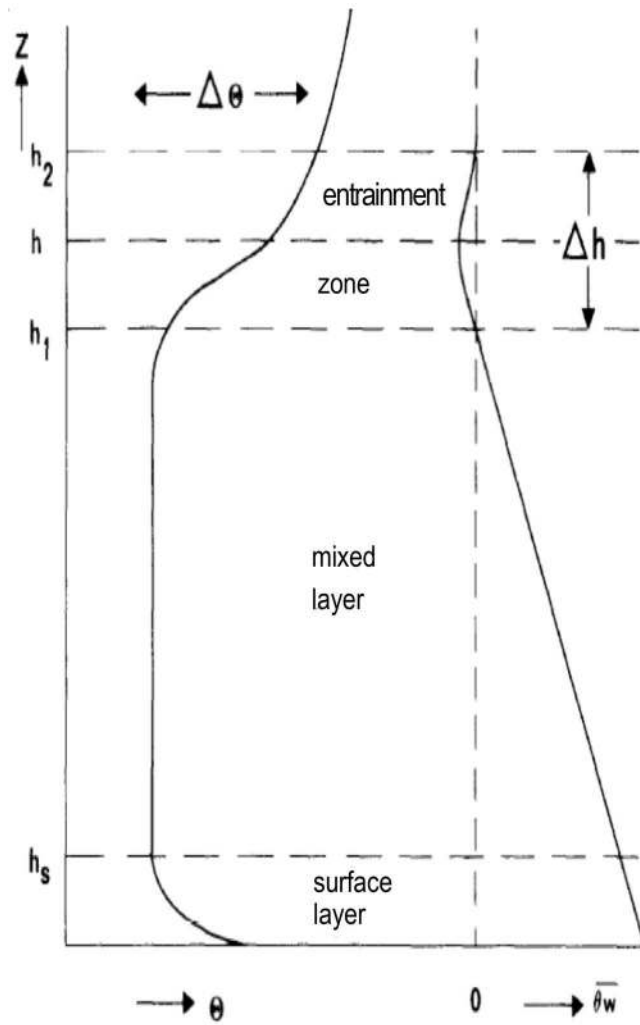
Figure 1. Schematic structure of the daytime convective planetary boundary layer.

region may also be characterized by a weak reversal in the upward heat flux known as the "countergradient diffusion" [*Deardorff*, 1972; *Holtslag and Moeng*, 1991].

[9] One of the most important and popular tools for the study of turbulence is dimensional analysis based upon dimensionless parameters defined in terms of velocity, length, and time scales that characterize the two basic mechanisms for turbulence production: shear and buoyancy. These dimensionless parameters define flow regimes in planetary boundary layers that are dominated by the presence of various turbulent processes (see, e.g., *Monin and Yaglom* [1975], *Garratt* [1992], *Stull* [1988], *Tennekes and Lumley* [1972], and *Wyngaard* [2010] for detailed reviews).

[10] For simplicity, we only consider a stationary and homogeneous boundary layer. For characterization of its structure and dynamics, we introduce the following parameters: the geostrophic wind G in the free atmosphere ($z > h_2$; see Figure 1); the corresponding thermal wind shear, dG/dz; the temperature jump $\Delta\Theta$ at the top of an unstable boundary layer (or entrainment zone, see Figure 1); the temperature gradient, $\gamma = d\Theta/dz$, in the free atmosphere above the boundary layer; the Coriolis parameter, $f = 2\Omega\sin\phi$, where Ω

is the angular velocity of planetary rotation and ϕ is the latitude; the buoyancy parameter, g/θ_0, with g being the acceleration due to gravity; the roughness length, z_0; the reference temperature, θ_0, and the vertical turbulent heat flux at the surface, H_0. All these parameters are related to the phenomena that generate turbulence in the boundary layer.

[11] When turbulence is produced by shear, it is convenient to introduce a velocity scale, u_*, related to the shear stress, τ_{s0}, at the surface, known as the friction velocity:

$$u_* = \sqrt{\frac{\tau_{s0}}{\rho_0}}, \tag{1}$$

where ρ_0 is the density of the air at the ground (note that quantities with the subscript "0" refer to values at the surface).

[12] When turbulence is produced by buoyancy due to an upward sensible heat flux imposed at the planet's surface, the covariance between vertical velocity and temperature fluctuations, w' and θ', respectively, taken at the surface, determines the surface heat flux, H_0,

$$-\left(\overline{w'\theta'}\right)_0 = \frac{H_0}{\rho_0 c_p}, \tag{2}$$

where c_p is the specific heat capacity of the air at constant pressure and the minus sign denotes that the surface is losing energy to the atmosphere. This parameter is often used to scale the intensity of turbulence [*Monin and Obukhov*, 1954]. We also define a length scale known as the Monin-Obukhov length scale, L,

$$L = -u_*^3 \Big/ \left(\kappa \frac{g}{\theta_0} \left(\overline{w'\theta'}\right)_0\right), \tag{3}$$

where κ is the von Kármán constant usually taken equal to 0.4. The overbar in equations (2) and (3) indicates an ensemble mean value and the prime indicates turbulent fluctuations. Note that L is positive for stable stratification and negative for unstable conditions.

[13] Other appropriate length scales can also be introduced. Recalling that h is the depth of the turbulent layer above the surface and z denotes the height above the surface, we now have three length scales that provide two independent dimensionless combinations: z/h is the location of the point of interest within the boundary layer, and $h/|L|$ represents a stability parameter that is smaller than 1 when shear production dominates and greater than 1 when turbulence is primarily due to buoyant convection.

[14] To characterize the boundary layer dynamics, we also need to introduce time scales that characterize nonstationary processes: (1) T_f, the time scale of external processes that act upon the boundary layer; (2) T_m, the time scale for the development of mean velocity and temperature profiles; (3) $T_t = \ell/U$, the time scale characteristic of the large-scale eddies (here ℓ and U represent length and velocity scales for the macroscopic structure of turbulence); and (4) T_p, the time scale of turbulence production processes.

[15] Note that u_*, L, and z alone define the scaling structure of the surface layer via the Monin-Obukhov flux-gradient

relationships for mean velocity and temperature, which can be written as

$$\Phi_m\left(\frac{z}{L}\right) = \frac{\kappa z}{u_*}\frac{d\overline{u}}{dz}, \tag{4}$$

$$\Phi_h\left(\frac{z}{L}\right) = Pr_t\frac{\kappa z}{\theta_*}\frac{d\overline{\Theta}}{dz}, \tag{5}$$

where θ_* is defined by

$$\left(\overline{w'\theta'}\right)_0 = u_*\theta_* \tag{6}$$

and Pr_t is the turbulent Prandtl number in neutrally stratified flows. These functional expressions relate Φ_m and Φ_h to the eddy viscosity and eddy diffusivity when used in the simplest closure models for the Reynolds-averaged boundary layer equations (see section 5.2). They lead to the logarithmic flux profile relationships for velocity and temperature:

$$\left(\frac{\overline{u}}{u_*}\right) = \frac{1}{\kappa}\ln\left(\frac{z}{z_0}\right), \tag{7}$$

$$\left(\frac{\overline{\Theta}}{\theta_*}\right) = \frac{Pr_t}{\kappa}\ln\left(\frac{z}{z_{0T}}\right), \tag{8}$$

that govern the surface layer. Here z_0 is a roughness length that characterizes the inhomogeneity of the surface for the momentum transfer, z_{0T} is an equivalent characteristic for the heat transfer, and $\overline{\Theta} = \Theta - \theta_0$. Equations (7) and (8) indicate that z_0 and z_{0T} are the heights above the surface at which $\overline{u}$ and $\overline{\Theta}$, respectively, go to zero. Generally, z_0 and z_{0T} are not equal.

[16] We shall treat separately each of the hypotheses required in order to use surface layer similarity theory on Mars. The complexity of the terrain, along with large-scale meteorological phenomena (synoptic perturbations), can greatly alter horizontal homogeneity. However, synoptic perturbations are not usually present at some locations and times of the year (such as midlatitude northern summertime), and some sites, such as those for the Pathfinder and Viking missions, although not especially flat, did not present much in the way of sharp topography [*Golombek et al.*, 1997].

[17] On the other hand, molecular exchanges are 2 orders of magnitude weaker than turbulent diffusion in the first few meters [*Martínez et al.*, 2009], which allows us to neglect molecular diffusion in the surface layer. Moreover, the height of the surface layer and the magnitude of the Coriolis force are found to be of the same order on Mars as on Earth, and consequently Coriolis forces can be neglected in both cases.

[18] Concerning suspended dust, similarity theory takes no account of this peculiarly Martian phenomenon (in that none of the independent variables takes any direct account of dust). Nevertheless, the observed dustiness is usually low [*Savijärvi*, 1999] in midlatitude locations during northern summertime, and thus the importance of the dust becomes reduced anyway. Suspended dust may be important, however, for the Martian boundary layer in complex terrains [*Karelsky and Petrosyan*, 1995; *Karelsky et al.*, 2007],

which may have significant implications for the validity of classical similarity theory.

[19] The portion of the boundary layer above the surface layer may be characterized by one of three cases: the neutral, convective, or stable boundary layers. For the neutral boundary layer, the heat flux at the surface is close to zero $((\overline{w'\theta'})_0 \simeq 0)$ and buoyancy forces play no significant role, so that u_*, h, and z are the appropriate scaling parameters.

[20] The competition between shear and buoyancy effects is commonly characterized by the dimensionless Richardson number, which is a measure of hydrodynamic stability that depends on the current vertical gradients of temperature and wind speed. It is generically defined as

$$Ri = \frac{N^2}{S^2}, \tag{9}$$

where N is the Brunt-Vaïsälä frequency ($N^2 = \beta g\partial\Theta/\partial z$; β is the thermal expansion coefficient), measuring the strength of static stability, and S is a measure of the mean vertical shear of the horizontal flow. Small ($\leq O(1)$) or negative values of Ri are often regarded as indicating the likelihood of turbulence generation via instability (either through shear-dominated or buoyancy-dominated processes, though see *Galperin et al.* [2007] and section 5.1.2 for further discussion) while larger (positive) values of Ri are associated with intermittent turbulence. For some purposes, it is also useful to introduce a "fluctuation" Richardson number,

$$Ri' = \frac{g|\theta'|\ell}{\theta_0 u_*^2}, \tag{10}$$

which defines the ratio of the acceleration due to a temperature fluctuation, θ', to the turbulent acceleration, u_*^2/ℓ. For large fluctuation Richardson numbers, the buoyancy production process is dominant and the boundary layer flow consists of discrete ascending thermals or plumes for which h, w_*, and z are scaling parameters.

[21] In the convective boundary layer, the convective velocity scale, w_*, is defined as

$$w_* = \left(\frac{g}{\theta_0}\left(\overline{w'\theta'}\right)_0 h\right)^{1/3}. \tag{11}$$

The mixed layer scalings for a convective boundary layer are:

$$\frac{\sigma_w}{w_*} \equiv \frac{\left(\overline{w'^2}\right)^{1/2}}{w_*} = \Phi_w\left(\frac{z}{h}\right), \tag{12}$$

$$\frac{\sigma_u}{w_*} \equiv \frac{\left(\overline{u'^2}\right)^{1/2}}{w_*} = \Phi_u\left(\frac{z}{h}\right), \tag{13}$$

$$\frac{\sigma_\theta}{\theta_*} \equiv \frac{\left(\overline{\theta'^2}\right)^{1/2}}{\theta_*} = \Phi_\theta\left(\frac{z}{h}\right), \tag{14}$$

where σ_w, σ_u, and σ_θ represent the characteristic scales for the standard deviations of vertical velocity, w, horizontal velocity, u, and temperature, θ, respectively; the temperature

scale, θ_*, is defined as $\theta_* = \overline{(w'\theta')}_0/w_*$. $(\Phi_w, \Phi_u, \Phi_\theta)$ represent dimensionless universal functions of z/h that determine the vertical structure of each quantity.

[22] As for the surface layer, the complexity of the Mars terrain, together with other large-scale phenomena (synoptic perturbations), can greatly alter horizontal homogeneity in the convective mixed layer. Thus, we must be certain to apply this theory only under those circumstances where the flow is sufficiently homogeneous in the horizontal direction.

[23] Along with horizontal homogeneity and stationarity, the other main hypotheses that must be satisfied when applying convective mixed layer similarity theory are (1) convection is the dominant heating mechanism throughout the mixed layer and (2) surface stress effects become negligible throughout this layer. This is certainly so on Earth under fair weather conditions [André et al., 1978], because the heating rate due to radiation convergence within the boundary layer is negligible, and the winds are light under the aforementioned conditions. On Mars, however, special care must be taken, since this may not always be the case.

[24] There is no uncertainty in neglecting the effects of surface stress throughout the bulk of the Martian convective mixed layer when the winds are calm (especially during low-latitude and midlatitude northern summertime). A problem may arise with the radiative heating throughout the Martian convective mixed layer, however, which now becomes nonnegligible because of the longwave radiative heating (in a mostly CO_2 atmosphere) and also because of the direct absorption of solar radiation by dust (see section 5.2).

[25] Under stable conditions, shear production is the only significant source of turbulence and so $\overline{(w'\theta')}_0$, τ_s/ρ_0 and z are appropriate scaling parameters. Along with the conventional Monin-Obukhov length scale defined by equation (3), such flows can also be characterized by a local Monin-Obukhov length scale,

$$\Lambda = -(\tau_s/\rho_0)^{3/2}/\kappa \frac{g}{\theta_0}\overline{w'\theta'}, \qquad (15)$$

where τ_s and $\overline{w'\theta'}$ are z dependent [Nieuwstadt, 1984].

[26] The gradient Richardson number is another important scaling parameter for stable boundary layers, providing an additional measure of static stability; it is defined as

$$Ri_g = \frac{g}{\theta_0}\frac{\partial\overline{\Theta}}{\partial z}\bigg/\left(\frac{\partial\overline{u}}{\partial z}\right)^2. \qquad (16)$$

This parameter provides an indication of the relative importance of shear production compared with buoyancy effects with the shear production dominating for numerically small values of Ri_g and buoyancy effects being stronger for numerically large (positive) values of Ri_g.

[27] The Reynolds number, $Re = U\ell/\nu$, is frequently used as a measure of the complexity and degree of turbulence in fluid dynamics. Here, as before, U is a characteristic velocity scale, ν is the kinematic viscosity of the air, and ℓ is a characteristic length scale. When Re exceeds a certain limiting value (typically $\gtrsim 2000$), the flow is likely to become turbulent, and the intensity of turbulence increases with increasing Re.

[28] If viscous dissipation is relatively weak, turbulence kinetic energy (TKE) is freely exchanged between different length scales, systematically cascading energy toward smaller scales over a range of scales known as the inertial subrange. Within this interval, the energy spectrum adopts a self-similar form known as the Kolmogorov law [Tennekes and Lumley, 1972; Pope, 2005],

$$E(k) = \alpha_1\varepsilon^{2/3}k^{-5/3}, \qquad (17)$$

where ϵ is the turbulence energy dissipation rate and α_1 is a dimensionless constant known as the Kolmogorov constant, whose value has been experimentally estimated to be $\alpha_1 = 1.5 \pm 0.15$ [Sreenivasan, 1995]. At the largest scales, the limit of the inertial subrange is governed by the scale of shear production, which may be of the order of the domain (or, in the case of the PBL, typically the height of the measurement above the surface). At the smallest scales, the inertial subrange is limited by the scales at which viscous dissipation becomes significant. The latter is characterized by the Kolmogorov scale of viscous dissipation, η, given by

$$\eta = (\nu^3/\epsilon)^{1/4} \approx \left(\kappa z\nu^3/u_*^3\right)^{1/4}, \qquad (18)$$

where the near-ground approximation of the turbulent dissipation has been used,

$$\epsilon \approx u_*^3/(\kappa z). \qquad (19)$$

Taking the scale for surface layer shear production as κz, we express the ratio of the scales of the shear production and the dissipation in terms of the Reynolds number Re_l,

$$\frac{\kappa z}{\eta} = (\kappa Re_l)^{3/4}, \qquad (20)$$

where

$$Re_l = \frac{u_*z}{\nu}. \qquad (21)$$

[29] Close to the surface, the value of ν may determine the conditions for rough or smooth (laminar) flow. These conditions are often formulated in terms of yet another Reynolds number, the roughness Reynolds number,

$$Re_0 = u_*z_0/\nu. \qquad (22)$$

The transition between rough and smooth flow is generally taken to occur for Re_0 around 2–3 [Brutsaert, 1982].

[30] If an object in the flow is small enough, one can use a Knudsen number, Kn, to account for the molecular characteristics of the gas in its interaction with the object. This dimensionless number is defined as

$$Kn = \lambda_f/D, \qquad (23)$$

where λ_f is the mean free path of the molecules and D is a characteristic length scale for the object or process in

question. For $Kn \lesssim 0.1$, the gas can effectively be considered a continuous medium. For $Kn \gtrsim 0.1$, however, the interaction is first considered as a slip flow, changing to a free molecular interaction for $Kn > 1$. In the Earth's boundary layer, $\lambda_f \sim 70$ nm, and so consideration of slip effects is only necessary for the smallest objects (e.g., small aerosols). On Mars, however, $\lambda_f \sim 5$–10 μm and a much larger fraction of the aerosol spectra effectively moves in a slip flow [cf. *Newman et al.*, 2002a].

3. OVERVIEW AND COMPARISON OF EARTH AND MARS PBLS

[31] To a large extent, the description and modeling of the Martian atmospheric boundary layer is similar to the corresponding description and modeling of the Earth's atmospheric boundary layer, both with respect to numerical modeling and to the different scaling laws. In spite of the success of the approach of using Earth-based formulations, it is useful to summarize characteristic similarities and differences between atmospheric boundary layers of the two planets. These differences almost all derive from the differences in density, where the surface pressure of the Martian atmosphere compares well with a good technological vacuum at about 500 Pascal. See Table 1 for summary of Earth and Mars values of parameters used to describe a planetary atmosphere.

[32] The low density of the Martian atmosphere means that it plays a much smaller role in the heat budget of the ground than on Earth. Compared to radiative terms, the sensible heat flux appears negligible in the surface energy budget (see Figure 2). The Martian surface temperature is therefore essentially derived from an equilibrium between the radiative terms and the soil heat conduction [*Savijärvi and Kauhanen*, 2008]. Lacking the moderating influence of the atmosphere, the diurnal variation of the surface temperature tends to be larger than on Earth, though not orders of magnitude greater. Dust storms constitute an exception to the above statement. Here the atmosphere on Mars does indeed influence the surface heat budget [*Larsen et al.*, 2002; *Määttänen and Savijärvi*, 2004].

[33] While the atmosphere on Mars generally plays a small role for the heat budget of the surface, the opposite is not true. Heat transfer between the atmosphere and the surface is the main driver of the thermal structure of the atmospheric boundary layer, driving the atmosphere into stronger instability at daytime and deeper stability at nighttime than is normally seen at Earth. The stronger daytime convection on Mars is associated with a deeper convective boundary layer than on Earth. On Mars a daytime boundary layer height of the order of the atmospheric scale height (see Table 1) is not unusual, while nighttime flows normally end up with large height intervals over which the Richardson number is large enough for turbulence to become intermittent. The small impact of the Martian atmosphere on the surface heat budget is augmented by another aspect of the atmosphere, its lack of significant amounts of water, which on Earth also acts to dampen the diurnal temperature cycle by evaporation and condensation.

[34] On Mars the vertical flux of longwave net radiation tends to play a larger role in the energy budget of the PBL than on Earth (see also sections 5 and 5.2). Indeed close to the ground, it will often dominate the turbulent heat flux [e.g., see *Savijärvi*, 1999; *Larsen et al.*, 2002; *Savijärvi and Kauhanen*, 2008]. The primary reason is that the Mars atmosphere is almost exclusively composed of CO_2, meaning that the specific concentration of greenhouse gases at Mars is ~100%, while on Earth it is around 1%–10% H_2O and 0.04% CO_2. Upwelling thermal infrared radiation from the insolated soil is prone to strong net absorption by the colder atmospheric CO_2 and, to a lesser extent, H_2O and dust. Model computations by *Haberle et al.* [1993a], *Savijärvi* [1999], and *Spiga et al.* [2010] (e.g., see Figure 3) indicate that, close to the ground (i.e., the lowest hundred meters or so in the midmorning, dependent on local time [see, e.g., *Savijärvi*, 1999, Figure 3]), the dominating net radiative forcing of the near-surface air temperature forces the turbulent heat flux to reverse sign relative to normal expectations: i.e., it becomes negative for unstable conditions and positive for stable conditions. Convective processes act to cool the atmosphere rather than warm it, as is the case on Earth. At larger altitudes (more than a few hundred meters above the surface) the turbulent heat flux tends to dominate. Absorption of shortwave and longwave radiation by the atmospheric dust loading also influences the heating and cooling of the air, similarly to clouds and dust on Earth.

[35] The low density of the Martian atmosphere also results in much higher kinematic viscosity, ν, and heat diffusivity, κ_T, than for Earth because the dynamic characteristics are divided by the density to derive the kinematic values entering our description of the atmospheric motion. The larger value of ν for the Martian atmospheric boundary layer in turn influences a number of parameters used to characterize the turbulent conditions of the atmosphere.

[36] The Kolmogorov scale, η, characterizing the smallest scale of turbulence due to the viscous dissipation of small-scale motions, becomes about 20 times larger than in the Earth's boundary layer. The existing data suggest that the length scales for turbulence production on Earth, typically represented by the measurement height and boundary layer height, can be used for Mars as well. Considering the typical measurement height for Martian wind data, $z = 1$ m, and a u_* value of 0.5 m s^{-1}, we find that η is about 0.3–1 mm on Earth but nearer to 7 mm–2 cm on Mars. Therefore, the characteristic Reynolds number for the flow becomes smaller on Mars, and the inertial subrange of the variance spectra for turbulence becomes shorter. Using typical values of atmospheric parameters, we find the ratio of shear production scale to η to be about 50 for Mars but 1250 for Earth. Therefore, we expect the inertial subrange of turbulence in the near surface atmosphere to be much less important on Mars than on Earth. Similarly, the Reynolds number based on roughness length (equation (7)) tends to be smaller on Mars than on Earth for similar wind speeds. As described in section 2, the roughness Reynolds number characterizes the interaction very close to the surface, e.g., determining the fluxes between the flow and the surface.

TABLE 1. Parameters Characterizing the Climate and Atmosphere for Mars and the Earth

Parameter	Mars	Earth	Units
Total solar irradiance	591	1373	W m^{-2}
Orbital eccentricity	0.093	0.017	
Axial inclination (obliquity)	25.2	23.4	degrees
Length of day	24.62 (1 sol)	23.94	hours
Length of year	686.98 (667 sols)	365.26	Earth days
Gravity, g	3.7	9.8	m s^{-2}
Atmospheric gas constant, R	188	287	J kg^{-1} K^{-1}
Typical surface pressure, p	7	1015	hPa
Typical surface density, ρ	1.5×10^{-2}	1.2	kg m^{-3}
Typical surface temperature, T	220	300	K
Scale height, $H = RT/g$	11	9	km
C_p	730	1010	J K^{-1} kg^{-1}
Kinematic viscosity, ν	10^{-3}	1.5×10^{-5}	m^2 s^{-1}
Buoyancy parameter, g/T	1.8×10^{-2}	3.3×10^{-2}	m K^{-1} s^{-2}
Dry adiabatic lapse rate, Γ	4.5×10^{-3}	9.8×10^{-3}	K m^{-1}

This means that the Martian surface flux is characterized as being in a somewhat smoother, more laminar regime than on Earth for similar wind speeds, and z_{0T} and similar scalar parameters will therefore be larger on Mars than on Earth.

[37] If one takes into account the above considerations, it seems that one can use the boundary layer formulations from Earth equally to describe the boundary layer on Mars, as has been confirmed by many studies. The overall empirical characteristics are that, close to the surface, we find typical wind speeds to be much as we know them on Earth. We find much stronger diurnal temperature variations, with more vigorous turbulent temperature and wind fluctuations during the day. These features have been found to be consistent with standard surface boundary layer similarity formulations with respect to the relation between mean profiles, fluxes and variances [*Sutton et al.*, 1978; *Tillman et al.*, 1994; *Larsen et al.*, 2002; *Gunnlaugsson et al.*, 2008; *Davy et al.*, 2010] (see section 4.4 for further discussion). Because of the higher turbulence activity in the daytime Martian boundary layer, one derives as well that the maximum daytime boundary layer height is higher on Mars than on Earth. See Table 2 for characteristic scales for the unstable boundary layers on Earth and Mars. For neutral to moderately stable conditions, one finds no substantial difference in the description of the Earth and Mars boundary layers. For (nighttime) stable conditions, it seems that the surface layer is driven into a more stable state more often than on Earth, in accord with the missing moderation by the turbulent heat flux, but since that state of the atmosphere is not well described, either on Mars or on Earth, we shall not dwell further on these conditions here.

[38] It is uncertain to what extent the importance of the net radiative flux for the temperature field can be reconciled with current surface layer scaling laws that assume the existence of a layer with the turbulent fluxes being independent of height close to the ground. Also, the equations for the growth of the unstable boundary layer height may be modified by the inclusion of radiative flux terms. The Martian atmospheric surface layer calculated from the results of models and data analysis cited above appears more consistent with all turbulence fluxes being height independent,

except for the heat flux, where it is the sum of the net turbulent and radiative heating rates that is constant with height.

[39] As somewhat of a side issue, the low density of the Martian atmosphere means that the exchange between the air and many atmospheric sensors are much weaker than on Earth, especially for those being moved by the air and those that utilize heat exchange with the air as their basic measuring principle. Since the exchange with the air for such sensors is weaker on Mars, other processes influencing the sensor output, like internal friction, radiation balance, and heat conduction losses, become relatively more important on Mars than on Earth [e.g., see *Taylor et al.*, 2008]. Additionally, on Mars the smallest diameter considered for some of the thermal sensors is about 25 μm, which is small enough for the sensor no longer to interact with the air under fully nonslip flow conditions (i.e., Kn is not sufficiently small, as defined in section 2). In that case, a partial slip condition must be applied when quantifying the interaction between the sensor and the flow in which it is embedded.

4. RECENT AND CURRENT MISSIONS AND OBSERVATIONS

[40] Our current knowledge relevant to an understanding of Mars' boundary layer is based on observations made by a large set of spacecraft (Table 3). The observations can be subdivided into orbital (section 4.3) and surface-based observations. The latter can in turn be further divided into in situ observations (section 4.1) and surface-based remotely sensed observations (section 4.2). These observations are of various types and they characterize not only the atmosphere itself, but also the planetary surface or variables providing indirect diagnostics of the boundary layer, its state and phenomenology. This section provides an outline and organized description of different types of relevant measurements and data sets (past to present), including specific missions and instruments as well as references to detailed descriptions of both.

[41] Descriptions of future missions and observations are given in sections 7.2 and 7.3. Missions in their implementation stages or confirmed for implementation (but not yet
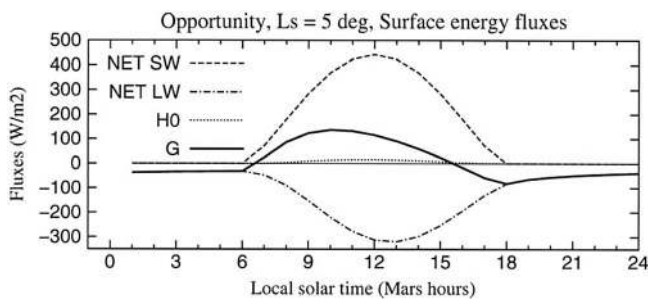
Figure 2. Surface energy fluxes in the 1-D simulation of *Savijärvi and Kauhanen* [2008] of conditions at the Opportunity landing site at $L_s = 5°$, showing the net shortwave flux (dashed line), net longwave flux (dash-dotted line), sensible heat flux H_0 (dotted line), and net heat flux into the ground G (solid line). Adapted from *Savijärvi and Kauhanen* [2008] with permission.
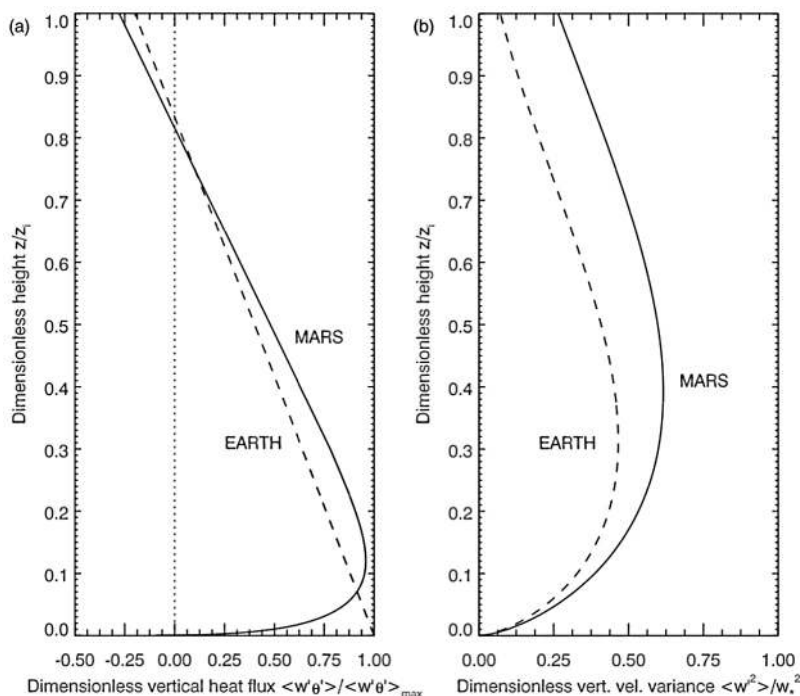
Figure 3. Similarity empirical functions in quasi-steady midday conditions, showing the average variation with dimensionless height (normalized by the boundary layer depth $z_i = h$) of dimensionless (a) vertical eddy heat flux and (b) vertical velocity variance on Mars (solid line) and on the Earth (dashed line). Adapted from *Spiga et al.* [2010] with permission.

in operation; see section 7.2), as well as a selection of some possible proposed observations (illustrative examples of what the next observational steps might and perhaps should be), have been included.

[42] Good starting points for accessing the data returned by past and current missions are NASA's Planetary Data System (http://pds.jpl.nasa.gov/) and the European Space Agency's (ESA) Planetary Science Archive (http://www.rssd.esa.int/index.php?project=PSA). Table 3 is an overview and compendium of PBL observations and relevant missions. Timelines of the instruments' periods of operations are shown in Figure 4.

4.1. Surface in Situ Observations

[43] Surface in situ observations have so far been point-wise observations (sampling the state of the atmosphere or surface as a function of time) as opposed to horizontal profiles along the surface (since none of the landed rovers have had this type of instrumentation; however, see section 7.2.1). Surface in situ observations have been performed by instruments on board four landers (Table 3): Viking Lander 1 and 2 (VL1, VL2), Mars Pathfinder (MPF), and Phoenix (PHX). The relevant instruments are listed in Table 3 and described in greater detail in sections 4.1.1 (VL1, VL2), 4.1.2 (MPF), and 4.1.3 (PHX). All these landers have provided pressure and temperature time series, whereas only the Viking landers have had satisfactory wind speed and direction sensors. Some atmospheric quantities have been measured simultaneously at two to three levels above the surface, allowing for estimation of vertical gradients for flux

estimations. The time series data sets exhibit varying temporal coverage (Figure 4), time resolutions, accuracies, and stabilities, described in sections 4.1.1–4.1.3. These landing sites have so far been only in the northern hemisphere, at latitudes from the subtropics to the polar region (Figure 5).

[44] Some surface in situ measurements have allowed for the detection and identification of the faster and more

TABLE 2. Approximate Mean Daytime SL and Convective Mixed Layer Turbulent Parameters on Mars and on Earth[a]

Parameter	Mars	Earth	Units
Unstable Surface Layer			
Obukhov length, L	−17	Similar	m
Friction velocity, u_*	0.4	0.3	m s^{-1}
Temperature scale, $|T_*|$	1	0.15–0.88	K
Dissipation rate, ϵ_z	0.16	0.01–0.02, $z = 4.32$ m	m^2 s^{-3}
		0.001–0.01, $z = 18$ m	m^2 s^{-3}
Temperature SD, $\sigma_\theta(z)$	3	0.18–0.32, $z = 4$ m	K
Horizontal velocity SD, $\sigma_u(z)$	2	1.4, $z = 4$ m	m s^{-1}
Vertical velocity SD, $\sigma_w(z)$	0.5	0.4–0.6, $z = 4$ m	m s^{-1}
		0.38–0.44, $z = 4.32$ m	m s^{-1}
Convective Mixed Layer			
Boundary layer height, h	6	0.2–2	km
Vertical velocity scale, w_*	4	1–2.5	m s^{-1}
Temperature scale, θ_*	0.1	0.03–0.1	K
Dissipation rate, $\langle \epsilon \rangle$	0.005	0.001–0.005	m^2 s^{-3}
Temperature SD, $\langle \sigma_\theta \rangle$	0.3	0.06–0.2	K
Horizontal velocity SD, $\langle \sigma_u \rangle$	2.4	0.47–1.13	m s^{-1}
Vertical velocity SD, $\langle \sigma_w \rangle$	2.4	0.6–1.4	m s^{-1}

[a]Terrestrial values correspond to planetary boundary layers formed over flat and homogeneous terrain and under conditions with no baroclinic disturbances. SD, standard deviation.
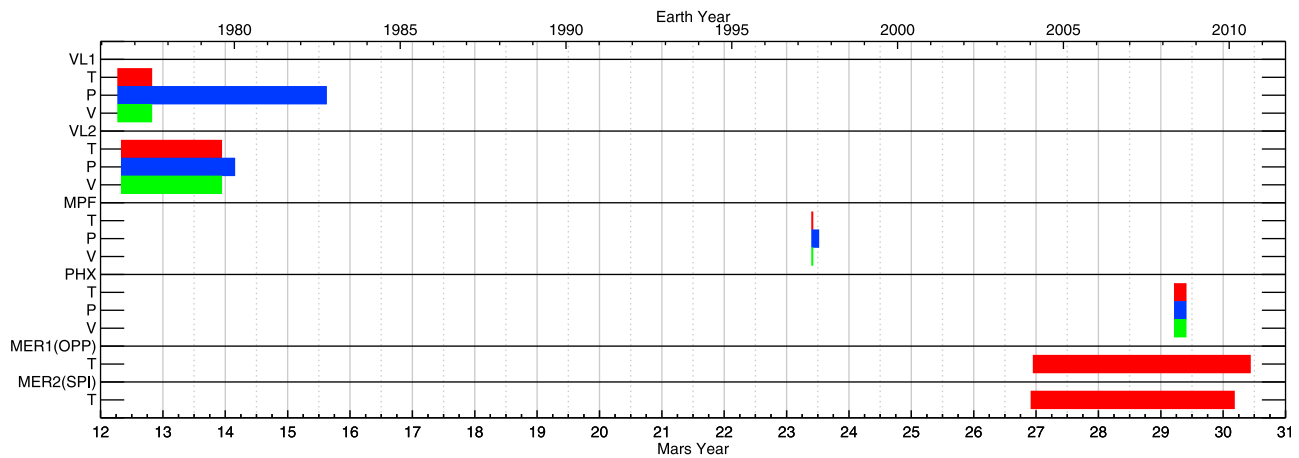
TABLE 3. Overview of the Past, Current, and Confirmed Future Missions and Their Observations Relevant to Studies of the Martian PBL[a]

Mission	Instrument	Landers			Orbiters				Surface									H_2O Content	PBL Direct					Dust		PBL Indirect			Subsurface H_2O
		In Situ	Imaging	Remote Sensing	Nadir	Limb	Radio Occultation	Solar and Stellar Occultations	α	I	Topography	T_s	z_0	T	p	$\vec{V}$	w		τ	h_{PBL}	$T(z)$	D_T/dz	dq/dz	Devils	Dust	Clouds	r_{eff}	h_{CL}	
																								Past and Current					
VO	IRTM			x	x				x	x		x																	
	MAWD			x	x													x											
	VIS		x	x	x																				x	x	x		
VL	VMIS	x												x	x	x					x[b]								
	Imager		x	x																				x	x	x	x		
Phobos 2	Auguste			x				x										x			x	x							
MGS	MOC			x	x														x		x	x	x	x	x	x			
	MOLA			x	x						x														x	x			
	RS			x			x													x	x								
	TES			x	x	x			x	x		x							x	x					x	x			
MPF	ASI/MET	x							x	x		x		x	x	x[c]					x[b]								
	IMP		x																					x					
MOd	THEMIS			x	x				x	x		x							x						x	x			
	GRS, HEND			x						x																			x
MER	Mini-TES			x	x				x			x						x[d]	x		x				x	x			
	PanCam		x																					x	x	x			
MEx	HRSC			x	x														x						x	x			
	OMEGA			x	x							x						x	x						x	x	x		
	PFS			x	x							x						x			x				x	x	x		
	RS			x			x					x								x	x								
	SPICAM			x	x			x											x		x				x	x			
PHX	SSI		x																x					x	x	x			
	RAC		x																					x	x	x			
	MET	x												x	x	x	x[e]												
	TECP	x										x						x											
	LIDAR			x	x														x		x	x		x	x	x			
MRO	HiRISE			x		x																				x			
	MCS			x	x	x						x						x	x		x	x	x		x	x	x	x	
																							Confirmed						
MSL	REMS	x		x								x		x	x	x	x	x	x					x	x	x			
	MastCam		x	x					x										x						x	x			

[a]Definitions and explanations of the symbols and acronyms can be found in Table A1.
[b]Entry profile.
[c]Only wind direction information is of satisfactory quality, magnitude information is not (see section 4.1.2).
[d]H_2O column abundance.
[e]Telltale observed via the imaging system (see section 4.1.3).

Figure 4. Periods of operations of lander missions and their instruments most relevant to PBL studies. See also Table 3. The vertical axis indicates missions and instruments. The bottom horizontal axis shows the time in Mars years, and the top horizontal axis shows the time in Earth years. For definition of the Mars years used here, see, e.g., *Clancy et al.* [2000, p. 9563]. The differences between the observational setups (e.g., temperature observations of the MERs versus the other landers as well as wind observations of MPF and PHX) are described in the text in greater detail.

short-lived PBL phenomena such as dust devils (see Figure 6). Dust devils have been previously observed by both orbital [*Thomas and Gierasch*, 1985] and lander imagers [*Metzger et al.*, 1999; *Ferri et al.*, 2003], but dust devil signatures have also been seen in the landers' pressure time series [*Ryan and Lucich*, 1983; *Murphy and Nelli*, 2002; *Ringrose et al.*, 2003; *Ellehoj et al.*, 2010] (see Figure 7). Sufficiently high sampling rates are required to characterize such signatures in pressure time series.

[45] The Mars Exploration Rovers' payloads include no in situ atmospheric sensors [*Squyres et al.*, 2003], but the Mini-TES instruments (see Table 3 and section 4.1) have been noteworthy [*Smith et al.*, 2004] for being able to make remote sensing measurements that can characterize the microscale region (from meters to kilometers) around the rovers (e.g., see Figure 8). The Mini-TES instruments are

described in greater detail in section 4.2.2. Unlike the earlier stationary landers (VL1 and VL2 (section 4.1.1) and the MPF (section 4.1.2)), the MERs have operated in the equatorial region, on opposite sides of the planet (Figure 5).

4.1.1. Viking Landers' Meteorological Instrumentation

[46] Both Viking landers carried the Viking Meteorology Instrument System (VMIS) as part of their payloads. The VMIS comprised wind speed and direction ($\vec{V}$), temperature (T), and pressure (p) sensors at a single level [*Chamberlain et al.*, 1976]. The wind speed was measured by an overheat hot-film sensor array, while direction was obtained with a quadrant sensor. Some early observational results are shown in Figure 9. *Hess et al.* [1977] suggested the wind patterns to be predominantly the result of pressure gradients due to a combination of local topographical slopes and coupling with large-scale winds aloft. At the VL1 site both factors were
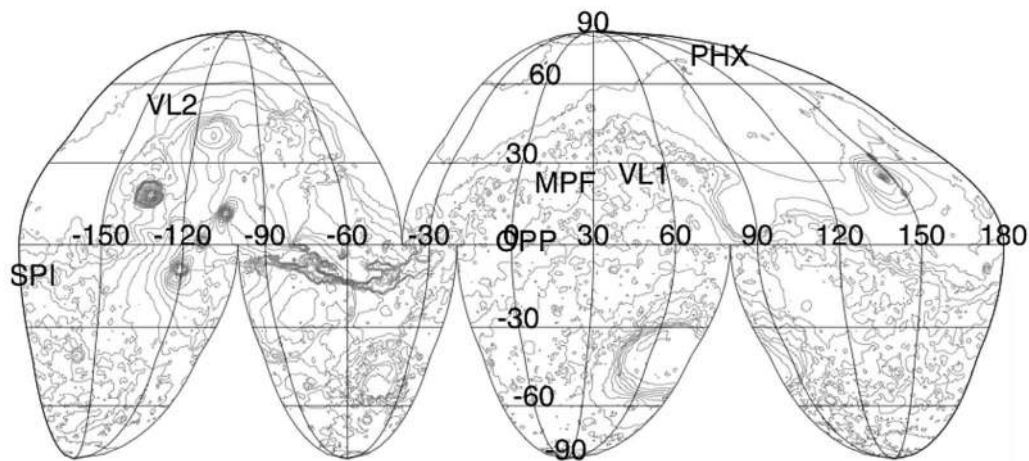
Figure 5. Landing sites of missions with relevant PBL observations shown in Goode's homolosine projection. Clear majority of the sites are in the northern hemisphere. MOLA topography contours are shown in grey to assist in locating the landing sites.

Figure 6. Image of dust devil vortices, laden with dust, passing the Spirit lander on sol 568. Image credit: NASA/JPL.

interpreted to be of similar magnitudes, while at the VL2 site the slope is seen to dominate.

[47] The T sensors were thermocouple arrays, and the pressure sensors were stretched diaphragm-type reluctance transducers. The $\vec{V}$ and T sensors were located approximately 1.6 m above the surface, and the p sensor was placed inside the lander body with the VMIS electronics.

[48] Instrument accuracies were reported as ±15% in wind speed (for speeds over 2 m s^{-1}), ±10% in wind direction,

±1.5 K in temperature, and 0.07 hPa in pressure. The pressure accuracy was limited by digitization. The VMIS temperature and wind measurements suffered from wind direction-dependent thermal contamination due to the heat plume emanating from the radioisotope thermal generators (RTGs [*Hess et al.*, 1977]) (see Figure 9). The initial observational strategy was to collect data with sample intervals of 4 s or 8 s in 11 min modules spaced 1 h 27 min apart [*Hess et al.*, 1976].

[49] Viking landers also measured entry profiles [*Seiff and Kirk*, 1977] although these obviously only represent a single instant (in local time and season) and a single location for each. Despite these limitations, these represented the first measurements of this kind for Mars and provided valuable information on the profile of the PBL with high vertical resolution.

[50] Temperature profiles observed during the entries are shown in Figure 10. A comprehensive analysis of these observations can be found in the study by *Seiff and Kirk* [1977]. They interpret the observations to show the occurrence of a near-surface convective region and deduce a PBL height of approximately 6 km at the time of landing.

[51] VL1 landed on 20 July 1976 (at areocentric longitude $L_s \approx 96.7°$) and operated until 13 November 1982
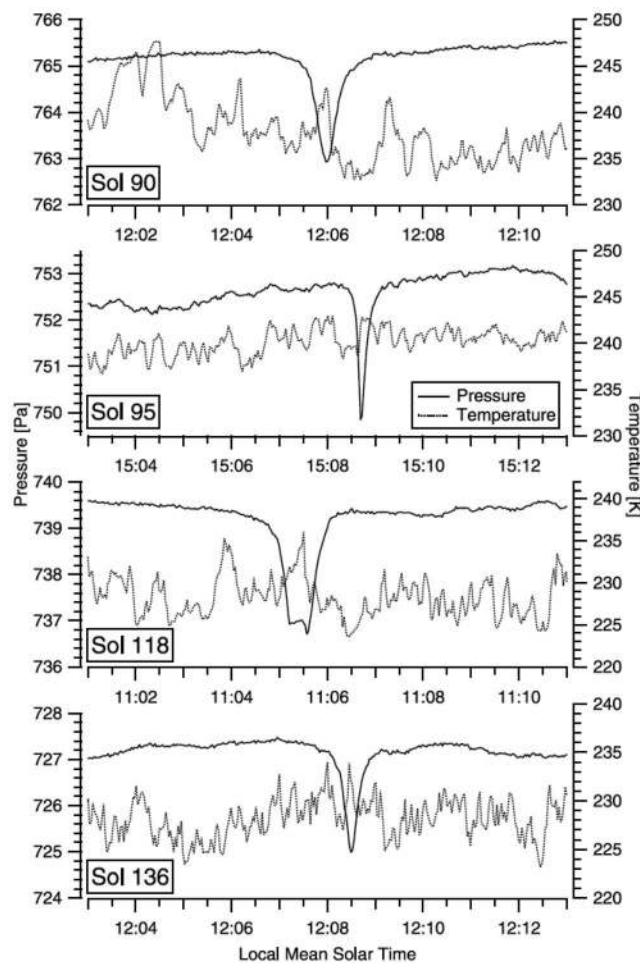
Figure 7. Raw pressure (solid lines) and temperature (dotted lines) measurements at the upper thermocouple on the Phoenix lander, showing examples of p and T variations during the passage of dust devil vortices over the spacecraft. Adapted from *Ellehoj et al.* [2010] with permission.
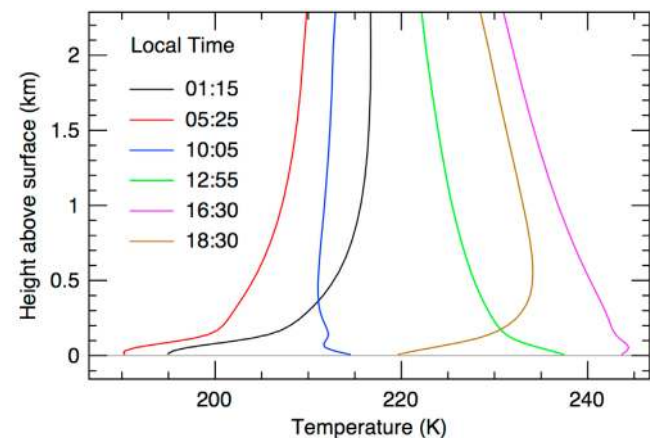
Figure 8. Typical temperature profiles retrieved from upward looking Mini-TES observations made over the course of 4 days by the Spirit lander near $L_s = 5°$, showing the evolution of the daytime near-surface superadiabatic layer and the nighttime inversion layer. Adapted from *Smith et al.* [2006] with permission.
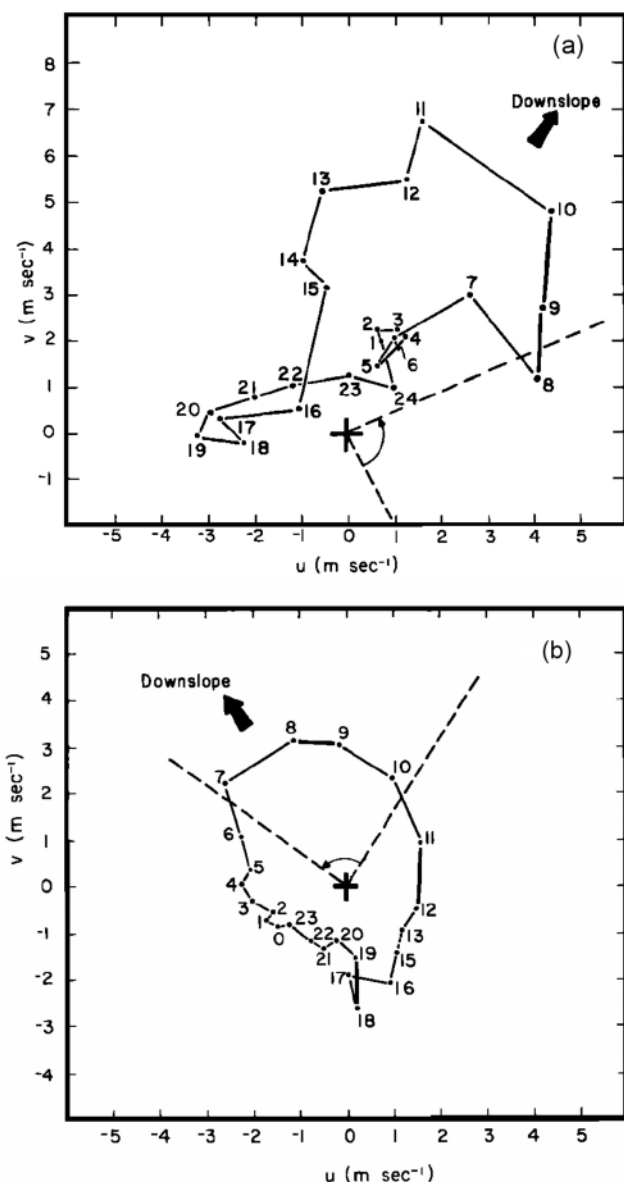
Figure 9. Mean wind hodographs (a) for the first 44 sols at the VL1 landing site and (b) for the first 50 sols at the VL2 landing site. Each point represents the vector mean of the northward and eastward components of the wind over the time interval indicated. The sectors indicated by dashed lines are directions suffering from interference from the body of the spacecraft. Adapted from *Hess et al.* [1977] with permission.

($L_s \approx 226.5°$; operating 2307 days or 2251 Martian solar days (sols), over 3 Mars years). VL2 landed on 3 September 1976 ($L_s \approx 117.2°$) and ended operations on 11 April 1980 ($L_s \approx 91.0°$; operating 1316 days or 1284 sols, almost 2 Mars years). See also Figure 4.

4.1.2. Mars Pathfinder Meteorological Instrumentation

[52] The MPF comprised the larger stationary lander and a small rover (the Sojourner). The payload included the Atmospheric Structure Instrument and Meteorology package (ASI/MET; located in the stationary lander) designed for measurement both during entry (especially the parachute-decelerated phase below ≈8 km) and after landing [*Seiff et al.*, 1997]. The ASI/MET comprised a wind speed and direction ($\vec{V}$) sensor, temperature (T) sensors at three vertical levels (see Figure 11), and a pressure (p) sensor. The sensor technologies were similar to those used in the VMIS: the wind sensor was an overheat sensor (albeit with smaller overheat) and located above the surface at $z = 1.1$ m, the T sensors (at $z = (0.25, 0.50, 1.00)$ m) were thin-wire thermocouples, and the p sensor (inside the lander) was similar to the VMIS design. Sample temperature observations are shown in Figure 11. The diurnal characteristics of the temperatures and the directions of the near-surface thermal gradients stem from the low density of the Martian atmosphere, which causes the atmospheric temperatures to be predominantly driven by those at the surface. For further details, see *Schofield et al.* [1997].

[53] The p sensor had two measurement ranges, 0–12 hPa for descent and 6–10 hPa for surface observations. The respective resolutions (at 14 bit) were 0.075 and 0.025 Pa. The T sensor design goals were an absolute accuracy of 1 K, relative accuracy of 0.1 K, and resolution of 0.04 K between 160 and 300 K of ambient temperature. The sampling intervals were 4 s for the synoptic observation sessions and 1 s for the boundary layer sessions [*Schofield et al.*, 1997].
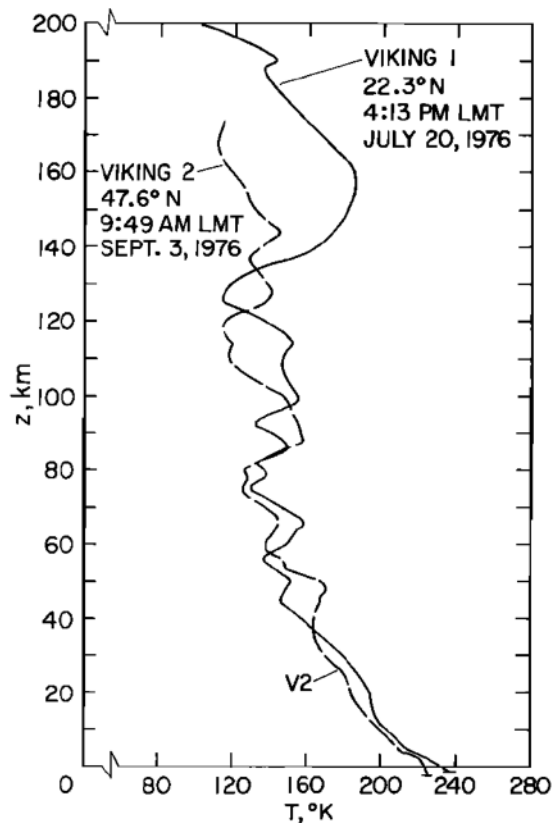
Figure 10. Temperature profiles measured during the entries, descents, and landings of the VL1 and VL2 spacecraft. Note that directly sensed temperature data are available for altitudes between 3.9 km and 1.45 km above the surface. Adapted from *Seiff and Kirk* [1977] with permission.
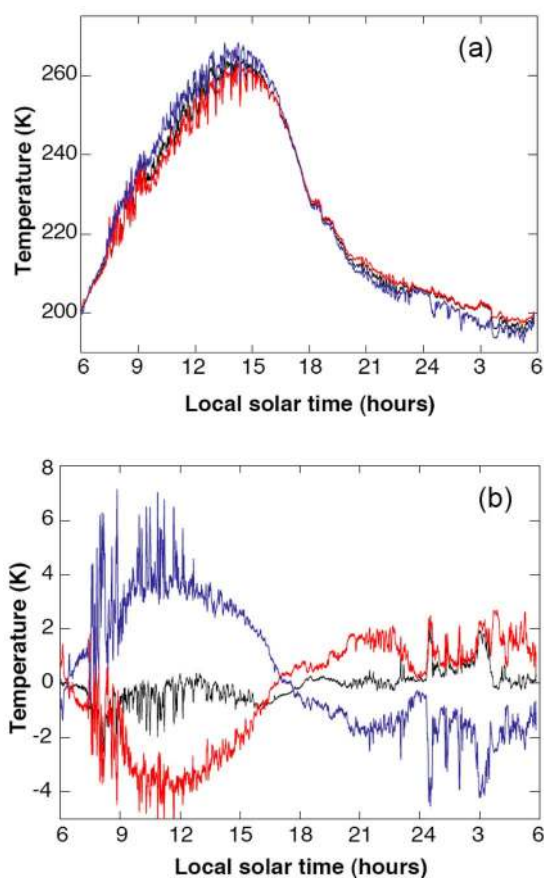
Figure 11. (a) The diurnal variation of atmospheric temperature measured by the top (red), middle (black), and bottom (blue) mast thermocouples at the MPF landing site, from 06:00 LST on sol 25 to 06:00 LST on sol 26. These thermocouples were 100, 50, and 25 cm, respectively, above the plane of the lander solar panels. Temperatures were sampled continuously at 4 s intervals throughout this period, but the plots use 30 point (2 min) running means for clarity (this smoothing reduces the amplitude and frequency of the fluctuations that are present in the raw data). (b) The data of Figure 11a plotted as temperature deviations from the mean of all three thermocouples. Sampling times and data smoothing are identical to those of Figure 11a. Adapted from *Schofield et al.* [1997] with permission of the American Association for the Advancement of Science.

Based on testing, the wind speed accuracy was approximately 1 m s^{-1} at low wind speeds, worsening to about 4 m s^{-1} above 20 m s^{-1}. Directional accuracy was of the order of $\pm 10°$. The MPF design attempted to address the problem of lander-induced thermal contamination (see also sections 4.1.1 and 4.1.3); the meteorological mast was placed, not over the spacecraft deck but at the end of one petal [*Seiff et al.*, 1997; *Schofield et al.*, 1997]. Despite this care, accurate determination of the magnitude of the wind vectors has ultimately been unsuccessful, although the wind directions have been extracted satisfactorily.

[54] MPF landed on 4 July 1997 ($L_s \approx 142.4°$) and operated until 27 September 1997 ($L_s \approx 188.0°$; 85 days or 83 sols; Figure 4). The typical variation of diurnal temperatures at three vertical levels, as measured by MPF, is illustrated in Figure 11.

4.1.3. Phoenix Meteorological Instrumentation

[55] Phoenix's payload included the Meteorological (MET) instrument package to "provide information on the daily and seasonal variations in Mars near-polar weather during Martian late spring and summer" [*Taylor et al.*, 2008, p.1]. The Phoenix MET package made direct atmospheric measurements only during the surface phase but not during the entry and descent. The Phoenix MET package consisted of temperature (T) sensors at three vertical levels and a compound pressure (p) sensor. The T sensors were thermocouples, as on previous landers and similar to MPF's ASI/MET at $z = (0.25, 0.50, 1.00)$ m, whereas the pressure sensing system (inside the lander) comprised a three-head silicon diaphragm sensor. Other sensors, not part of the MET package but relevant to observations of the Martian PBL, included the imaging system (section 4.2.1) and the LIDAR (section 4.2.3).

[56] The pressure system's accuracy at the beginning of the surface mission was <6 Pa when the temperature in the vicinity of the sensor was <0°C and <11 Pa when $T < 0$°C. Resolution was approximately 0.1 Pa and time resolution 2–3 s [*Taylor et al.*, 2010].

[57] Because of resource constraints, the MET package did not include a wind sensor similar to those in the VMIS or ASI/MET packages. Wind measurements were carried out with a simple telltale consisting of a lightweight suspended cylinder being deflected by the wind, with the deflection being estimated utilizing the Phoenix lander's imaging system (see Figure 12). The system has been found to supply reliable data on both mean wind and turbulence, although a simple description of resolution and accuracy is difficult to provide [*Gunnlaugsson et al.*, 2008; *Holstein-Rathlou et al.*, 2010].

[58] The temperature measurement quality requirements were as follows: range 140–280 K, absolute accuracy ±1 K,

Figure 12. Image of the telltale used to determine estimates of winds at the Phoenix landing site. Adapted from *Holstein-Rathlou et al.* [2010] with permission.

and resolution 0.5 K [*Taylor et al.*, 2008]. The MET experienced thermal contamination effects, however, similar to the VMIS and the MPF ASI/MET. The temperature measurements at the lowest level have been shown to be unreliable and highly dependent on wind direction because of the thermal contamination caused by the vicinity of the warm spacecraft deck (see also sections 4.1.1 and 4.1.2). This effect was investigated via a computational fluid dynamics simulation by *Davy et al.* [2010]. From the Martian PBL perspective, the Phoenix MET package observations have been used to estimate heat fluxes between the surface and the atmosphere [*Davy et al.*, 2010].

[59] Although not part of the MET, the Thermal and Electrical Conductivity Probe [*Zent et al.*, 2009] has also carried out observations (coordinated with the LIDAR and the MET telltale) pertinent to the atmospheric PBL, most importantly humidity and surface-atmosphere fluxes [*Zent et al.*, 2010]. PHX landed on 25 May 2008 ($L_s \approx 76.3°$) and operated until 2 November 2008 ($L_s \approx 151.1°$; 161 days or 157 sols, almost a quarter of a Martian year; Figure 4).

4.2. Surface-Based Remote Sensing

[60] The types of surface-based remote sensing instruments flown to date include imaging systems, LIDARs, and Thermal Emission Spectrometers (TESs). Their observations are described in greater detail below. Some other types (such as dedicated optical column thickness sensors) have also been planned and even implemented, but none have reached the Martian surface to date [e.g., *Harri et al.*, 1998].

4.2.1. Imaging Instruments

[61] All Mars landers have included imaging systems (Table 3), which can hence be regarded as surface-based remote sensing instruments with relevance for studies of atmospheric (and specifically, PBL) characteristics (such as dust optical thickness, water vapor content, aerosol properties) and meteorological phenomena (such as dust devils and condensation clouds; see Figure 6). Imaging systems typically can, however, provide only indicative and indirect information (such as occurrence of dust devils, presence of surface frost or of liquid brine droplets [*Renno et al.*, 2009]) on fundamental meteorological parameters and phenomena such as pressure, temperature, humidity, and convection. Imaging of dust devils [*Ferri et al.*, 2003] has, however, even provided some statistics on the dust devils' frequency of occurrence and characteristics. The Viking landers [*Pollack et al.*, 1977], Mars Pathfinder [*Smith et al.*, 1997], the two Mars Exploration Rovers [*Lemmon et al.*, 2004], and the Phoenix lander [*Moores et al.*, 2010] have successfully provided atmospheric imagery from the surface.

4.2.2. Mini-TES Instruments on the MERs

[62] Apart from imaging systems on board both the Viking landers and the Mars Pathfinder, Mars Exploration Rovers' Mini-TES [*Christensen et al.*, 2003] instruments are the first surface-based remote sensing instruments on Mars. Atmospheric observations are one of the instrument's three science objectives, the other two pertaining to mineralogy and thermophysical properties of surface materials. The key qualitative improvement of the Mini-TES' over previous atmospheric observations is that they have provided information on the vertical temperature profile from about 20 m up to approximately 2 km above the surface [*Smith et al.*, 2004]; see Figure 8 for some examples that clearly show the development of strongly superadiabatic thermal gradients near the ground during the day and a strong nighttime inversion layer at dusk. By comparison, the other landers' in situ temperature measurements have been carried out only in the lowest meter or two above the surface. In surface-looking mode, the Mini-TES instruments have also observed the brightness temperatures of the ground.

[63] The retrieval algorithms have been described and errors estimated by *Smith et al.* [2006]. The temperature errors are estimated to be ≈2 K at below ≈200 m, increasing to ≈5 K at 2 km. The error of aerosol optical depth determination is estimated to be the larger of 0.03 or 10% and that of the water vapor column abundance ≈5 pr μm.

[64] Mini-TESs can take a spectrum every 2 s. Each observation in turn is an average over 100–1000 spectra. The profiles are not in the true vertical, since the instrument's line-of-sight can be at maximum elevation angle of only 30° above the horizontal. Presenting the profiles as a single vertical profile is because of the assumption that the atmospheric parameters sensed vary relatively little in the region around the rover. Because of limited power resources of the rovers, the Mini-TES observations typically cover only a limited fraction of the diurnal cycle, typically from the morning to afternoon (approximately 10:00–17:00 LT); observations during other parts of the diurnal cycle are sparse [*Smith et al.*, 2004, 2006].

[65] The MER-A (Spirit) landed on 4 January 2004 ($L_s \approx 327.6°$) and MER-B (Opportunity) on 25 January 2004 ($L_s \approx 339.0°$). At the time of writing, MER-B continues to operate, but no communication from MER-A has been received since 22 March 2010. Both rovers' operational lifetimes have hence exceeded 3 Martian years (Figure 4).

4.2.3. Phoenix LIDAR

[66] The Phoenix lander's payload included the first atmospheric LIDAR deployed onto the Martian surface. The LIDAR has provided information on the vertical and temporal distributions of aerosols, both dust and ice crystals (and by proxy, on the PBL height), in the lowest 5–6 km. The instrument characteristics have been described by *Whiteway et al.* [2008]. Observations of water ice clouds at the top of the PBL, of precipitation from the clouds and of dust have been reported by *Whiteway et al.* [2009b, 2009a]. Some examples of such measurements are shown in Figures 13 and 14.

[67] Figure 13a shows profiles of optical extinction coefficient in the absence of water clouds, during which dust is the main source of attenuation. These profiles indicate a well-mixed boundary layer up to an altitude of around 4.5 km, with differences in the mean extinction reflecting slow seasonal changes in dust loading. Figure 13b shows a profile with H_2O ice clouds present in the form of two layers, one located at around 3.5–4.5 km altitude and another within 1 km of the ground. The identification of these layers as clouds is confirmed from the profiles in
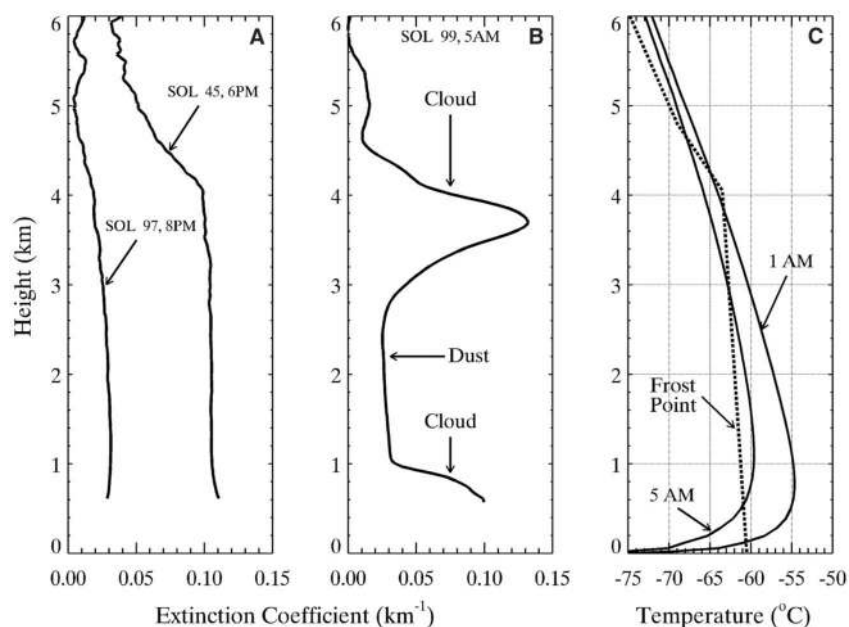
Figure 13. Profiles of the optical extinction coefficient at the Phoenix landing site, derived from the LIDAR backscatter signal at a wavelength of 532 nm (a) for sols 45 ($L_s = 97°$) and 97 ($L_s = 121°$) and (b) for 99 ($L_s = 122°$), obtained by *Whiteway et al.* [2009b]. Each profile is averaged over 1 h and smoothed for a vertical resolution of 40 m. (c) Height profiles of atmospheric temperature at the same site, estimated with a numerical simulation model of the Martian PBL [*Davy et al.*, 2010] and an estimate of the profile of frost point temperature. Adapted from *Whiteway et al.* [2009b] with permission.

Figure 13c obtained from the model of *Davy et al.* [2010], which shows temperatures dipping below the H_2O frost point at the approximate altitudes of the clouds. These clouds were sometimes observed to produce intermittent snow-like precipitation over the Phoenix site, as graphically illustrated in Figure 14.

4.3. Orbital Observations

[68] Orbital observations have a somewhat limited capacity to probe the lowest layers of the atmosphere, but they are equally irreplacable for certain global measurements and also crucial for PBL studies, such as the properties of the surface. In this section we list the different observational modes of past and current missions that may be useful for PBL studies.

4.3.1. Radio Occultation

[69] The RO method (as implemented in its uses so far) utilizes three main components: (1) radio transmitters (on one or multiple frequencies) on board a Mars orbiter, (2) ultrastable oscillator on board a Mars orbiter, and (3) ground stations on Earth. The ground stations receive the radio signal transmitted through Mars' atmosphere, either when the orbiter rises from behind the planet following an occultation or before it sets just prior to the occultation. For purposes of extracting information related to the atmosphere, the primary observable is the phase of the radio signal (and the variation thereof). The phase information allows for the atmospheric refractive index profile $\mu(r)$ (where r is the distance from planet's center) and subsequently number density, pressure, and temperature profiles ($n(r)$, $p(r)$, and $T(r)$, respectively) to be derived. A more

detailed description of this observational method can be found, e.g., in the study by *Tyler et al.* [1992].

[70] A variant of the method would involve two or more Mars orbiters equipped also with receivers and occultations between the spacecraft. This concept and its relevance to PBL studies is further elaborated in section 7.3.3.

[71] The RO method is generally considered the best orbital remote sensing method for PBL studies; RO observations can probe the atmosphere all the way down to the surface, and both the vertical resolution and overall accuracy
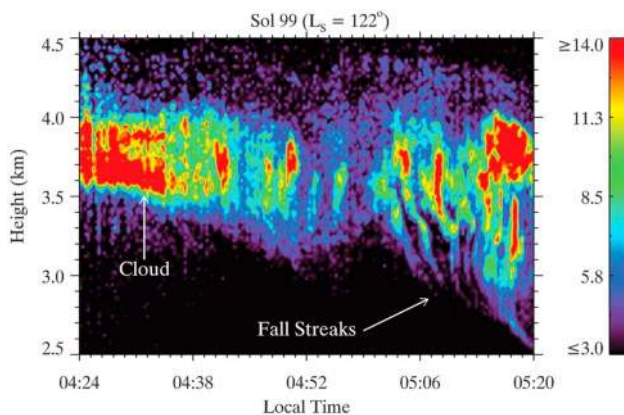

Figure 14. Contour plot of backscatter coefficient ($\times 10^6$ m^{-1} sr^{-1}) as a function of altitude and time, derived from the Phoenix LIDAR backscatter signal at a wavelength of 532 nm on mission sol 99 ($L_s = 122°$). Adapted from *Whiteway et al.* [2009b] with permission of the American Association for the Advancement of Science.

are very good in comparison with other remote sensing methods of the thermal profile. Weaknesses include the poor horizontal resolution (the method inherently averages the atmospheric state over a long tangential path in the atmosphere) and (in the orbiter-Earth implementation) the coverage may be restricted by the configuration of the orbiter's orbit and the Mars-Earth celestial mechanics.

[72] The description here is based on the radio science (RS) experiment on Mars Global Surveyor (MGS) [*Hinson et al.*, 1999, 2004; *Tyler et al.*, 1992], but the basic principles are applicable to any other RO experiment, such as those on board the Viking orbiters [*Michael et al.*, 1972], the Mars Express [*Hinson et al.*, 2008; *Spiga et al.*, 2010], or Mars Reconnaissance Orbiter (MRO) [*Zurek and Smrekar*, 2007]. The MGS RS experiment atmospheric observations have been reported, e.g., by *Hinson et al.* [1999, 2001, 2003] and *Hinson and Wilson* [2002, 2004].

[73] The RO measurements and derived quantities relevant for PBL studies include vertical profiles of temperature, static stability, geopotential height, and the balanced wind field [*Hinson et al.*, 2004]. However, the near-surface (PBL) wind field cannot be directly inferred from the temperature field derived from RO measurements, as this wind field is not balanced because of the effects of surface friction. Temperature measurements give access to other quantities such as the PBL height when defined via the temperature vertical structure. The retrieved profiles begin either from the surface or some hundreds of meters above the surface and reach altitudes of tens of km, thus covering easily the extent of even the daytime PBL. Vertical resolution is ≈500 m–1 km, whereas horizontal resolution is highly anisotropic: along the line-of-sight the horizontal resolution is of the order of few hundred kilometers, in the direction perpendicular to the line-of-sight horizontal resolution is comparable to the vertical resolution [*Hinson et al.*, 1999, 2001, 2004; *Hinson and Wilson*, 2004]. The accuracy of the measurements increases with increasing pressure (accuracy is better closer to the surface) and is of the order of 0.3%–0.4% in the lowest layers, corresponding to 1 K and 2 Pa. In the highest layers of the profiles, the corresponding numbers are 6%, 10 K, and 0.6 Pa.

[74] *Hinson et al.* [1999] published the first results on the MGS radio occultation measurements, and they addressed some results on the observed structure of the radiative-convective boundary layer. These were also the first remote sensing measurements that could resolve the vertical and temporal variations of the PBL. The observations in the study by *Hinson et al.* [1999] were limited to the period from evening through nighttime until just before dawn. The stratification below 3 km was slightly subadiabatic in the evening and showed a strong inversion in the predawn hours. They also estimated the daytime convection to reach an altitude of 8–10 km (at around 18:00 LT) in these early summer profiles from southern subtropical and midlatitudes. An example is shown in Figure 15, showing evidence for the development of a radiatively induced temperature inversion in the lowest part of the atmosphere during the night.

[75] Thus, RO profiles with better than 1 km vertical resolution in the lower atmosphere were available during the 10 year long MGS mission, but the latitude and time coverage were not suitable for PBL convection studies [*Hinson et al.*, 1999]. This limitation was recently addressed with the Mars Express (MEx) RO profiles [*Hinson et al.*, 2008]. The MEx RO observations have provided good coverage at latitudes and local times where PBL convection is occurring (low-latitude terrains and around 16:00–17:00 LT). Properties such as the potential temperature down to 1 km above the surface, as well as the PBL depth, can be determined accurately by the RO limb sounder. The vertical resolution is <1 km and the horizontal resolution in the direction perpendicular to the line-of-sight is comparable (and much smaller than typical PBL depths on Mars), whereas the horizontal resolution along the line of sight is of the order of 400 km. Such measurements enabled *Hinson et al.* [2008] to identify striking variations in the depth of the convective PBL within the low-latitude Martian regions. The Martian convective boundary layer appears to extend to higher altitudes over high plateaux (e.g., 8–9 km over Tharsis) than in lower-altitude plains (e.g., 5–6 km over Amazonis) despite similar surface temperatures. Such behavior is related to convection arising from solar heating of the ground, and the impact of this heat source on thermal structure being largest where the surface pressure is smallest, at high surface elevations [*Hinson et al.*, 2008]. Modeling studies [*Spiga et al.*, 2010] indicate that this clear correlation of PBL depth with spatial variations in surface elevation and weaker dependence on spatial variations in surface temperature is a consequence of the prominent radiative forcing of the Martian boundary layer (see section 5.3).

[76] The theory proposed by *Souza et al.* [2000] sheds light on the basic thermodynamical mechanism by which topographical features enhance convective circulations and the depth of the PBL over elevated terrain. It follows from the second law of thermodynamics that the surface heat flux is proportional to the temperature difference between the ground and the near-surface air. Thus, when the ground is flat and uniform, the surface heat flux decreases as an air parcel moves toward the updraft. However, on sloping terrains, horizontal potential temperature gradients cause the surface heat flux to decrease less rapidly when an air parcel moves upslope. This forces stronger convection and produces a deeper PBL over the elevated terrain.

4.3.2. Solar and Stellar Occultations

[77] Solar and stellar occultations use a similar observation geometry to the radio occultations, with the exception that the Sun or stars function as the sources of the radiation and the satellite instrument as the receiver. The difference between the reach of stellar and Solar occultations is demonstrated by, for example, MEx Spectroscopie Pour l'Investigation des Caractéristiques de l'Atmosphère de Mars (SPICAM), which can use both as occultation sources. Stellar occultations so far made in the UV and near-infrared wavelengths are not suitable for PBL studies, as the weakness of the stars as light sources and dustiness of the Martian
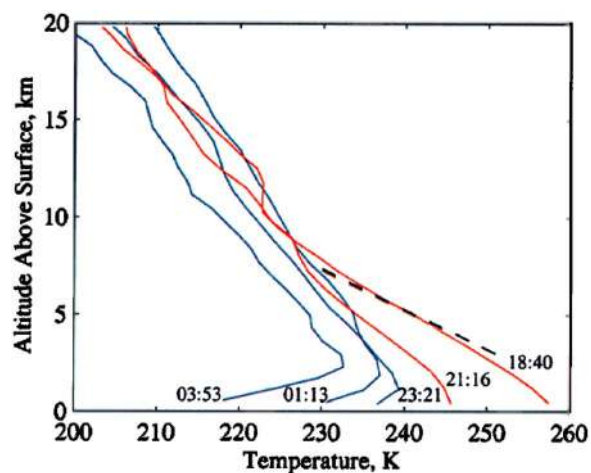
Figure 15. Temperature profiles from the southern hemisphere of Mars, obtained by *Hinson et al.* [1999] from MGS radio occultation measurements. Only the lower portion is shown to emphasize structure near the surface. Red and blue lines denote measurements made before and after sunset, respectively. The profiles show the nighttime development of a temperature inversion within ~3 km of the surface. Profiles were acquired over several months covering the seasonal interval $235° \leq L_s \leq 342°$. The dashed line shows the adiabatic temperature gradient. Adapted from *Hinson et al.* [1999] with permission.

atmosphere implies practically no atmospheric transmission at altitudes below 30–40 km. In principle, solar occultations are able to probe the atmosphere all the way down to ≈10 km as demonstrated by SPICAM infrared (IR) spectrometer [*Fedorova et al.*, 2009] with a vertical resolution of 3–5 km [*Fedorova et al.*, 2009; *Chassefière et al.*, 1992]. Solar occultation observations have, however, limited coverage in local time, since observational opportunities are restricted to the evening or morning terminators (sunset or sunrise).

[78] Examples of solar occultation experiments are the Phobos 2 Auguste [*Korablev*, 2002] and MEx SPICAM [*Bertaux et al.*, 2006; *Fedorova et al.*, 2009]. Aerosol and water vapor profile results from the Auguste experiment have been reported by *Chassefière et al.* [1992, 1995] and *Rodin et al.* [1997]. *Chassefière et al.* [1992, 1995] observed the aerosol mixing ratio and effective radius r_{eff} only in the range between 15 and 25 km, from where they extrapolated the results all the way to the surface using certain assumptions of the vertical distribution. *Rodin et al.* [1997] reported values for the condensation level of water vapor ($h_{CL} \approx$ 25 km), eddy diffusion coefficient, and its vertical variations, and measured the constant mixing ratio of water vapor in the lowest atmosphere (10–15 km) to be 150 ± 50 ppmv. They also observed clouds at 3–8 km altitude (perhaps at the top of the PBL) and retrieved particle sizes of $r_{eff} \approx 2~\mu$m for these clouds.

[79] Ongoing investigations with the SPICAM solar occultations are revealing water vapor, aerosol [*Fedorova et al.*, 2009], and ozone [*Listowski et al.*, 2011] profiles down to at least 10 km altitude with unprecedented accu-

racy. These studies may provide new insight into, for example, the vertical distribution of water vapor and the hygropause altitude and its variations. The water vapor vertical distribution is important for PBL studies and for disentangling the possible influence of the regolith in the near-surface water cycle.

4.3.3. Nadir

[80] Nadir observations are the most utilized of all the remote sensing modes, and they do provide important surface and atmospheric data for PBL studies despite the observing geometry often providing coarse or no information on the vertical variations of the observed, nonsurface quantities. In nadir observation mode the instrument's line-of-sight is directed toward the surface, often perpendicular to it. So-called spot-pointing observations (a.k.a. emission phase function), where the instrument looks at a fixed point on the planet's surface and the emergence angle changes while the satellite moves on its orbit over this point, present another less frequent option for nadir observations. Nadir observations can be passive or active: radiation emitted from, scattered from, or absorbed in the atmosphere and at the surface is observed with the sensor (e.g., spectrometer or camera) or the reflection of an emission sent from the instrument itself is received at the receiver (LIDAR, radar). Nadir observations, for the purposes of this discussion, can be divided into observations of the surface and of the atmosphere (and phenomena within).

[81] Many surface parameters important to the atmosphere can be readily retrieved from nadir observations of the surface (with examples from Mariner 9, the Viking orbiters, MGS, MEx, and Mars Odyssey 2001 (MOd)). These include the surface temperature T_s, which itself depends on the thermal inertia (I) and on the albedo (α) of the surface material [*Kieffer et al.*, 1976, 1977; *Mellon et al.*, 2000; *Christensen et al.*, 2001; *Fergason et al.*, 2006]. T_s controls the flux of heat from surface to the PBL. Equally important for modeling the near-surface atmosphere is the local topography, which can nowadays be mapped with very high resolution using LIDAR [*Smith et al.*, 2001]. In addition to the large-scale topography, the surface roughness (z_0) is an important parameter for the development of the vertical profile of the wind in the PBL. Images can be used to map rock abundances at, e.g., possible landing sites. This information can be later used to derive z_0 [*Heavens et al.*, 2008; *Hébrard et al.*, 2008]. The thermal inertia mentioned above describes a property of the top few centimeters of the soil, but the propagation of the thermal wave into the ground depends on the changes with depth of the soil properties. For example, subsurface ice and its distribution can have a strong impact on the temperature variations in the ground. The MOd Gamma Ray Spectrometer and MOd High-Energy Neutron Detector neutron data indicate large subsurface hydrogen content, which has been interpreted as subsurface ice [*Mitrofanov et al.*, 2003; *Boynton et al.*, 2004; *Jakosky et al.*, 2005; *Kuzmin et al.*, 2007]. The distribution of this subsurface ice globally and vertically (on time scales of 100–1000 years) depends on, for example, latitude, the properties of the soil, the local concentration of atmospheric vapor, and

the thermal conditions in the soil. Feedback in this system exists since the concentration of the water vapor in the atmosphere and the thermal conditions in the soil also depend on the distribution of the subsurface ice. Thus it is clear that information on the global distribution of the sub-surface water ice may turn out to be important also in its influence on the PBL because of differing surface and sub-surface temperature responses, which in turn may affect, for example, the seasonal adsorption and desorption of water from the regolith and thus the water cycle both globally and in the PBL. The polar caps and their growth, extent, and retreat have been surveyed with several instruments, and their extent, seasonal changes, and composition are presently very well known [*James and Cantor*, 2001; *Kieffer and Titus*, 2001; *Langevin et al.*, 2005; *Douté et al.*, 2007]. Such information is important for studies of the polar and midlatitude boundary layer since the polar caps may extend to the midlatitudes in both hemispheres.

[82] Imaging instruments can be used to observe clouds, dust devils, and storms [e.g., *Cantor et al.*, 2001, 2002; *Drake et al.*, 2006], and other visible phenomena in the PBL that are the outcomes of atmospheric circulations, which are in turn often affected by the surface properties. These phenomena can reveal information on favored lifting zones, wind speeds, properties of the surface, and the region's applicability as a landing site. In addition they naturally reveal the state of the atmosphere and the PBL, which needs to be favorable for the formation of such circulations.

[83] Other atmospheric (mesoscale) circulation phenomena that have an influence on or an expression in the PBL have been observed indirectly. The Viking orbiters observed so called "bore waves" in the vicinity of the Tharsis ridge [*Hunt et al.*, 1981]. *Hunt et al.* [1981] explained these wave features to be created by slope winds and their interactions in the mountain highlands, thus giving indirect evidence of slope winds in the area. Near-surface clouds and fogs can also be observed with nadir observations: *Inada et al.* [2008], for example, observed a dust haze in Valles Marineris, which has most probably a very interesting local climate with changing local solar incidence angle (depending on the time of day and the season and including the effects of shadowing from large nearby topographic changes) as well as slope and valley winds on the steep slopes and at the bottom of the long canyon. *Inada et al.* [2008] only speculated on the possible forming mechanisms of the haze and left detailed atmospheric studies for future work. However, slope winds in the topographically complex canyon may play a role in the formation of such haze. These examples show how nadir observations of, for example, cloud features as well as surface and near-surface temperatures can give indirect clues of local atmospheric mesoscale, and even PBL, phenomena in play.

[84] A spectacular example of an unexpected indirect observation of condensation and dust clouds is the observations from orbit by LIDAR, as was done with MGS Mars Orbiter Laser Altimeter (MOLA) (see Figure 16) that revealed and mapped near-surface CO_2 clouds in the polar night for the first time [*Pettengill and Ford*, 2000; *Ivanov and Muhleman*, 2001].

[85] Dust optical properties (like the single scattering albedo) and dust optical depth are crucial properties in their influence on the whole atmosphere, including the PBL, because of the profound impact of dust on the atmospheric radiative transfer and thus, on the vertical temperature profile both within and above the PBL. These properties have been mapped globally and locally with a wide set of instruments on several missions, such as MGS TES [*Clancy et al.*, 2003; *Wolff et al.*, 2006], MEx Observatoire pour la Minéralogie, l'Eau, les Glaces et l'Activité (OMEGA) [*Vincendon et al.*, 2007; *Määttänen et al.*, 2009], and MRO Compact Reconnaissance Imaging Spectrometer for Mars and Mars Color Imager [*Wolff et al.*, 2009, 2010].

[86] For retrieving the dust column optical depth, some a priori assumptions of the dust vertical profile need to be made. The most commonly used assumptions are a well-mixed (constant mixing ratio) profile and the so-called Conrath profile [*Conrath*, 1975]. However, some studies have shown that dust on Mars may well be concentrated in the lowest 1–2 scale heights of the atmosphere, at least in dust storm conditions [e.g., *Määttänen et al.*, 2009]. Characterization of dust vertical profiles is not easy with nadir observations (except perhaps with LIDAR), but at least in dust storm conditions comparisons between observed and modeled temperature profiles can provide important constraints on the dust profiles [*Määttänen et al.*, 2009].

[87] In addition to the dust column, the water vapor column is another important atmospheric variable measured with nadir observations. Considering the PBL, the vertical variations of the water column, and possible near-surface reservoirs affecting it, are important, as mentioned already with occultation observations. Nadir observations of the water column may give hints of the role of regolith in the water cycle and thus the near-surface variations of water vapor abundance, as pointed out by, for example, *Jakosky and Farmer* [1982] and *Fouchet et al.* [2007].

[88] Nadir observations of absorption spectra in the infrared can also be used to retrieve the thermal profile within and above the PBL using the 667 cm^{-1} CO_2 absorption band and its wings [*Formisano et al.*, 2001; *Grassi et al.*, 2006; *Conrath et al.*, 2000; *Smith et al.*, 2001a, 2001b]. Because of the nadir geometry, however, the ability to sense the thermal profile in the PBL itself is the most difficult, although the temperature in the middle atmosphere is influenced by the PBL behavior. This issue can be overcome, though, if the infrared spectrometer is also able to make measurements in a limb-viewing geometry (see section 4.3.4).

[89] Another example of atmospheric phenomena that can be observed with nadir observations is the surface pressure p_s. OMEGA on Mars Express has been used to retrieve p_s [*Forget et al.*, 2007; *Spiga et al.*, 2007], which has revealed small-scale local atmospheric phenomena (such as waves and pressure changes around craters) possibly related to PBL processes.
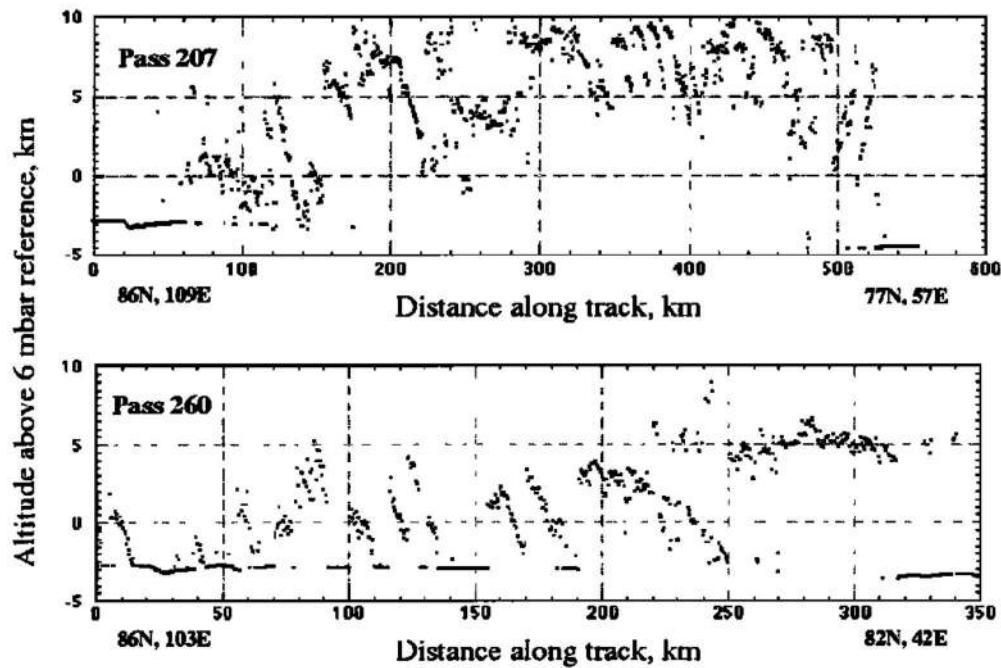
Figure 16. Examples of periodic cloud echo profiles from orbital passes 207 (L_S - 301.3°) and 260 (L_S - 316.4°) of the MGS MOLA LIDAR. The discontinuous solid line seen below the clouds corresponds to echoes from the surface, which are often preempted by echoes from the clouds above. Adapted from *Pettengill and Ford* [2000] with permission.

4.3.4. Limb Sounding

[90] Observations of the Martian limb can provide atmospheric profiles of parameters such as temperature, aerosol opacity, particle sizes, water vapor, and other trace gases. However, the instrument pointing and satellite position need to be very accurately known for correct line-of-sight altitude determination, and furthermore the vertical resolution is not necessarily much better than one scale height [*Rannou et al.*, 2006]. Thus limb observations can be very useful for observing aerosol properties and the large-scale atmospheric state, since also the gradient wind field can be retrieved from the temperature field. But the resolution of the limb observations is not sufficient to reveal details of the PBL structure even though the observations reach the lowest scale height and the surface. Examples of limb observations by TES and SPICAM are provided, for example, by *Smith et al.* [2001a] and *Rannou et al.* [2006].

[91] A recent investigation, the Mars Climate Sounder (MCS [*McCleese et al.*, 2007]) on the Mars Reconnaissance Orbiter, uses the limb observing technique to efficiently scan the whole atmosphere with a vertical resolution of about 5 km and horizontal resolution of 200 km [*Kleinböhl et al.*, 2009]. This scale of vertical resolution may render the MCS observations useful for coarse-scale PBL investigations. Observed fields include temperature profiles, aerosol opacity (including dust and ices), and its vertical distribution. Nadir observations to complement the limb profiling are also scheduled. The instrument was designed to acquire water vapor profiles as well, but unforeseen changes in channel response after the assembly phase have hindered this aspect of the retrievals to date.

4.3.5. Mutual in Situ and Remote Observations

[92] The Mini-TES instruments included in the Mars Exploration Rover payloads can probe the lowest layers of the atmosphere up to 2 km altitude with a reasonably high vertical resolution [*Smith et al.*, 2004] (see also section 4.2.2). Mutual observations with orbiting near-infrared instruments (such as MGS TES, MOd Thermal Emission Imaging System, and MEx Planetary Fourier Spectrometer (PFS)) have been made to resolve the full atmospheric profiles and to provide ground truth for validation of the remote sensing observations. These studies have proven to be very fruitful and have, for example, revealed the capacity of the PFS to probe the atmospheric temperatures down to 5 km altitude or less with generally good agreement with Mini-TES [*Wolkenberg et al.*, 2009]. *Wolkenberg et al.* [2009] noted also that the local time had the largest influence on the agreement between the measurements from orbit and from ground: even if the observations were made some sols apart, but at the same local time, the agreement between the profiles was usually good. However, if the measurements were from different local times, but from the same sol, the difference was significantly larger. This is an indication of the large diurnal variability and of the repetitive nature of developing convection in the PBL at the two MER sites. Surface temperature and column opacity measurements can be compared in a similar manner.

4.4. Use of Mars Lander Data to Validate Surface Layer Scaling Laws

[93] Data from the Viking, Pathfinder, and Phoenix missions have been used to validate the Monin-Obukhov and other boundary layer turbulence scaling laws (see *Tillman*

et al. [1994]; *Larsen et al.* [2002] using Viking and Pathfinder data, and *Gunnlaugsson et al.* [2008]; *Davy et al.* [2010] for Phoenix data). On Earth, such validations normally involve making simultaneous measurements of wind, temperature, and humidity profiles, combined within dependent flux measurements. The Mars validations have been somewhat more primitive, however, because of the lack of such a complete data set. At the Viking lander sites, wind and temperature measurements were available at one level, while both the Pathfinder and the Phoenix landers were equipped still for measuring at one velocity level only but with sensors at three temperature levels. Hence, a thorough evaluation of the Monin-Obukhov similarity theory on Mars has not so far been possible.

[94] Instead, a consistency check has been performed between the available data and the similarity scaling formulations developed for the Earth's atmosphere. For all landers, u_* has been estimated from the mean wind velocity, and an estimate of the roughness length scale, z_0, has been obtained from the surface characteristics of the terrain surrounding the landers [*Larsen et al.*, 2002]. The heat flux has been estimated from the temperature profile. For Viking data especially, the surface temperature was also estimated from a radiation balance model, and the near-surface atmospheric temperature was estimated from either a sublayer diffusion model or an estimate of z_{0T}. From Pathfinder and Phoenix, one could use the measured temperature gradient directly, since all three temperature levels were within the turbulent surface layer. Hence one can effectively estimate the surface heat flux and friction velocity consistent with both the measured wind speed and temperatures (given the assumption of Monin-Obukhov profiles). These parameters have subsequently been inserted in standard models for wind and temperature variances and/or spectra for comparison with the variance of the wind and temperature fluctuations measured by the landers.

[95] To compare the measured and modeled spectra and variances, the many special measurement aspects of Martian fluctuation measurements relative to normal Earth-based procedures and instrumentation have had to be considered, such as the effects of substantial flow distortions around the landers, sampling problems associated with aliasing (Viking), larger Martian Kolmogorov scales than on Earth (Viking; see section 2), and unusually low measuring heights compared to Earth data. Such issues are compounded by the use of, at best, fairly slowly responding sensors and relatively low data rates (all data sets). In view of these aspects of the data, most of the studies so far have concentrated on comparing modeled and measured power spectra, while just one [*Holstein-Rathlou et al.*, 2010] has presented a comparison of measured variances compared to variances predicted from spectral models.

[96] Finally, it should be mentioned that the parameterization of the low-frequency behavior of the velocity fluctuations for unstable conditions requires an estimate of the height of the unstable boundary layer. In practice, this was estimated from the history of the surface heat flux, in a standard way. Examples of spectral presentations are shown in Figures 17

and 18, illustrating our ability to model especially the wind spectra on Mars (see Figure 17), using adaptations of the scaling and formulations derived from the Earth's surface layer. Temperature spectra (see Figure 18) are less well understood but still show evidence for an onset of the inertial subrange consistent with the expected scaling behavior.

[97] Although the results of the above procedures have provided some validation of the application of the classical Monin-Obukhov scaling laws in the Martian atmospheric boundary layer, they do not really test the flux-profile relations that constitute the core of the Monin-Obukhov similarity approach. They cannot therefore be used in a straightforward way to evaluate the hypothetical balance between the turbulent near-surface heat flux and the effects of net radiation in generating the mean temperature profile close to the ground, as has been suggested by some modeling results [e.g., *Savijärvi*, 1999; *Spiga et al.*, 2010]. In a way, all applications of these surface layer scaling laws to the interpretation of measured data or to model parameterizations can be regarded as consistency checks of the above type, so long as no inconsistency appears in the results (see the discussion in section 5.2). But to date, the most direct validation has been performed on the aforementioned spacecraft data.

5. MODELING THE MARTIAN PLANETARY BOUNDARY LAYER

[98] The many observational efforts about Mars' atmosphere and ground have been supported and interpreted by a wide range of theoretical and numerical modeling studies, many of which have been based on a hierarchy of atmospheric models. General circulation models (GCM) produce views of the large-scale synoptic weather and climate [e.g., *Leovy and Mintz*, 1969; *Pollack et al.*, 1976, 1981; *Haberle et al.*, 1993a; *Forget et al.*, 1999; *Wilson*, 1997; *Allison et al.*, 1999; *Takahashi et al.*, 2003; *Moudden and McConnell*, 2005; *Segschneider et al.*, 2005; *Takahashi et al.*, 2006], while mesoscale models are increasingly being used to study the fine structure of local weather phenomena and to support various mission objectives, including the selection of safe landing sites and weather forecasts for intended landings [e.g., *Rafkin et al.*, 2001; *Toigo and Richardson*, 2002; *Tyler et al.*, 2002; *Moudden and McConnell*, 2005; *Wing and Austin*, 2006; *Kauhanen et al.*, 2008; *Spiga and Forget*, 2009]. As in the case of the atmospheric and oceanic boundary layers on Earth, models of the PBL on Mars include similarity theories, Reynolds stress models (hereafter ReSMs), and LESs. All these approaches are intertwined and interconnected, and the degree of their overall consistency can be used as one of the tools of each respective models' validation. Among the similarity theories, Monin-Obukhov theory takes the central stage and has already been briefly reviewed in sections 2, 3, and 4. The turbulence in the Martian PBL is commonly studied nowadays using large-eddy and direct numerical simulations (LES, DNS; see section 5.3 below), while the local structure of the lower Martian atmosphere has been charted by the help of one- and two-dimensional PBL models [e.g., *Gierasch*
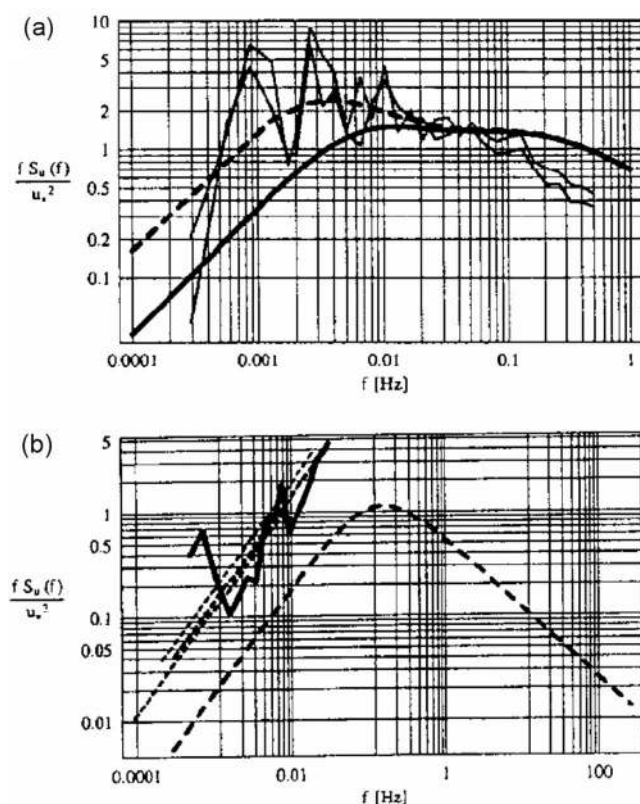
Figure 17. Spectra of wind speed normalized by u_* and compared with the models. (a) An unstable spectrum from the Pathfinder lander [*Larsen et al.*, 2002]. The low-frequency peak, reflecting the frequency associated with boundary layer height eddies, is clearly seen. At higher frequencies, the effects of the low-pass filter characteristics of the sensors affect the shape of the spectrum. (b) A stable velocity spectrum from the Viking landers [*Tillman et al.*, 1994]. The measured spectrum here is strongly influenced by the relatively low sampling rate and effects of aliasing. The bell shape indicates the modeled spectrum (see text), the thick line indicates the measured spectrum, and the lines through the data indicate the modeled data spectrum, taking into account the aliasing and the Kolmogorov-scale filtering.

and Goody, 1968; *Blumsack et al.*, 1973; *Pallman*, 1983; *Ye et al.*, 1990; *Savijärvi*, 1991b; *Haberle et al.*, 1993a; *Savijärvi and Siili*, 1993; *Odaka*, 2001]. The 1-D models still serve as an efficient tool, however, for interpreting the near-surface local conditions at the sites of various landers [e.g., *Savijärvi et al.*, 2004; *Savijärvi and Kauhanen*, 2008; *Savijärvi and Määttänen*, 2010].

[99] All of these atmospheric models must provide a representation for the very active turbulence in the PBL of Mars. In practice, the turbulence is usually presented as a diffusive (mixing) process in all prognostic equations, but there is a wide range of approaches that have been adopted to achieve this.

5.1. Bulk and Mixing Length Parameterized Models of the Martian PBL

5.1.1. First-Order Closure Models

[100] The first Martian atmospheric models, roughly before the 1990s, used either a bulk approach (treating the whole PBL as a single layer) or a mixing length closure, whereby the vertical turbulent diffusion coefficients, K_ν, are given at a few layers through the PBL as the triple product of a squared mixing length, ℓ (hence the name), the current wind shear, and a dimensionless, semiempirical stability factor, $f(Ri)$, that is a function of a suitably defined Richardson number, based on the Monin-Obukhov similarity theory and calibrated using measurements on the Earth,

$$K_\nu = \ell^2 \left| \frac{\partial \mathbf{V}}{\partial z} \right| f(Ri). \qquad (24)$$

The mixing length, $\ell(z)$, is a measure of the diameter of the typical turbulent eddies. It is usually assumed to increase linearly with height near the surface and to asymptote higher up toward a constant (the asymptotic length scale [*Blackadar*, 1957]), which on Earth is of the order of 1/10 of the convective boundary layer height. Ri in this case could be the local bulk Richardson number (see section 2), which provides a measure of hydrodynamic stability dependent on the current vertical gradients of the temperature and wind speed at each height, or an equivalent measure (such as Ri' or Ri_g; compare equations (10) and (16)).

[101] These diagnostic first-order closure methods were based on their Earth counterparts. They appear to work quite well on Mars (compare section 3), thus broadly confirming the planetary validity of the classical similarity theory. They are still adequate if one is mainly interested in the simulation of the basic variables (e.g., grid-scale wind and temperature) and less so in the details of the subgrid-scale turbulence. In a test at York University, where higher-order closures and a mixing length–type first-order closure were compared in the same 1-D model framework at the Mars Pathfinder conditions [*Weng et al.*, 2006], the resulting diurnal simulations of the near-surface mean winds and temperatures were quite alike and found to be quite close to the MPF observations. However, the first-order closure methods do not provide a lot of information about the structure of the turbulence itself. Hence the so-called TKE and other higher-order closures and LES and DNS have recently become popular (see sections 5.2 and 5.3).

5.1.2. Physics of the Martian PBL as Revealed by First-Order Closure Models

[102] The in situ lander observations indicate that the Martian boundary layer is, at least in the safe, smooth, and flat landing sites explored to date, quite repetitive in its strong diurnal and annual cycles, since it is superadiabatic in the daytime sunshine and subadiabatic with a steep surface inversion every night [e.g., *Smith et al.*, 2006]. This is partly because clouds in the Martian atmosphere are absent or thin. Clouds do not, therefore, moderate the solar and thermal radiation to the same extent as on Earth, although the ubiquitous suspension of mineral dust tends (in large concentrations) to take over the role of clouds on Mars.

[103] The early first-order closure models were able to reveal that the Martian PBL, and especially its surface layer, is strongly controlled by radiative heating and cooling (i.e., radiative flux divergences): carbon dioxide at the 15 μm
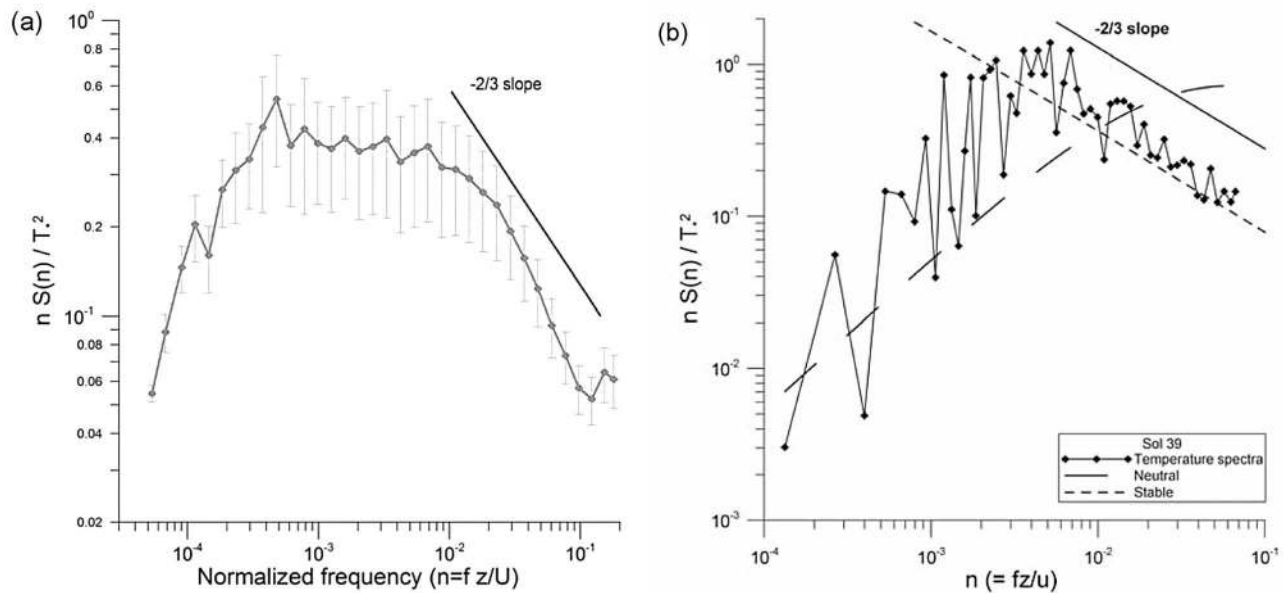
Figure 18. Spectra of temperature from the Phoenix lander [*Davy et al.*, 2010], normalized by T^* and plotted versus the normalized frequency, $n = fz/\overline{u}$, with z being the measurement height, $\overline{u}$ being the mean speed, and f being the frequency (in Hz). (a) A composite daytime (unstable) spectrum, averaged over 32 sols. (b) A sample nocturnal (stable) spectrum. The model spectrum is indicated by a broken line. Also here the low-pass sensor response is seen, together with some shortcomings of the modeling of the temperature. Note that no analytical model curve for unstable temperature spectra has ever been formulated. However, the approach toward the spectral slope of the inertial subrange ($-2/3$) is indicated for both unstable and stable conditions, confirming the existence of this important turbulent feature on Mars.

band and airborne dust at other IR wavelengths readily adopt the daytime heat and nighttime cold of the sand-like ground (regolith) via absorption of thermal radiation emitted by the hot or cold regolith typical, e.g., of the Sahara desert. They also absorb solar radiation. This adds an extra daytime heating effect, which is small in relatively dust-free conditions but can be strong during heavy dust loads. Thus, the radiation and ground heat conduction schemes should be of relatively high accuracy in all Martian atmospheric models and especially so for PBL models intended for Mars. Perhaps the largest source of inaccuracy in PBL modeling is our limited knowledge of the local amounts and current radiative properties of the Martian dust. Water vapor can also have a nonnegligible effect on both solar and thermal radiative transfer in the Martian PBL [e.g., *Savijärvi*, 1991a; *Määttänen and Savijärvi*, 2004]. But since the absolute humidity on Mars is small, most models have so far ignored water vapor and other trace gases in their radiation schemes. The CO_2 and water ice-covered winter polar caps form a special, often cloud-topped, arctic PBL.

[104] The small air density, which makes the Martian air react rapidly and strongly to the vertical radiative flux divergences, also makes the turbulent fluxes relatively small in magnitude so one might be tempted to think that turbulence is ineffective on Mars. But in fact the low density of the air, together with low gravity on Mars, contributes to the vertical turbulent flux divergences actually being quite strong, to the extent that the Martian extrapolar convection and turbulence are more vigorous than those on the Earth

(see section 3), thereby mixing the IR-induced daytime heat content and nighttime coldness of the surface layer upward very effectively. The typical depth of the afternoon Martian convective boundary layer is about 7–8 km at low latitudes (2–3 km on Earth), while the nighttime inversion is about 0.5 km thick (compare with values of 100–200 m on Earth). The strong daytime turbulence also mixes dust from the ground to the air, feeding, e.g., local dust devils and regional and global dust storms. This creates an interesting and poorly known arena for various feedback effects on many scales between the dust, radiation, temperature and wind distributions.

[105] An interesting feature of the midday superadiabatic surface layer of Mars is that it appears to be so strongly heated from below by IR radiation that turbulence is actually forced to cool it down. Therefore, the turbulent heat fluxes most probably attain their morning and midday maxima not at the surface, as on Earth, but a few hundreds of meters aloft (see Figure 3).

5.2. TKE Closures for the Martian PBL

[106] Many models of Martian circulation employ ReSMs for parameterization of the turbulent boundary layer. As explained earlier, Martian and terrestrial boundary layers are similar in many aspects and so they can be described by similar models. Indeed, the Reynolds stress modeling approach used in terrestrial circulation models has been adopted in several leading Martian atmospheric models, e.g., by *Forget et al.* [1999] and *Rafkin et al.* [2001]. Despite the

portability of terrestrial ReSMs to the Martian environment, there has been a notable absence of a comprehensive source of information on the ReSM technique for the Martian community. One of the purposes of this paper is to mitigate this omission and provide the community of Mars researchers with a state-of-the-art review on those aspects of the Reynolds stress modeling approach, as applied to the terrestrial atmosphere and ocean, that can be applied to Mars.

[107] The Reynolds stress models rely upon the Reynolds averaging of the governing equations and a set of closure assumptions relating unknown correlations to the known ones as well as to the mean fields. ReSM is a powerful tool for modeling turbulent flows that has been used extensively in engineering, environmental, and geophysical sciences, and its foundations have been outlined in numerous review articles and books [e.g., *Tennekes and Lumley*, 1972; *Mellor and Herring*, 1973; *Monin and Yaglom*, 1975; *Mellor and Yamada*, 1982; *Pope*, 2005; *Alfonsi*, 2009]. All ReSM models are based upon the Reynolds decomposition of fluctuating flow characteristics, such as the instantaneous velocity, $\tilde{u}_i = U_i + u_i$, where $\overline{\tilde{u}_i} = U_i$ is either the ensemble- or time- or space-averaged velocity and u_i is its fluctuating counterpart. The subtleties of the averaging have been extensively analyzed, e.g., by *Monin and Yaglom* [1975] or *Pope* [2005], and will not be discussed further. We shall refer to either of these averagings as Reynolds averaging and assume that they are used consistently throughout the derivations.

[108] The application of Reynolds averaging to the governing equations in the Boussinesq approximation and utilizing Einstein's summation rule yield [*Galperin et al.*, 1989]

$$\frac{DU_i}{Dt} + \epsilon_{ikl}f_k U_l = \frac{1}{\rho_0}\frac{\partial}{\partial x_l}(-\overline{u_i u_l}) - \frac{1}{\rho_0}\frac{\partial P}{\partial x_i} + g_i\frac{\rho}{\rho_0}, \quad (25)$$

$$\frac{D\Theta}{Dt} = \frac{\partial}{\partial x_l}(-\overline{u_l \theta}), \quad (26)$$

$$\frac{\partial U_i}{\partial x_i} = 0, \quad (27)$$

where Θ and θ are the mean and fluctuating potential temperatures, respectively, ρ is the density, ρ_0 is a constant reference density, P is the mean pressure, $f_k = 2\Omega(0, \cos\phi, \sin\phi)$ is the Coriolis vector, Ω is the angular velocity of the planet's rotation, and $g_i = (0, 0, -g)$ is the acceleration due to gravity.

[109] Reynolds averaging of the governing equations for turbulent momentum and heat fluxes, $\overline{u_i u_j}$ and $\overline{u_i \theta}$, respectively, encounter the classical problem of turbulence closure since those equations involve many unknown correlations that cannot be "closed" at any level of correlation, i.e., a closed expression for the unknown correlations cannot be derived without introducing additional assumptions. The most problematic correlations are those involving the pressure because it is a nonlocal variable [e.g., *Mellor and Herring*, 1973]. Two approaches have been developed to model the pressure-velocity correlation terms, one by *Launder et al.* [1975] and *Zeman and Lumley* [1979] (we shall refer to these as LRR models), and the other by *Mellor*

and Herring [1973] and *Mellor and Yamada* [1974] (hereafter referred to as MY models). Models of the LRR family are more comprehensive and more complicated than their MY counterparts. The LRR approach was initially designed for engineering flows with weak or no shear, while the MY models were more commonly applied to geophysical and environmental flows with strong shear. Later, the LRR models were also adapted to geophysical flows [e.g., *Canuto et al.*, 2001; *Cheng et al.*, 2002]. Models of intermediate complexity have also been proposed [e.g., *Kurbatskiy and Kurbatskaya*, 2006, 2009]. Note that the closure constants in both families of closures have been assumed invariant [e.g., *Lewellen*, 1977], although for some applications the constants were allowed to be flow dependent [e.g., *Ristorcelli*, 1997; *Girimaji*, 2000]. The closures used in current models of the Martian circulation are almost exclusively of the MY family [*Forget et al.*, 1999; *Rafkin et al.*, 2001; *Moudden and McConnell*, 2005], and so we shall only consider models of this class hereafter.

[110] Fully prognostic equations for all Reynolds stresses, $\overline{u_i u_j}$, and turbulent heat fluxes, $\overline{u_i \theta}$ in the MY approach can be classified in terms of the departure from isotropy quantified by the expressions

$$\overline{u_i u_j} = \left(\frac{\delta_{ij}}{3} + a_{ij}\right)q^2, \qquad a_{ii} = 0, \quad (28)$$

$$\overline{u_i \theta} = b_i q\left(\overline{\theta^2}\right)^{1/2}, \quad (29)$$

where $q^2 = \overline{u_k^2} = 2E_{KT}$, E_{KT} is TKE and a_{ij} and b_i are tables of nondimensional coefficients. Let us introduce the following notations:

$$a \equiv \| a_{ij} \|, \quad (30)$$

$$b \equiv \| b_i \|, \quad (31)$$

where $\|.\|$ denotes a matrix norm [*Mellor and Yamada*, 1974; *Galperin et al.*, 1988]. Assuming a and b are small but of the same order of magnitude, i.e., $O(a) = O(b)$, and systematically neglecting terms of progressively higher order in a and b, one establishes the MY hierarchy of turbulence closure models [*Mellor and Yamada*, 1974]. By neglecting all terms up to $O(a^2)$ and $O(b^2)$, one arrives at the quasi-equilibrium turbulence energy model [*Galperin et al.*, 1988], which could be classified as the level 2 model in the MY hierarchy. For this model, the Reynolds stresses and turbulent heat fluxes are related by algebraic equations, first for the Reynolds stresses themselves,

$$\overline{u_i u_j} = \frac{\delta_{ij}}{3}q^2 - \frac{3\ell_1}{q}\left[\overline{u_i u_k}\frac{\partial U_j}{\partial x_k} + \overline{u_j u_k}\frac{\partial U_i}{\partial x_k} - C_1 q^2\left(\frac{\partial U_i}{\partial x_j} + \frac{\partial U_j}{\partial x_i}\right) \right.$$
$$\left. + \beta\left(g_i\overline{u_j \theta} + g_j\overline{u_i \theta}\right) + f_k\left(\epsilon_{ikl}\overline{u_l u_j} + \epsilon_{jkl}\overline{u_l u_i}\right) + \frac{2q^3}{3\Lambda_1}\delta_{ij}\right], \quad (32)$$

for the heat flux,

$$\overline{u_i \theta} = \frac{3\ell_2}{q}\left(\overline{u_k u_i}\frac{\partial\Theta}{\partial x_k} + \overline{\theta u_k}\frac{\partial U_i}{\partial x_k} + \beta g_i\overline{\theta^2} + f_k\epsilon_{ikl}\overline{u_l \theta}\right), \quad (33)$$

and for the temperature variance,

$$\overline{\theta^2} = -\frac{\Lambda_2}{q}\overline{u_k\theta}\frac{\partial\Theta}{\partial x_k}. \tag{34}$$

The TKE is given via a prognostic equation for q^2,

$$\frac{Dq^2}{Dt} - \frac{\partial}{\partial x_k}\left(q\ell S_q\frac{\partial q^2}{\partial x_k}\right) = -2\overline{u_k u_l}\frac{\partial U_k}{\partial x_l} - 2\beta g_k\overline{u_k\theta} - \frac{2q^3}{\Lambda_1}, \tag{35}$$

where β is the thermal expansion coefficient, $\beta = (\partial\rho/\partial\theta)_p/\rho_0$, S_q is the vertical nondimensional exchange coefficient for q^2 (usually taken to be equal to 0.2 [*Mellor and Yamada*, 1982]), and various turbulence length scales are related to the master macroscale, ℓ, following *Mellor and Yamada* [1982],

$$(\ell_1, \ell_2, \Lambda_1, \Lambda_2) = (A_1, A_2, B_1, B_2)\ell, \tag{36}$$

where

$$(A_1, A_2, B_1, B_2) = (0.92, 0.74, 16.6, 10.1). \tag{37}$$

It can be shown [e.g., *Mellor*, 1975] that the remaining constant, C_1, is not independent but is related to the other constants by

$$C_1 = \frac{1}{3}\left(1 - 6A_1B_1^{-1} - A_1^{-1}B_1^{-1/3}\right) = 0.08. \tag{38}$$

In the MY model, the dissipation rate, ϵ, is given by

$$\epsilon = \frac{q^3}{B_1\ell}. \tag{39}$$

[111] The Coriolis terms in equations (32) and (33) significantly complicate the algebra. These terms were investigated by *Galperin et al.* [1989] for the case of stable stratification and by *Hassid and Galperin* [1994] for the cases of neutral and unstable stratification. It was found for the stable case that the contribution of the Coriolis terms does not exceed about 10% of the total stress, while for neutral and unstable stratification, the magnitude of the Coriolis terms can be large. These conclusions could be important for the daytime Martian atmospheric boundary layer, which is often strongly unstable and very deep. Despite these findings, the explicit Coriolis terms in the Reynolds stress and heat flux equations are usually neglected. The effect of the horizontal component of the Coriolis parameter on the mean flow has been considered in a relatively small number of studies, among them *Kasahara* [2003], *Dellar and Salmon* [2005], and *Gerkema et al.* [2008], where it was shown that it could be significant though again usually neglected in most implementations.

[112] In the boundary layer approximation, using equations (32)–(35) with the explicit Coriolis terms neglected, the vertical turbulent fluxes of momentum and temperature can be represented in the following format:

$$-(\overline{uw}, \overline{vw}) = K_M\left(\frac{\partial U}{\partial z}, \frac{\partial V}{\partial z}\right), \tag{40}$$

$$-\overline{w\theta} = K_H\frac{\partial\Theta}{\partial z}, \tag{41}$$

where U and V are the components of the mean horizontal velocity, z is the vertical coordinate, K_M is the vertical eddy viscosity, and K_H is the vertical eddy thermal diffusivity. K_M and K_H are generally given by mixing length parameterizations of the form $K_M = q\ell S_M$ and $K_H = q\ell S_H$, where S_M and S_H are nondimensional stability functions. *Galperin et al.* [1988] showed that, in the quasi-equilibrium turbulence energy model, S_M and S_H are given by

$$S_M = \frac{B_1^{-1/3} - 3A_1A_2G_HP_1}{(1 - 9A_1A_2G_H)P_2}, \tag{42}$$

$$S_H = A_2\left(1 - 6A_1B_1^{-1}\right)P_2^{-1}, \tag{43}$$

where

$$P_1 = (B_2 - 3A_2)\left(1 - 6A_1B_1^{-1}\right) - 3C_1(B_2 + 6A_1), \tag{44}$$

$$P_2 = 1 - 3A_2G_H(6A_1 + B_2), \tag{45}$$

$$G_H = -\left(\frac{l}{q}\right)^2\beta g\frac{\partial\Theta}{\partial z} = -\left(\frac{lN}{q}\right)^2, \tag{46}$$

with N being the Brunt-Väisälä frequency. These equations are assumed valid for both stable and unstable stratification. Using somewhat modified closure assumptions but staying within the MY hierarchy, *Kantha and Clayson* [1994] obtained slightly different equations for S_M and S_H.

[113] Calculation of K_M and K_h relies upon the precise specification of the turbulence macroscale, ℓ, which presents a formidable problem for turbulence modeling because the macroscale does not obey any known conservation law. As a result, all existing models for ℓ, either prognostic or diagnostic, are empirical. For neutrally stratified atmospheric boundary layers, Blackadar's algebraic equation has been commonly used [*Blackadar*, 1962],

$$\ell = \ell_B = \kappa z/(1 + \kappa z/\ell_0), \tag{47}$$

where ℓ_0 is a reference length scale. This equation ensures a smooth transition of ℓ from κz in the logarithmic velocity profile near the solid ground to a constant value at the top of the boundary layer. For the Martian atmosphere, *Forget et al.* [1999] fix ℓ_0 at 160 m while *Moudden and McConnell* [2005] set ℓ_0 to 200 m. *Rafkin et al.* [2001] use a different definition of ℓ_B,

$$\ell_B = \frac{\kappa(z + z_0)}{1 + \kappa(z + z_0)/\ell_0}, \tag{48}$$

where, following *Mellor and Yamada* [1974],

$$\ell_0 = 0.1\frac{\int_0^h zq\,dz}{\int_0^h q\,dz}, \tag{49}$$

and where h is the top of the boundary layer. A similar definition of ℓ_0 was used by *Haberle et al.* [1993a], but they employed a coefficient of 0.2 instead of 0.1.

[114] In stably or neutrally stratified boundary layers and in flows that combine layers with different senses of

stratification, Blackadar's formulation fails and more a sophisticated formulation may be required. In stably stratified boundary layers, the size of the overturning eddies is conditioned by their kinetic energy exceeding the potential energy of the background. This leads to the length scale limitation first introduced by *Deardorff* [1976] and then used in turbulence models by *André et al.* [1978], *Hassid and Galperin* [1983], *Galperin et al.* [1988], and many others,

$$\ell \leq \ell_s = 0.53 \frac{q}{N}. \tag{50}$$

The turbulence macroscale in stably stratified boundary layers can either be clipped to ℓ_s [*Galperin et al.*, 1988; *Rafkin et al.*, 2001] or determined from the equation

$$\ell^{-1} = \ell_B^{-1} + \ell_s^{-1}, \tag{51}$$

which ensures a smooth transition from the Blackadar formulation to ℓ_s in regions dominated by stable stratification. Some models take into account the dependence of ℓ on the vertical Coriolis parameter, f, by adding another term to equation (51),

$$\ell^{-1} = \ell_B^{-1} + f/C_f q + \ell_s^{-1}, \tag{52}$$

where C_f is a constant [see, e.g., *Zilitinkevich et al.*, 2007, and references therein]. Combined with equation (46), inequality (50) imposes a limitation on G_H,

$$G_H \geq -\left(0.53^2\right) = -0.28. \tag{53}$$

[115] In the original MY models, the stability functions, S_M and S_H, depended not only on G_H but also on the non-dimensional mean shear parameter, G_M, given by

$$G_M = \left(\frac{\ell}{q}\right)^2 \left[\left(\frac{\partial U}{\partial z}\right)^2 + \left(\frac{\partial V}{\partial z}\right)^2\right] = \left(\frac{\ell S}{q}\right)^2, \tag{54}$$

where S is the mean shear magnitude. In practice, however, these formulations led to spurious oscillations and instabilities [*Mellor and Yamada*, 1982; *Hassid and Galperin*, 1983]. The quasi-equilibrium turbulence energy model by *Galperin et al.* [1988] was designed to alleviate this problem. Various aspects of these instabilities were discussed by *Deleersnijder and Luyten* [1994], *Mellor* [2003], *Deleersnijder and Burchard* [2003], and *Umlauf and Burchard* [2005]. An insightful study by *Deleersnijder et al.* [2008] attributes these oscillations to the ways S_M and S_H depend on the mean gradients of the velocity and temperature, i.e., G_M and G_H. To highlight the source of the instability, they consider a simple scalar diffusion equation in the variable ψ,

$$\frac{\partial \psi}{\partial t} = \frac{\partial}{\partial z}\left(\lambda \frac{\partial \psi}{\partial z}\right), \tag{55}$$

where λ is the diffusivity. It is assumed that $\lambda = \lambda(\psi_z)$, $\psi_z \equiv \frac{\partial \psi}{\partial z}$, and λ is positive definite. For ψ_z, a corresponding diffusion equation can also be derived,

$$\frac{\partial \psi_z}{\partial t} = \frac{\partial}{\partial z}\left(\tilde{\lambda} \frac{\partial \psi_z}{\partial z}\right), \tag{56}$$

where $\tilde{\lambda}$ is the "effective diffusivity;" $\tilde{\lambda} = \lambda + \frac{\partial \lambda}{\partial \psi_z}\psi_z$. Unlike λ, it is possible for $\tilde{\lambda}$ to become negative, giving rise to an unbounded growth of ψ_z, even though ψ itself remains bounded in time. As a result, ψ may exhibit small-scale, finite-amplitude oscillations that appear as an instability of the large-scale flow. *Deleersnijder et al.* [2008] designed a criterion which allows one to determine whether or not a particular dependence, $[S_H(G_M, G_H), S_M(G_M, G_H)]$, would lead to oscillations of this kind. This is a useful criterion as it makes it possible to screen various stability functions and select those that will not cause unphysical oscillations of the solution. Among other interesting results, this criterion demonstrates that the stability functions of the quasi-equilibrium turbulence energy model by *Galperin et al.* [1988] can never cause spurious oscillations of this kind.

[116] The gradient Richardson number, Ri_g (compare equation (16)), is an important characteristic parameter for stratified turbulence that determines the strength of stratification with respect to vertical shear. Under strongly stable conditions, a critical value of Ri (denoted as Ri_{cr}) may be attained at which turbulent mixing is often assumed to be fully suppressed. In MY models, Ri_{cr} is under 0.2, leading to underpredicted mixing in some situations [*Martin*, 1985; *Simpson et al.*, 1996; *Rippeth*, 2005]. *Galperin et al.* [2007] discussed the general notion of a Ri_{cr}, based upon recent observational and theoretical studies that considered the effects of nonstationarity, internal waves, and flow anisotropization. They concluded that all these factors preclude the full laminarization of turbulence and thus make the concept of a Ri_{cr} devoid of its conventional meaning. Consequently, they suggested that the use of Ri_{cr} as a criterion of turbulence extinction should be avoided.

[117] Turbulence intensity in stably stratified flows can also be judged by another parameter, the buoyancy Reynolds number, $Re_b = \epsilon/\nu_0 N^2$, with ν_0 being the molecular viscosity [see, e.g., *Galperin and Sukoriansky*, 2010, and references therein]. For $Re_b = O(1)$, vertical turbulent mixing may become laminarized. However, in horizontal planes, the mixing can still be much larger than in laminar flows. Conclusions similar to those of *Galperin et al.* [2007] on the absence of a meaningful Ri_{cr} were also reached by *Zilitinkevich et al.* [2007] based upon the total energy approach, with the total energy being the sum of kinetic and potential energies of turbulent fluctuations. A number of ReSMs with no Ri_{cr} were subsequently developed [e.g., *Canuto et al.*, 2008; *Violeau*, 2009; *Alexakis*, 2009; *Kantha and Carniel*, 2009; *Kitamura*, 2010].

[118] In the case of unstable stratification, a super-equilibrium balance equation for q^2 (with all tendency terms dropped), equation (35), yields

$$S_M G_M + S_H G_H = B_1^{-1}. \tag{57}$$

Galperin et al. [1988] showed that equation (57) yields a limitation on G_H for the case of unstable stratification,

$$G_H \leq [A_2(12A_1 + 3B_1 + 3B_2)]^{-1} = 0.0233, \tag{58}$$

which can be used as a clipping condition in simulations. Even though models of the MY family can be, and have

been, applied to flows with unstable stratification and strong convection, *Forget et al.* [1999] express some doubts about the validity of the model in such conditions. *Canuto et al.* [2005] explored the limitations of models of the MY family in depth and concluded that the condition (58) essentially imposes a limitation on the size of the eddies that can take part in convective transport. This limitation forces the model to include local interactions only and filters out the non-locality which would otherwise be allowed by the third-order and higher-order correlations. To overcome this shortcoming, *Canuto et al.* [2005] suggest that the third-order and possibly the higher-order correlations should be included in MY-type models.

[119] The effects of the nonlocality in convective flows are partially captured by the length scale specification, which must respond to ascending and descending motions of air parcels typical of convection. A widely accepted formulation of ℓ for turbulent convection goes back to works by *André et al.* [1978], *André and Lacarrére* [1980], *Bougeault and André* [1986] and *Bougeault and Lacarrére* [1989]. It is postulated that for each level, z, a parcel with a E_{KT} corresponding to that level (equal to $E_{KT}(z)$) can travel upward and downward before being damped by buoyancy forces. One defines ℓ_{up} and ℓ_{down} according to

$$\int_z^{z+\ell_{up}} \beta g[\Theta(z) - \Theta(z')]dz' = E_{KT}(z), \qquad (59a)$$

$$\int_{z-\ell_{down}}^z \beta g[\Theta(z') - \Theta(z)]dz' = EKT(z). \qquad (59b)$$

If a parcel encounters on its way a layer with stable stratification, then equations (59a) and (59b) readily provide the limitation (50). Keeping in mind a possible large disparity between ℓ_{up} and ℓ_{down} and the need to keep the bias toward smaller values, ℓ is related to ℓ_{up} and ℓ_{down} via $\ell_c = \min(\ell_{up}, \ell_{down})$. In realistic situations, boundary layers combine regions with both stable and unstable stratifications and to reflect this, the length scale equation (52) should be supplemented by the term ℓ_c^{-1}. Such an equation has been widely used in atmospheric models and numerical weather prediction in the framework of the so-called CBR model [*Cuxart et al.*, 2000].

[120] Specification of the turbulence length scale in flows with multiple regimes has been a persistently difficult problem for modeling. Aside from the algebraic formulations of the kind described earlier, another widely used approach employs prognostic equations for quantities related to ℓ, such as the dissipation rate, ϵ. Models utilizing prognostic equations for E_{KT} and ϵ are often known as $K - \epsilon$ models [e.g., *Rodi*, 1987; *Pope*, 2005]. *Mellor and Yamada* [1982] consider a prognosic equation for the quantity $q^2\ell$, which can be constructed by analogy with the equation for q^2,

$$\frac{D(q^2\ell)}{Dt} - \frac{\partial}{\partial z}\left(q\ell S_q \frac{\partial q^2\ell}{\partial z}\right) = \ell(E_1 P_s - E_3 P_b) - \frac{q^3}{B_1}\left[1 + E_2\left(\frac{\ell}{\kappa z}\right)^2\right],$$

$$(60)$$

where $P_s = K_M S^2$ and $P_b = K_H N^2$ represent the mechanical production and the buoyant destruction of the turbulence energy, respectively, ϵ is the dissipation rate given by equation (39), and the constants E_1, E_2, and E_3 are 1.8, 1.33, and 1.8, respectively. This equation is quite popular in oceanographic modeling and has been employed, for instance, in the Princeton Ocean Model (POM; http://www.aos.princeton.edu/WWWPUBLIC/htdocs.pom/). The values of these constants were reevaluated by *Burchard* [2001] using simulations of three oceanic flows, and their recommendation was to increase E_3 to about 5. *Umlauf and Burchard* [2003] formulated a generic transport equation for a quantity $\psi = (c_\mu^0)^p E_{KT}^m \ell^n$ that, with a proper choice of parameters p, m, and n, reverts to equations for either ϵ or $q^2\ell$ or a quantity $\omega \propto \epsilon/E_{KT}$ discussed, e.g., by *Wilcox* [1988] and *Umlauf et al.* [2003]. Note that, even though great progress has been achieved in Reynolds stress modeling using prognostic length scale equations, this approach is mostly local and thus may have difficulties in convective boundary layers where ℓ becomes nonlocal, as illustrated by equations (59a) and (59b).

[121] As mentioned earlier, in convective flows proper accounting for the effects of buoyancy-driven convection cells and the ensuing nonlocality requires modification, not only of the turbulence length scale equation but also of the equations for turbulence correlations [*Moeng and Wyngaard*, 1989; *Holtslag and Boville*, 1993]. *Deardorff* [1972], *Holtslag and Moeng* [1991], *Wyngaard and Weil* [1991] and *Canuto et al.* [2005] introduced ad hoc non-local terms that improved their models' performance. However, a comprehensive approach to overcome the shortcomings of local models entails consideration of the balance equations for the third and fourth moments, as was done, e.g., by *Canuto* [1992], *Canuto et al.* [2001], *Cheng and Canuto* [1994], *Cheng et al.* [2005], *Zilitinkevich et al.* [1999], *Gryanik et al.* [2005], and *Ferrero and Colonna* [2006]. A recent study by *Ferrero and Racca* [2004] demonstrated that accounting for nonlocal effects via higher-order correlations can improve simulations of the boundary layer height, even in the case of neutral stratification.

[122] The use of turbulence schemes in atmospheric models requires their consistency with the imposed boundary conditions. A conventional method to derive such boundary conditions near the underlying surface is to use a constant-flux layer approximation between the surface and the first grid point and to employ Monin-Obukhov similarity functions (Φ_q, where $q = m, h$ etc.; see section 2) to calculate the required values of the mean profiles. *Mellor* [1973] showed how Monin-Obukhov similarity functions can be derived directly from the turbulence model. However, in many cases these functions are taken from observations and so the mismatch between the observed functions and those obtained from the turbulence model may introduce spurious fluxes of momentum, heat, and other quantities.

[123] A new family of ReSMs was developed recently, based upon a spectral approach which is an alternative to the Reynolds stress modeling [*Sukoriansky et al.*, 2005b]. This approach has been coined a quasi-normal scale elimination, or QNSE. Within this theory, internal waves and turbulence

are treated as one entity rather than as an ad hoc dichotomy. QNSE provides a rigorous procedure of successive coarsening of the system's domain of definition that produces the effective, scale-dependent, vertical viscosity (K_M) and thermal diffusivity (K_H) as well as their horizontal counterparts. Dependent upon the range of eliminated scales, QNSE provides either subgrid-scale parameterization for LESs or an equivalent of an ReSM [*Sukoriansky et al.*, 2005b, 2006]. In the latter case, the eddy viscosities and eddy diffusivities become functions of either the local gradient Richardson number, *Ri*, given by (9), or the Froude number, $Fr = \epsilon/NE_{KT}$. One of the important advantages of the QNSE model is the absence of the critical Richardson number, Ri_{cr} [*Sukoriansky et al.*, 2005b; *Galperin et al.*, 2007]. The QNSE-based expressions for K_M and K_H have been successfully tested in both $K - \epsilon$ and $K - \ell$ applications [*Sukoriansky et al.*, 2005a, 2006; *Sukoriansky and Galperin*, 2008]. Along with the QNSE-based Monin-Obukhov similarity functions for the near-surface layer, these expressions were implemented in recent releases of the Weather Research and Forecasting (WRF) model for Earth applications. We note, however, that a version of the WRF model known as PlanetWRF has been in use recently for global simulations of the Martian atmosphere [*Richardson et al.*, 2007], and other versions are now being used for mesoscale and LES modeling for Mars [*Spiga and Forget*, 2009; *Spiga et al.*, 2010].

5.3. Large Eddy Simulations of the Martian

5.3.1. General Principles

[124] As described in section 4, the exploration of Mars from space has shown the variety and intensity of Martian boundary layer (BL) processes, with daytime convective heat fluxes some 3 times larger than in the terrestrial environment [*Sutton et al.*, 1978], wide dust devils extending to high altitudes [*Thomas and Gierasch*, 1985], well-organized convective cloud streets [*Malin and Edgett*, 2001], superadiabatic daytime and ultrastable nighttime near-surface gradients of temperature [*Schofield et al.*, 1997], large turbulent fluctuations of near-surface temperatures [*Smith et al.*, 2006] and a mixed layer depth of the same order of magnitude as the atmospheric scale height [*Hinson et al.*, 2008].

[125] Such a context of observational achievements has motivated the development of a number of dedicated three-dimensional mesoscale models for Mars [*Rafkin et al.*, 2001; *Tyler et al.*, 2002; *Toigo and Richardson*, 2002; *Richardson et al.*, 2007; *Kauhanen et al.*, 2008; *Spiga and Forget*, 2009] so as to resolve Martian circulations at higher resolution than possible with Global Climate Models (GCMs). These efforts have given birth to powerful simulators of the Martian atmospheric circulations at both the mesoscale (hundreds of kilometers to 1 km) and the microscale (1 km to hundreds of meters). Mesoscale models couple nonhydrostatic dynamical cores, originally developed for terrestrial regional climate modeling, with physical parameterizations of Martian dust, CO_2, and H_2O cycles, developed for Mars GCMs. Of particular interest in BL studies is the use of mesoscale models for so-called LESs (also referred to as microscale modeling

or turbulence-resolving simulations). In these simulations, the grid spacing is reduced to a few tens of meters so as to resolve the larger turbulent eddies, which are responsible for most of the energy transport within the BL [see, e.g., *Lilly*, 1962]. Thus, besides the obvious realistic improvement gained by the 3-D computations, LES allows for fewer initial assumptions and parameterizations than single column models.

5.3.2. LES Standard Settings

[126] In three-dimensional LES, the numerical integration of the atmospheric fluid dynamic equations is performed through the dynamical core. In contrast to GCMs, integrations in mesoscale dynamical cores are performed not over the whole planetary sphere but in a limited domain over an area of interest. Martian models are adapted from carefully tested dynamical cores developed for the Earth, which integrate the fully compressible, nonhydrostatic Navier-Stokes equations. When fine-scale meteorological motions are resolved, vertical wind accelerations can become comparable to the acceleration due to gravity. Hence hydrostatic balance cannot be assumed in those equations as is typically the case in GCMs.

[127] The dynamical core is coupled with (most often 1-D) parameterization schemes, in order to compute physical processes at each grid point specific to the considered planetary environment. Mesoscale models used for LES applications usually come with the full range of physics developed for Martian GCMs, in particular, calculations of the diabatic forcing of atmospheric circulations (radiative transfer, soil thermal diffusion, etc.). As was pointed out for parameterized single-column modeling studies, radiation plays a prominent role in the energy budget of the Martian BL [*Haberle et al.*, 1993b; *Savijärvi*, 1999; *Davy et al.*, 2009]. Thus, including realistic computations of radiative transfer processes by CO_2 and dust appears necessary in Martian LES, while it may be less crucial in terrestrial LES.

[128] When subgrid-scale dynamical processes are not resolved by the dynamical core, their effects are parameterized in the model's physical schemes. Although BL mixing through convective plumes is predominantly resolved by LES, turbulent phenomena at smaller scales than typical LES grid spacings (i.e., few tens of meters) are still left unresolved. In LES, handling subgrid-scale BL mixing requires particular attention (see section 5.1.2); for Martian applications, the adopted strategy is usually similar to what is done in terrestrial LES [see, e.g., *Moeng et al.*, 2007; *Basu et al.*, 2008]. Some of the physical parameterizations used in coarser-resolution simulations, however, are not suitable for the very high-resolution LES. In GCMs, in order to ensure numerical stability and to account for subgrid-scale mixing processes insufficiently handled in the BL scheme, it is usually necessary to modify and adjust any unstable layer with negative vertical potential temperature gradients (a common near-surface situation during Martian afternoons) into a neutral equivalent [*Rafkin*, 2003]. But the use of convective adjustment is not generally needed in LES since the model explicitly resolves turbulent convective motions:

the mixed layer is a direct result of the model's dynamical integrations.

[129] The first model level is located a few meters above the ground (1–4 m), which means surface layer processes also need to be parameterized in LES. Surface layer values for sensible heat flux H_s and friction velocity u_* are passed on to the turbulent diffusion scheme where they modify momentum and potential temperature at the lowest grid levels [*Moeng et al.*, 2007]. Sensible heat flux H_s is evaluated by the bulk aerodynamic formula

$$H_s = \rho c_p u_* \theta_*, \qquad (61)$$

(compare section 2), where ρ is atmospheric density and c_p is specific heat capacity. At each grid point and time step, θ_* is effectively the temperature difference between surface and first atmospheric layer (at altitude z_1 above ground), and friction velocity u_* is taken to be the product of wind velocity in the first layer (background wind plus resolved turbulent winds) and the von Kármán drag coefficient $C_d = [\kappa/\ln(z_1/z_0)]^2$ with surface roughness $z_0 = 1$ cm.

[130] So far as initial and boundary conditions are concerned, LES are generally idealized numerical experiments rather than "real-case" mesoscale simulations. Periodic boundary conditions are often used to simulate the situation of an infinite flat plane. Surface properties (topography, albedo, thermal inertia) are set as constants over the whole simulation domain that typically is smaller than the resolution element of available observations. Surface static data are extracted from maps derived from recent Martian spacecraft measurements, such as the 64 pixel per degree (ppd) MOLA topography [*Smith et al.*, 2001], 8 ppd MGS TES albedo [*Christensen et al.*, 2001] and 20 ppd TES thermal inertia [*Putzig and Mellon*, 2007]. Large-scale circulations are prescribed through the same initial temperature and wind profiles being prescribed at any grid point. Temperature profiles are usually extracted from large-scale simulations by GCMs (often, but not always, sharing the same physics as the LES model). Usually random (noise) perturbations of ~0.1 K amplitude are added to the initial temperature field so as to break the symmetry of this initial field and to help trigger convective motions. Although the most common kind of simulation encountered in the Martian literature is of "pure free convection," more realistic cases with nonzero background wind velocity have also been performed [e.g., *Tyler et al.*, 2008]. Thus far, Martian LES has been conducted with a uniform dust opacity (usually in clear conditions) and surface roughness.

5.3.3. First Results

[131] Martian LES has allowed a significant leap forward in our understanding of the BL dynamics on Mars and allowed the study of the fine-scale structure of the Martian daytime BL, dominated by convective processes (the "convective" BL): mixed-layer growth, polygonal cells, thermal updrafts, and convective vortices [*Rafkin et al.*, 2001; *Toigo et al.*, 2003; *Michaels and Rafkin*, 2004]. Work with three-dimensional LES models for Mars quickly followed the first experiments of two-dimensional LES by *Odaka et al.* [1998]; their simu-

lations predicted intense vertical winds (20 m s^{-1}) caused by the convection in the Martian BL, although two-dimensionality is thought to adversely affect the amplitude of the winds because of key aspects of vortex stretching not being permitted.

[132] The first successful attempt to perform 3-D LES was reported by *Rafkin et al.* [2001], who later published a paper entirely dedicated to the topic of Martian LES [*Michaels and Rafkin*, 2004]. Through simulations with horizontal resolutions of 150 and 30 m in situations of moderate background wind (5 m s^{-1}), the authors describe the structure of the convective BL on Mars. After sunrise, the convection is organized into horizontal linear structures that, between 08:00 and 08:30 LT under the influence of the horizontal shear, are rapidly turned into open polygonal cells, with narrow updrafts at the ridges of the cells and strong subsidence in the middle of each cell (see Figure 19). The horizontal structure of the vertical velocity 4 km above the surface (where only the top of the most intense updrafts remain) is in satisfactory agreement with the organization of convective clouds observed from orbit by the MGS Mars Observer Camera (compare Figures 19a and 19b). During the afternoon, until the BL convection collapses around 16:30–17:00 LT, as the convective BL deepens to reach its maximum altitude (~6 km in the simulations of *Michaels and Rafkin* [2004]) cells keep on widening while updrafts intensify, as is most likely dictated by the conservation of mass.

[133] The maximal value predicted for the vertical heat flux in the Mars LES by *Michaels and Rafkin* [2004] is ~1.5 K m s^{-1} and is reached just before noon. It is 1 order of magnitude larger than in terrestrial deserts [see also *Spiga*, 2011, and references therein]. In addition, contrary to the relative isotropy that is observed on Earth, the contribution of vertical motions to the turbulent kinetic energy seems more prominent than the contribution of the horizontal motions. As was noted in previous studies with single-column models [*Haberle et al.*, 1993b; *Savijärvi et al.*, 2004], convective motions act to cool the near-surface atmosphere ($z \leq 0.1 z_i$; see Figure 3) in situations of strong radiative heating (mostly absorption of infrared radiation incoming from the surface by the atmospheric CO_2) instead of warming it, as is the case on Earth. As boundary layer turbulent motions tend to mix heat to counteract the heating gradients, convection transports the radiative heat, plus the contribution of sensible heat flux as on Earth, higher up in the BL.

[134] During the afternoon, when the convection is at its most vigorous, LES shows numerous convective vortices of diameter 100–1000 m in the first hundred meters above the surface. However, only a small fraction of these vortices evolves into structures in cyclostrophic equilibrium comparable with the observed dust devils (which have a vertical extent of ~60% of the BL depth and a depression of ~2 Pa). *Toigo et al.* [2003] dedicated a paper to an in-depth analysis of these "dust devil–like" vortices by means of LES (see Figure 20 for an example of the structures obtained) that discusses some of these issues. The results of *Toigo et al.* [2003] for convective vortices complements those of *Michaels and Rafkin* [2004]. *Toigo et al.* [2003] noticed a great similarity
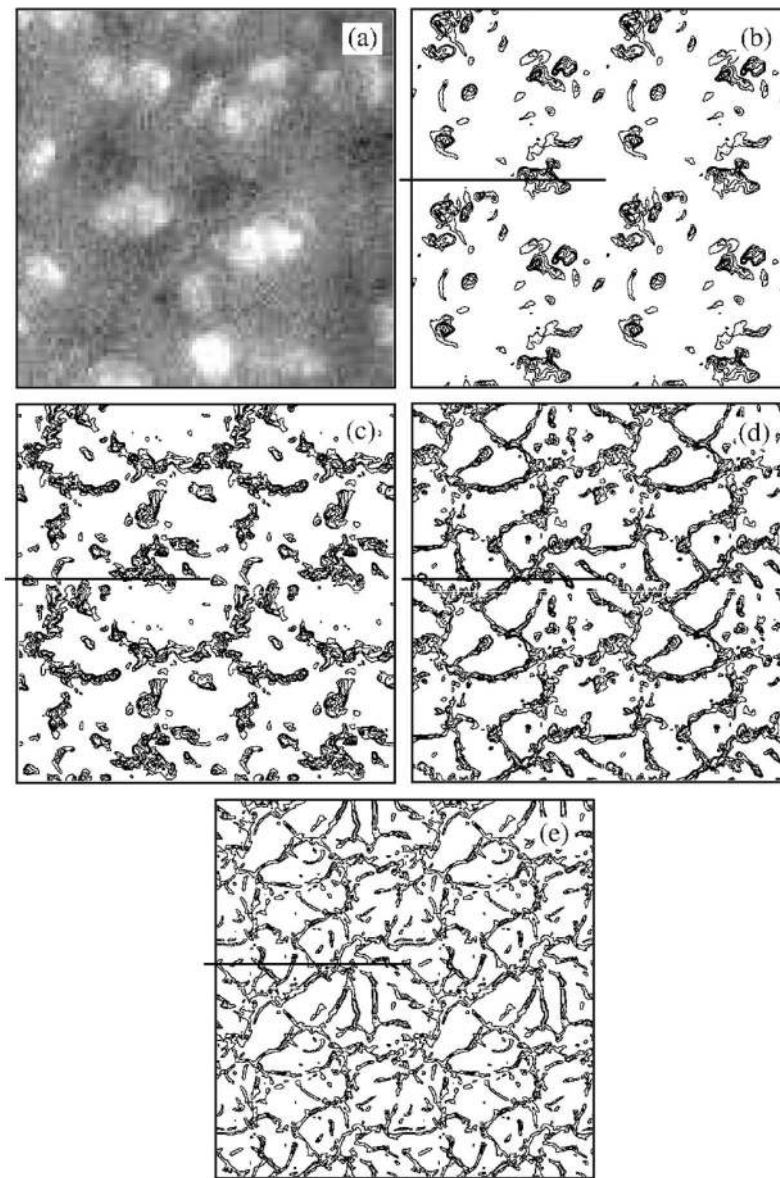
Figure 19. (a) An area (48 km × 48 km) of likely convective cloud over Syria Planum (portion of Mars Orbiter Camera image M0104901). Horizontal cross sections of vertical velocity at 1441 LST from the LES model of *Michaels and Rafkin* [2004] for heights of (b) 4342 m, (c) 2092 m, (d) 988 m, and (e) 385 m. Filled areas indicate regions of velocity greater than 2 m s^{-1}. Adapted from *Michaels and Rafkin* [2004] with permission.

with the equivalent terrestrial phenomena [*Kanak et al.*, 2000] and showed that the thermodynamic scaling theory of *Renno et al.* [1998] correctly describes the structure of the vortices. In addition, LES enables the assessment of the contribution of each term in the TKE equation. *Toigo et al.* [2003] showed that the vortices result from an equilibrium between production of TKE by buoyancy and a sink via advection of TKE and dissipation toward the smaller eddies. It is eventually confirmed by the study that convective vortices preferably form at the intersection of the convective cells. A plausible scenario to account for this is the twisting to the vertical of the horizontal vorticity resulting from temperature contrasts in the lowermost levels of the BL. The high sensitivity of the activity of the dust

devil–like vortices to the background wind is also emphasized by *Toigo et al.* [2003].

5.3.4. Recent Efforts and Perspectives

[135] Following the pioneering work described in the previous section, Martian LES studies with various models have confirmed the vigorous nature of the daytime Martian BL [*Richardson et al.*, 2007; *Sorbjan*, 2007; *Tyler et al.*, 2008; *Spiga et al.*, 2010]. These studies have shown that the daytime convective BL is significantly deeper on Mars than it is on Earth, with typical Martian BL depths exceeding extreme terrestrial values over desert regions (5 km), while maximum depths are over 10 km at around 11:00 LT. Over most Martian regions, the growing BL
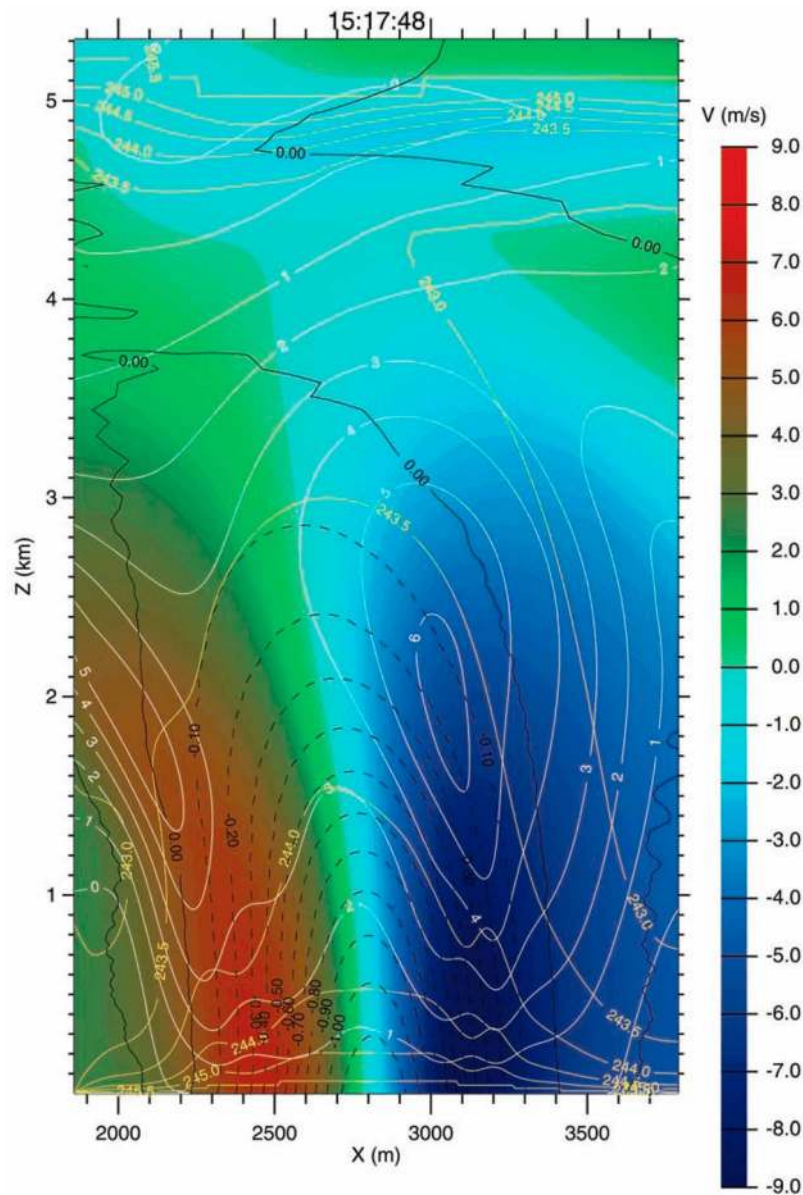
Figure 20. High-resolution simulation ($\Delta x = 10$ m) of the "no wind" simulation dust devil of *Toigo et al.* [2003]. Here a vertical slice through the center of the dust devil is plotted. Background color shows the tangential wind speed. Black contours show the pressure perturbation in Pa, reaching a maximum difference near the surface of about 1 Pa less than the background. Yellow contours show potential temperature in K and the warm core of the dust devil. White contours show upward wind velocity in m s^{-1}. Upward wind velocity peaks at the walls of the dust devil and the decrease in upward velocity can be seen in the center of the dust devil core. Adapted from *Toigo et al.* [2003] with permission.

already extends higher than the fully developed terrestrial BL over land in midlatitudes. Vertical eddy heat fluxes and TKE are of the order 1 K m s^{-1} and 10 m^2 s^{-2}, respectively, while updrafts could easily reach local values of 10 to 15 m s^{-1}. Note that these are not the most extreme values that might be encountered on Mars. As shown by *Spiga et al.* [2010], in a case where the boundary layer depth is nearly 9 km instead of 5 km, boundary layer potential temperature is ~50 K warmer, heat flux is more than doubled, and TKE is nearly tripled. By the end of the afternoon, the activity of convective plumes collapses, but BL motions are not entirely shut down [see, e.g., *Spiga and Forget*,

2009]. The stably stratified free atmosphere above the convective boundary layer is perturbed by the updrafts, which gives rise to internal gravity waves, by a mechanism similar to lee wave generation [*Stull*, 1976]. Because of the propagation of these gravity waves, the upper part of the boundary layer is still active after the early evening rapid collapse of the well-mixed layer below.

[136] Another consequence of intense boundary layer convection is the presence of convective vortices: *Michaels* [2006] shows through LES modeling, also taking into account dust lifting, that these structures would indeed account for the formation of dust devils and of subsequent

tracks along the ground of darker material, where bright dust is removed by vortices.

[137] Strong turbulent motions in the Martian BL might cause atmospheric hazards for future Martian landers. In the context of the paucity of turbulent wind measurements in the Martian BL, LES models are interesting and useful tools to address such questions. So far as preparations for missions to Mars are concerned, LES has been employed to estimate the atmospheric hazards for entry, descent, and landing at the selected sites of the Mars Exploration Rovers [*Toigo and Richardson*, 2003; *Rafkin and Michaels*, 2003; *Kass et al.*, 2003], Beagle 2 [*Rafkin et al.*, 2004] and Phoenix [*Tyler et al.*, 2008; *Michaels and Rafkin*, 2008]. *Rafkin and Michaels* [2003] noted that over Isidis Planitia, where upslope circulations can be encountered, convective updrafts are linearly organized in the horizontal. Furthermore, a return flow layer with moderate subsidence above the upslope circulation suppresses the growth of the afternoon convective BL, which appears only half as deep as over similar plains devoid of this regional circulation feature. This effect is also described by *Toigo and Richardson* [2003] within Gusev Crater. *Tyler et al.* [2008] showed through LES modeling in high-latitude regions (Phoenix landing site) that the influence of background wind on the simulated BL depth is not negligible but is far less crucial than variations of surface thermophysical properties (namely, albedo and thermal inertia). As also discussed by *Michaels and Rafkin* [2008], afternoon BL convection is vigorous, even in those high-latitude regions where surface temperatures are low. Amongst other consequences, this could constitute a significant atmospheric hazard for spacecraft descent and landing. The need for accurate and realistic Martian microscale modeling remains critical for the design of upcoming missions to Mars (e.g., Mars Science Laboratory, ExoMars).

[138] To date, LES studies have mostly centered on idealized numerical experiments, which have produced plausible results with respect to the limited observations available. The quantitative validation of LES diagnostics against existing data remains to be done, however. One of the main limiting factors is the paucity of data covering the entire vertical extent of the Martian BL. This limitation was recently addressed with the Mars Express radio occultation experiment [*Hinson et al.*, 2008]. Temperature profiles were obtained with good vertical resolution and coverage at latitudes and local times where BL convection is occurring, permitting an unprecedented estimation of convective BL depth. In low latitudes, the Martian convective boundary layer appeared to extend to higher altitudes over high plateaus than in lower-altitude plains, despite similar surface temperatures. Surface altimetry strongly influences the regional variability of daytime BL growth when considering locations at constant latitude and local time. *Spiga et al.* [2010] shows that these dramatic regional variations of convective BL depth are qualitatively and quantitatively predicted by LES (see Figure 21) in spite of their idealized character. High-resolution numerical modeling complements the radio science observations acquired over a con-

siderably larger area than the width of typical convective cells. LES reveals the BL dynamics associated with the observed regional differences in BL depth. Intense BL dynamics is found to underlie the measured depths (up to 9 km), with vertical wind speeds up to 20 m s^{-1}, turbulent heat fluxes up to 2.7 K m s^{-1}, and convective turbulent kinetic energies up to ~26 m^{-2} s^{-2}.

[139] Through large eddy simulations, it is also possible to relate the regional variability of BL depth [*Hinson et al.*, 2008] (see section 4) to the aforementioned dominant radiative forcings of the Martian boundary layer [*Spiga et al.*, 2010] (see sections 3 and 5). Mars appears in striking contrast to terrestrial arid conditions where sensible heat flux dominates [*Spiga*, 2011]. On Earth, the afternoon boundary layer generally warms "from below" by sensible heat flux upwelling from the heated surface, whereas on Mars it warms "both from inside and from below" by infrared radiative heating (plus visible absorption by dust) and sensible heat flux, respectively. New scaling mixed-layer laws in quasi-steady midday conditions will need to be developed for the Martian case to account for the turbulent heat flux not being at its maximum near the surface but at a few hundreds of meters above it. Mars confirms that the boundary layer has to be defined as that part of the atmosphere influenced by the presence of the surface, and not only by the surface itself. In the Martian environment, the energy that fuels the thermals of typical mean velocity w_* does not originate only from the atmospheric levels immediately adjacent to the surface. Thus, a version of the mixed layer formulae valid both on Mars and on Earth should substitute the maximum heat flux $\langle w'\theta' \rangle_{max}$ for the surface heat flux $\langle w'\theta' \rangle_0$ [*Spiga et al.*, 2010; see also *Sorbjan*, 2007]. For instance, only the relationship

$$W_* = \left[g z_i \frac{\langle w'\theta' \rangle_{max}}{\langle \Theta \rangle} \right]^{1/3} \tag{62}$$

(where z_i is the boundary layer depth and Θ is the potential temperature) enables one to calculate the Martian vertical velocity scale W_* consistent with resolved convective motions computed by LES. Values of $W_* = 4$ to 6.5 m s^{-1} obtained for Mars account for the vigorous convection compared to Earth (where $W_* < 2$ m s^{-1}) and are in good agreement with similarity estimates based on observations [*Martínez et al.*, 2009]. Moreover, scaling by maximum heat flux instead of surface heat flux allows for a rigorous comparison between Martian and terrestrial convective boundary layers as shown in Figure 3.

[140] Future work in this arena will focus upon the influence of variations of dust opacity, background wind, local topography, and synoptic and mesoscale vertical motions so as to yield more realistic LES results. Although elements of comparison between Mars and the Earth can already be put into a useful perspective, the Martian small-scale variability remains to be explored in greater detail, especially with additional measurements of wind and temperature, in order to validate diagnostics derived from numerical models and to expand the knowledge of small-scale
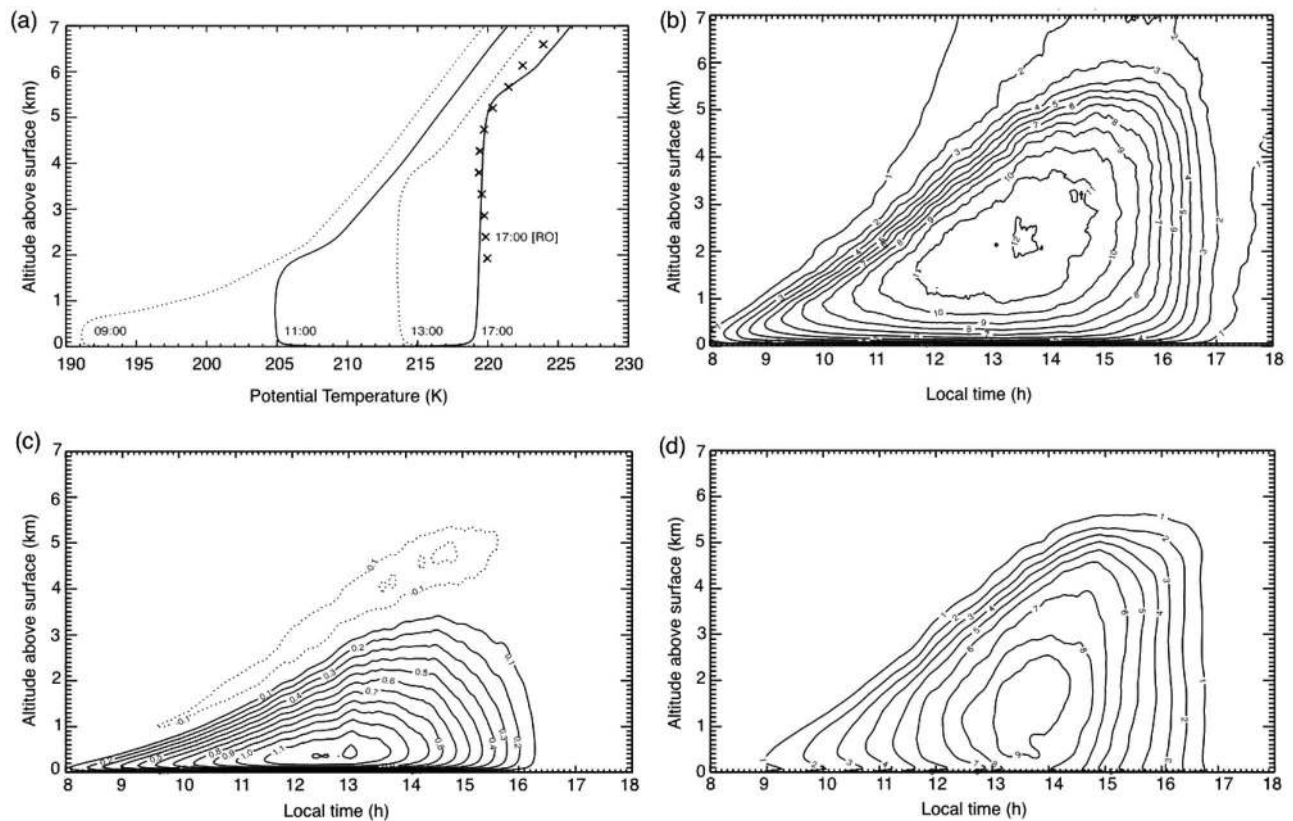
Figure 21. Variation of the LES statistics with time and height above ground in case study b (Amazonis Planitia) of *Spiga et al.* [2010]: (a) potential temperature (K) with superimposed radio occultation profile at 17:00 LT, (b) updraught maximum vertical velocity (m s^{-1}), (c) vertical eddy heat flux (K m s^{-1}), and (d) turbulent kinetic energy (m^2 s^{-2}). All displayed quantities are averaged over the simulation domain. Adapted from *Spiga et al.* [2010] with permission.

phenomena by new studies in extreme environments. To date and to the extent of our knowledge, nighttime Martian LES results have not been much discussed in the literature and remain a topic to be explored.

6. ROLE OF THE MARTIAN PBL IN THE GLOBAL CLIMATIC SYSTEM

[141] The Martian planetary boundary layer plays a crucial role in communicating fluxes of heat, momentum, dust, moisture, and chemical species between the solid surface of Mars and the global-scale atmospheric circulation. These fluxes not only inject aerosols and constituents into the atmosphere above the boundary layer, but they can modify the global atmospheric circulation, either through radiative effects leading to local heating or cooling, such as from absorption by aerosols, or by exchanging momentum and heat between the surface and atmosphere. These last two effects provide a drag on the large-scale flow, by mixing in air with zero mean momentum, and a direct thermal forcing, by mixing heat from the surface. The latter rapidly responds to changes in insolation when the atmosphere is clear, transferring heat into the middle atmosphere much more rapidly than would be achieved by conduction alone.

[142] The deep convective boundary layer on Mars, extending occasionally to over 10 km altitude above the

surface during the daytime [*Hinson et al.*, 2008], can efficiently mix quantities such as heat, momentum, dust, moisture, etc., from those parts of the atmosphere in close contact with the surface rapidly to great heights, at which point they will be taken up by the global circulation and distributed around the planet on a timescale of a day or two. The PBL on Earth plays a similar role, but it is relatively less important for global transport not only because it typically does not extend so high into the atmosphere, but because deeper convective motions that extend beyond the boundary layer are strongly driven by latent heat release as water condenses. On Mars, the latent heat effects of water are essentially negligible, but the ability of dust and water ice to absorb solar radiation, and so locally to heat the atmosphere, can be thought of as a somewhat analogous effect. This takes place on longer time scales, however, than those on which latent heat can drive convective cumulus clouds to the top of the terrestrial troposphere (~20–40 min, assuming a typical updraft wind speed of ~10 m s^{-1} [e.g., see *Emanuel*, 1994]).

[143] It has been demonstrated [*Newman et al.*, 2002a] that boundary layer mixing is essential to lift dust into the body of the atmosphere. If dust is lifted by near-surface wind stress, derived from the large-scale winds, but only injected into the lowest level in a model (5 m above the

surface, in the case of *Newman et al.* [2002a]), then the dust can remain trapped close to the surface and is consequently not transported over large horizontal scales by the model winds. This is particularly true if the dust, or other tracer, in the model is not radiatively active. It was found to be vital to mix any tracer injected into the lowest level of the atmosphere in the vertical over a few levels, with the mixing being governed by the convective and turbulent fluxes implied by the parameterized PBL. Feedback from radiative heating can enable the dust to enter the planetary-scale meridional and zonal circulation much more easily by enhancing the local vertical velocity and leads to dust raised in one hemisphere being transported to the other within days as it enters the powerful cross-equatorial Hadley circulation.

[144] Dust devils are one of the most obvious manifestations of boundary layer activity, primarily during summer afternoons, when the atmosphere is relatively clear and the surface is warm. Dust devils are regularly seen on Earth, particularly in desert regions during the summer, but they are even more spectacular on Mars, can reach over 12 km in height, and can be readily seen from orbit [*Malin and Edgett*, 2001]. Dust devils play an important role in lifting dust from the surface on Mars, and perhaps contribute the largest component of the background dust level during the relatively clear Martian northern hemisphere summer season. Once the amount of dust in the atmosphere becomes larger, the atmosphere becomes relatively warmer and the surface becomes cooler, so reducing the temperature contrast, the intensity of convection, and the height and strength of the convective boundary layer. This negative feedback means that dust devils are unlikely to be responsible for planet encircling dust storms on Mars but will instead tend to be inhibited as more dust is lifted [*Newman et al.*, 2002b].

6.1. Relationship Between the PBL and the Surface

[145] Orbiters and landers have shown that dust devils and dust storms are ubiquitous on Mars [e.g., *Greeley and Iversen*, 1985; *Renno et al.*, 2000; *Cantor et al.*, 2001]. Together with convective plumes and turbulence forced by wind shear, these weather phenomena transport dust, water vapor, and other tracer species upward. Dust is lifted when the wind speed exceeds a threshold value, and sand particles propelled by drag forces bounce along the surface, ejecting the smaller, harder to lift dust aerosols into the air, in a process known as saltation [*Bagnold*, 1941]. Besides ejecting dust into the air, saltation plays an important role in geological processes such as sediment transport, the formation of sand dunes, and wind erosion [*Greeley and Iversen*, 1985].

[146] Once lifted, dust aerosols may be transported over large horizontal distances by the wind, so that the distributions of suspended dust do not necessarily correlate with the sources of lifting in a simple manner. Moreover, the various dust lifting processes may interact with the surface in different ways, leading to different geographical locations for the various dust sources. Dust aerosols play an important role in climate by scattering and absorbing solar radiation and by absorbing and emitting thermal radiation. In addition, dust particles serve as sites for heterogeneous chemical reactions that might be either sources or sinks of trace gases. Both chemical and dynamical effects may also arise from electrostatic charges that can develop within wind-driven sand or dust [*Melnik and Parrot*, 1998; *Kok and Renno*, 2008, 2009]. From an engineering point of view, variations in atmospheric dust content affect spacecraft performance by producing variations in the flux of solar radiation at the surface and variations in atmospheric temperature and density. For example, the Mars Global Surveyor detected orbit-to-orbit variations by factors of two in atmospheric density at about 120 km, probably caused by variations in atmospheric dust content and temperature [*Bougher et al.*, 1999]. Thus a better characterization of the dust cycle is important to the understanding of some of the most important processes actively modifying the Martian surface and producing short-term atmospheric variability that affects aerobraking, aerocapture, entry, descent, and landing.

[147] Dust devils form at the bottom of convective plumes. Since their sources of angular momentum are local wind shears, caused either by the convective circulation itself or by larger-scale phenomena, they can rotate clockwise or anticlockwise with equal probability [*Renno et al.*, 1998]. A distinctive feature of intense dust devils is their well-defined dust funnel. Theory indicates that dust is focused around the funnel by a dynamic pressure drop caused by increases in the speeds of the air spiraling toward the vortex [*Renno*, 2008]. Like waterspouts, tornadoes, and hurricanes, dust devils can be idealized as convective heat engines. They are the smallest and weakest members of this class of weather phenomena [*Renno*, 2008]. They form when a vortex strong enough to initiate saltation occurs over surfaces composed of loose particles. The intensity of a dust devil depends on the depth of the convective plume and the transfer of heat from the ground into the air [*Renno et al.*, 1998].

[148] On Mars, dust devils are much bigger and stronger than on Earth. Terrestrial dust devils have typical diameters of less than 10 m and are seldom higher than 500 m [*Sinclair*, 1973]. In contrast, dust devils with diameters between 100 m and 1 km and heights in excess of 5 km are observed on Mars [*Thomas and Gierasch*, 1985; *Malin et al.*, 1999]. The dust devils observed in the Pathfinder images have about 700 times the dust content of the local background atmosphere [*Metzger et al.*, 1999]. Measurements by *Renno et al.* [2004] indicate that the heat and dust fluxes in terrestrial convective plumes and dust devils can be many orders of magnitude larger than their background values of a few 100 W m^{-2} and a few 100 μg m^{-2} s^{-1}. Calculations suggest that dust devils are a significant source of atmospheric dust both on Earth and on Mars [*Renno et al.*, 2004]. There is evidence that, besides dust storms, dust devils play an important role in the Martian dust cycle. For example, the atmospheric dust opacity increased throughout the MPF mission in spite of low-wind conditions and the absence of dust storms on the planet. *Ferri et al.* [2003] showed that the dust flux due to dust devils contribute significantly to the maintenance of dust in the atmosphere of Mars, perhaps even being the primary source of dust into

the atmosphere of the MPF landing site at the Ares Vallis region. They might also play an important role on the transport of other tracer species.

[149] On Earth, windblown sand, dust devils, and dust storms produce electric fields ranging from a few 100 V m^{-1} to 200 kV m^{-1} [*Crozier*, 1964; *Stow*, 1969; *Schmidt et al.*, 1998; *Renno and Kok*, 2008]. Even small terrestrial dust devils can produce electric fields of the order of 10 kV m^{-1} [*Renno et al.*, 2004], which is of the order of that necessary to produce electric discharges in the thin Martian atmosphere [*Melnik and Parrot*, 1998]. Charge transfer during collisions of sand with dust particles [*Renno et al.*, 2003], and charge separation by updrafts and turbulent diffusion, produce these large fields [*Kok and Renno*, 2008]. Numerical simulations by *Melnik and Parrot* [1998] predict the occurrence of electric discharges in Martian dust storms. *Ruf et al.* [2009] showed evidence of that deep Martian dust storms can produce powerful electric discharges.

[150] Recent studies suggest that electric fields in Martian dust storms produce energetic electrons [*Delory et al.*, 2006], destroy water vapor, and lead to the formation of hydrogen peroxide, a potential sink of methane [*Atreya et al.*, 2006; *Kok and Renno*, 2009]. Hydrogen peroxide could be responsible for the reactive soil found at the Viking landing sites [*Oyama et al.*, 1977]. Moreover, energetic electrons are predicted to directly dissociate methane [*Farrell et al.*, 2006]. The large spatial and temporal variability of the methane observed in the Martian atmosphere suggests the existence of as yet unknown strong sources and sinks of this gas [*Lefevre and Forget*, 2009]. Dust electrification and heterogeneous reactions on dust particles might explain this puzzling result.

[151] In situ measurements in the PBL can shed light on the processes described above and lead to a better understanding atmospheric and geological processes. Moreover, they can lead to a better understanding of the habitability of Mars.

6.2. The Influence of the PBL on Martian Weather and Climate

[152] The planetary boundary layer has a profound effect upon the Martian atmosphere on weather and climate time scales and spatial scales, and its influence is particularly strong on a planet with a mostly clear and thin atmosphere, where changes in surface temperature and surface drag have a huge impact compared to the relatively smaller thermal and dynamical inertia of the atmosphere itself. This is illustrated by the small changes in surface temperature with elevation on Mars; temperature contours tend to follow the surface much more so than they do on Earth [*Webster*, 1977; *Nayvelt et al.*, 1997]. This results in a global-scale thermal forcing to the lower atmosphere on Mars, communicated from the surface by conduction over only very short distances and then, much more strongly, by convection within the planetary boundary layer.

[153] The planetary boundary layer also provides a large-scale friction on the global circulation, by mixing air that has been in direct contact with the surface and has essentially

zero momentum over a range of heights up to at least 10 km. This results in an effective drag to the large-scale winds. Large-scale stationary waves are generated on Mars, linked to the surface topography. *Nayvelt et al.* [1997] have shown that the near-surface winds associated with stationary waves are sensitive to the parameterized frictional effects of the boundary layer and a careful choice of parameters is necessary to get good agreement with observed streak directions. Small-scale inertia-gravity waves are also readily generated near the surface on Mars, largely through winds blowing over topography but also from convective and frontal wedge-type forcing in the boundary layer. These waves can have a strong effect on the upper atmospheric winds, where the vertically propagating waves break, typically tending to drag the large-scale winds toward zero [*Joshi et al.*, 1996].

[154] A final intriguing possibility in the lower atmosphere is that the varying thickness of the planetary boundary layer, which tends to be deeper over higher topography [*Hinson et al.*, 2008], may itself cause topographic effects (low-level drag over different depths of the atmosphere and generation of stationary waves) that are exaggerated compared to the already large, actual size of the Martian surface topography (see also the explanation offered for this by *Souza et al.* [2000]).

[155] The role of the planetary boundary layer in injecting and then mixing dust into the Martian atmosphere has already been noted. It should also be noted that the atmosphere will feedback on the planetary boundary layer under very dusty conditions, reducing convection and turbulence. Thus the boundary layer might itself be seen as a vital component of the Martian dust cycle which can exhibit both positive (at low dust levels) and negative (at high dust levels) feedbacks on the dust cycle and the amount of dust loading in the Martian atmosphere. The dust loading is itself a dominant component of Martian climate and a both a driver and symptom of climate variability.

6.3. The PBL in Spacecraft Mission Planning

[156] The dominant role of the planetary boundary layer over the whole of the lowest scale height of the Martian atmosphere and above has been discussed. A good representation of the boundary layer is clearly vital to a successful model of Martian weather and climate. It is also important for spacecraft mission planning, for both weather predictions for landed operations and for entry, descent, and landing itself. In particular, vertical wind speeds associated with turbulence in the convective boundary layer can vastly outstrip the large-scale vertical flow. This might be a major consideration for landing heavier payloads with a parachute or small retro thrusters, for example. The degree of turbulence and the time of day when it can be expected to be large are also major factors in limiting the uncertainty of the landing ellipse of a spacecraft. Even if landing at night, strong katabatic winds can form in the stable atmosphere and low-level density flows may upset landing calculations.

[157] Progressively sophisticated and increasingly high-resolution modeling has been applied to assist mission

design and planning. More recent such efforts in support of, e.g., the MER and Phoenix missions have been reported for instance by *Toigo and Richardson* [2003], *Rafkin and Michaels* [2003], and *Tyler et al.* [2008].

7. CONCLUSIONS AND OUTLOOK

7.1. Discussion and Outstanding Issues

[158] We see from both models and observations available from in situ and remote sensing measurements that a great deal of information on the Martian PBL can be gleaned from simple adaptations of our extensive knowledge of the PBL on Earth. Monin-Obukhov similarity theory appears to work quite well for characterizing the surface layer on Mars, provided one takes into account some important differences, e.g., in molecular viscosities and diffusivities of Martian air. The latter implies, amongst other things, a larger Kolmogorov dissipation scale, resulting in a somewhat narrower inertial range within which turbulent motions can evolve before being damped out at small scales. But nevertheless there is enough room for a significant inertial range to develop, allowing for the exchange of energy, momentum, and tracers in a manner consistent with the basic underlying assumptions of the Monin-Obukhov theory.

[159] In the main body of the boundary layer in the transition zone between the PBL and the free atmosphere, it is customary to assume (e.g., in boundary layer parameterizations in global and mesoscale models) that Mars will exhibit flow regimes that are directly equivalent to those encountered on Earth, depending upon whether the basic stratification is stable, neutral or unstable. The limited range of observations available over this height range (10 m– 10 km) seem to be consistent with these assumptions, although it is clear that conditions on Mars lead to more extreme forms of convective or ultrastable stratification than on Earth. The recent development of numerical LES models has enabled at least some aspects of this problem to be investigated by direct simulation (see section 5.3), at least under somewhat idealized circumstances. Such investigations have shown that strongly superadiabatic conditions are likely to be common near the Martian surface during the daytime and are more extreme than encountered even over high-altitude subtropical deserts on the Earth. It is important, therefore, to take this into account when parameterizing low-level convection on Mars in global circulation models using simple convective adjustment schemes. Such schemes may need to be flux limited in order to provide adequate estimates of the resulting stratification close to the surface. Another important issue, also highlighted in recent LES simulations for Mars, is the likely increased role of direct radiative fluxes within the PBL. Such fluxes are generally assumed to be negligible on Earth but are almost certainly far from negligible under conditions typically prevailing on Mars, especially during the day. This is currently neglected in most approaches to PBL parameterization in global and mesoscale models but should receive more attention in future work.

[160] The parameterization of strongly stable conditions in such models has proved notoriously problematic for both planets for many years. This is mainly because of the common assumption that shear-induced turbulence is fully suppressed if the gradient Richardson number exceeds a value Ri_{cr} of 0.2–0.5. Observational studies on Earth, however, consistently show that, even when Ri_g is much greater than unity, some degree of "turbulent" mixing persists. LES simulations seem to confirm this, with mixing and transport apparently due (at least in part) to the action of gravity waves when the static stability is strong. In this regard, the QNSE approach reviewed in section 5.2 offers a promising approach toward the adaptation of, or even as an alternative to, the conventional Mellor-Yamada family of parameterizations.

[161] Other important characteristics of strongly stratified flows are the vertical spectra of the horizontal kinetic energy and potential energy. On Earth, the former obeys the universal scaling law, $E_1(k_z) = cN^2 k_z^{-3}$, $c \simeq 0.2$. *VanZandt* [1982] noticed that the observed vertical spectra of the horizontal velocity in the atmosphere have a tendency to develop a universal distribution for all seasons, meteorological conditions, and geographical locations throughout the atmosphere. This distribution has been referred to as a canonical gravity wave spectrum [*Fritts and Alexander*, 2003] as its origin has often been attributed to interacting internal gravity waves [see, e.g., *Dewan*, 1979; *Dewan and Good*, 1986; *Fritts and Alexander*, 2003, and references therein]. *Galperin and Sukoriansky* [2010] discussed the connection between this spectrum in the free atmosphere and in the boundary layers. The vertical spectrum of the potential energy is more difficult to measure but generally it appears to be proportional to $E_1(k_z)$ [see, e.g., *Cot*, 2001]. These spectra are not only important atmospheric characteristics but are also critical for understanding of the physics of stably stratified turbulence. It is important that these spectra be measured in the Martian atmosphere in future missions.

[162] In discussing these and other related issues (such as concerning transports of water vapor, dust, and chemical tracers within the PBL), it is important (and sobering) to keep in mind the relative sparseness of direct observational measurements within the Martian boundary layer, compared with the rich set of measurements available to validate models and parameterization schemes on Earth. The vast majority of in situ measurements on Mars have been obtained from just a few (six, including the MER rover and Phoenix lander) spacecraft, at best equipped with meteorological sensors mounted at three vertical levels on measurement booms little longer than 1 m. While these kinds of measurement arrays can (in principle) provide direct measurements of vertical structure, heat and momentum fluxes, and spectra within the surface layer, they leave the rest of the mixed layer and transition zone (forming the bulk of the PBL) virtually unobserved. Even within the set of six successful surface landers, only four were so equipped with proper meteorological instrumentation, and of those, only two (the Viking landers) had wind sensors that could accurately measure wind velocities sufficiently to measure covariances and momentum fluxes. Practical mission safety requirements have so far limited all available landers to relatively low lying, flat, and featureless landing sites. While

such landscapes may be typical for large tracts of the Martian surface, there are huge areas of mountainous uplands on Mars where we have essentially no in situ measurements with which to validate model predictions. Such observational information as exists comes almost entirely from remote sensing instruments in orbit around Mars, which have many limitations in terms of spatial and temporal resolution and coverage. These types of observation, together with just a very few descent profiles measured during the entry, descent, and landing of the extant successful landed spacecraft, also currently constitute our sole sources of direct information on the structure and behavior of the mixed layer and transition zone.

[163] To put this into a terrestrial perspective, such detailed in situ coverage is tantamount to attempting to characterize the boundary layer structure of the entire Earth, based on measurements at, say, just 3 to 4 locations in the (nonmountainous parts of the) Sahara Desert and one in northern Canada or Antarctica. Such coverage would be scarcely representative even of the full range of desert landscapes on Earth (or even the Sahara and Sahel region itself). Moreover, only a few of those stations have measured for long enough even to span the entire seasonal cycle over one or a few years. It is hard to imagine how crude our state of knowledge of the Earth's PBL would be, were we to have been limited to this level of coverage.

[164] Given the profound importance of the PBL for both spacecraft operations and scientific modeling of the present and past Martian atmosphere and climate and the likely strong variability in PBL structure and properties depending on location, season, and time of day, there remains a very clear and compelling need to obtain many more measurements in this critical region of the Martian atmosphere. Even the existing in situ measurements have some severe limitations, with relatively few direct measurements of key fluxes of heat and momentum even at the best observed locations. Future instrumental campaigns will need to focus not only on widening the geographical and temporal coverage of measurements in the PBL but also on obtaining (1) in situ measurements with higher temporal resolution (with a sampling frequency in the 1–10 Hz range) in order to enable full characterization of turbulent heat and momentum fluxes, together with full kinetic energy and temperature spectra, (2) simultaneous measurements of turbulent and radiative fluxes close to the surface, and (3) profiled measurements of the main boundary layer and transition zone, including (ideally) determination of turbulent and radiative fluxes over the lowest 2–5 km of the atmosphere. Such measurements need to allow for strong temporal variations anticipated in this region of the atmosphere on diurnal, synoptic (2–20 sols), seasonal, and interannual timescales at each location in order to characterize fully the complete range of boundary layer processes. Aspirations (1) and (2) are relatively modest in their instrumental requirements, needing relatively simple upgrades to the kind of instrumentation that has already been successfully operated on Mars. For (3), however, a more sophisticated and complex campaign may

be necessary, perhaps using a mixture of airborne in situ and remote sensing instrumentation.

[165] Such considerations have not tended to command the priority for future spacecraft missions to Mars that one might have expected, given the issues raised above. Moreover, since the Viking, Pathfinder, and Phoenix landers have already made extensive atmospheric measurements, the notion continues to persist in some quarters that further measurements of this kind have relatively little value. But we know from our experience on Earth that a single station observing for 1 year would be quite insufficient to characterize fully the most important boundary layer processes even for a continent, let alone an entire planet. Given (1) the critical importance of wind shear and turbulence, dust, and radiation, etc., from an operational safety perspective, even of exobiologically or geologically focused lander missions, and (2) the relatively modest cost and resource requirements of the pertinent basic environmental measurements (atmospheric pressure, temperature, and wind), the omission of these relevant measurements on board all future Mars landers is difficult to justify. It is at least somewhat reassuring, therefore, that a basic complement of surface meteorology instrumentation is being considered for many of the currently planned or proposed missions in the near future. We now go on to review these missions in the light of the above discussion.

7.2. Observations on Confirmed Future Missions

[166] The next major landed Mars mission (scheduled for launch in 2011) is the Mars Science Laboratory (MSL), also known as Curiosity (see section 7.2.1). Other confirmed missions include the Phobos-Grunt (scheduled also for launch in 2011), the Mars Atmospheric and Volatile Evolution (MAVEN; launch in 2013–2014) and the Trace Gas Mission (TGM; slated to carry a small lander, for launch in 2016). Of these missions, the MSL is especially expected to be of particular relevance for PBL studies.

7.2.1. Mars Science Laboratory

[167] MSL's payload includes a comprehensive environmental instrument package, the Rover Environmental Monitoring Station (REMS [*Gómez-Elvira and the REMS Team*, 2008]). The REMS observations most relevant to PBL studies are wind speed and direction ($\vec{V}$), pressure (p), relative humidity (U), air temperature (T_{air}) and surface temperature (T_s). The pressure sensors are located inside the rover. The other sensors are placed at approximately 1.5 m above the ground, attached to two horizontal booms attached in turn to the rover's vertical Remote Sensing Mast (RSM).

[168] The requirement is to determine horizontal wind speed with ±1 m s^{-1} accuracy in the 0–70 m s^{-1} range, with a resolution of 0.5 m s^{-1}. The directional accuracy is expected to be better than 30°. For vertical wind the range is 0–10 m s^{-1}, with an accuracy and resolution as for the horizontal wind. T_{air} is measured by resistive sensors placed at the tips of rods bringing the sensors outside of the support structure's thermal influence. The range is 150–300 K, accuracy is 5 K, and resolution is 0.1 K. Pressure measurement range is 1–1150 Pa, end-of-life accuracy is 20 Pa,

and resolution is 0.5 Pa. Humidity will be measured by a single sensor (on one of the two booms) with 10% accuracy in the 200–323 K range with 1% resolution. Surface (brightness) temperature is sensed remotely from three thermopiles viewing the surface on one of the horizontal booms. The required range is 150–373 K with ±10 K accuracy and 2 K resolution.

[169] As mentioned previously, the wind field at the booms will be perturbed by the RSM and by the rover itself. The RTGs may also influence the wind and temperature observations. Calibration will be done via a variety of wind tunnel tests under Mars conditions as well as numerical modeling. Simulations will be used to obtain results where tests conditions cannot be reproduced on Earth. Observations on PBL turbulence, heat fluxes, and the characteristics of dust devils are among main science objectives of the REMS.

[170] The REMS operations baseline has been designed to be straightforward and regular: 5 min of data will be taken for every hour throughout every sol (irrespective of whether the rover itself is awake or not) from all sensors at 1 Hz sampling frequency. Additional observations can be scheduled, as long as the total diurnal REMS observation duration remains below 3 h. Examples include longer (up to 1 h) contiguous blocks. Mobility may allow for sampling of different microscale environments and provide "horizontal profile" measurements. Here the regular observation pattern will aid in separation of time and location dependencies.

7.2.2. Meteorological Network Precursor

[171] The Meteorological Network (MetNet) is a joint Finnish, Russian, and Spanish Mars mission concept based on a new type of semihard landing vehicle called the MetNet lander (Mars Network lander (MNL); http://www.meiga-metnet.org [*Harri et al.*, 2010; A.-M. Harri et al., Mars meteorological landers for meteonetworks and other applications, submitted to Acta Astronomica, 2010; A.-M Harri, private communication, 2010]). The new design aims at creating a small and relatively low cost lander by improving the payload-to-total-mass ratio by use of inflatable structures in the entry, descent, and landing system. Those characteristics are enabling factors in meeting the goal of the MetNet Mission: deployment of several tens of landers onto the Martian surface as a way of establishing a surface network comprising up to a few tens of landers with emphasis on atmospheric observations (see also section 7.3). Small size, moderate cost, and large numbers might also enable choices of more interesting (and quite possibly also riskier) landing sites (such as canyons) and comparisons between them of PBL characteristics and phenomena.

[172] The MNL precursor mission is scheduled for launch in the 2011–2012 window, carried to Mars by the Russian Phobos-Grunt spacecraft (e.g., http://en.wikipedia.org/wiki/Phobos-Grunt). The tentative payload (see, e.g., http://metnet.fmi.fi/fileadmin/templates/main/img/gallery-posters/pdf/MetPayload_EPSC09_Final.pdf) includes six instruments relevant to PBL studies: temperature, pressure, humidity, solar irradiance, and dust sensors as well as a panoramic camera (Table 3). Temperature will be measured with thermocouples at three levels, and pressure and humidity will be measured

with capacitive sensors of Phoenix and MSL heritage. Dust observations will be provided by both the solar irradiance and the dedicated dust sensors. The MetNet Precursor is a technology demonstration mission, hence the lifetime on the surface will be short: the primary mission is approximately a month, and a possible secondary mission phase is at most a few months.

7.3. Observations on Planned Future Missions

7.3.1. Mission Opportunities

[173] ESA and NASA have agreed to merge and consolidate their respective Mars exploration programs into a framework called Mars Exploration Joint Initiative (ESA-NASA joint Mars program: http://www.esa.int/esaSC/SEMH1J6CTWF_index_0.html). The program has at the time of writing been outlined for the 2016 and 2018 launch windows (see http://sci.esa.int/science-e/www/object/index.cfm?fobjectid=46048) but is expected to continue beyond those windows.

[174] The TGM orbiter (section 7.2) slated for the 2016 launch window includes an entry, descent, and landing demonstrator module, which may carry some science (possibly also atmospheric) instrumentation to the surface for short-duration (approximately a week) operations (see http://sci.esa.int/science-e/www/object/index.cfm?fobjectid=46124). The 2018 launch window is allocated for a dual rover payload, with emphasis on exobiology.

[175] A surface network is a possibility for the 2020 launch window. It would be scientifically the next logical step in the field of atmospheric studies. Several network proposals have been made in the last 15–20 years, yet none has proceeded to launch [see, e.g., *Chicarro et al.*, 1993; *Banerdt et al.*, 1996; *Harri et al.*, 1999; Ames Research Center, Mars Environmental Survey (MESUR) science objectives and mission description, unpublished report, 124 pp., NASA, Moffett Field, California, 1991; Pascal: A Mars climate network mission, Pascal mission proposal Web site, accessed 1 June 1999, http://www-mgcm.arc.nasa.gov/mgcm/micromet/pascal.html].

[176] An initial surface network can be expected to have a primarily global and regional (and possibly mission landing and operations assurance) emphasis, but from the PBL study perspective, an adequately instrumented network would permit a significant improvement in the sampling of different environments for surface-atmosphere interactions and the dependence of PBL phenomena and characteristics thereon.

7.3.2. Example Surface Instrument Suite

[177] An example instrument suite that would provide a lander- or rover-based comprehensive set of measurements of PBL behavior is described in this section. It is intended as an example that incorporates many of the suggestions for measurements mentioned in this review.

[178] One possible recommendation for a desirable and scientifically comprehensive instrument suite would include four sensor systems: a sonic anemometer, a tunable laser spectrometer, a visible and IR radiometer, and a pressure sensor. With these sensors, measurements of water vapor (and possibly other trace gases such as methane) abundances

and fluxes, air temperatures (from the surface up to several km), ground surface and regolith temperatures, surface radiative fluxes, sensible heat fluxes, and surface pressure could be made.

[179] Measurements should be simultaneously and regularly taken throughout the diurnal cycle, including the unstable (convectively active) daytime and the stable (but mechanically active) nighttime. The above mentioned quantities should be measured at a rate of $\simeq$1–10 Hz to measure the turbulent variability adequately.

[180] Observations of the ground surface and regolith temperatures can be thought of as representing measurements of the thermal forcing of the PBL and could be made by an IR radiometer (at multiple wavelengths and in multiple locations surrounding the rover to account for possible shadowing effects). The PBL temperature profile (which would thus be the thermal response of the atmosphere to the previously described forcings) could also be measured by the same IR radiometer looking in a different direction or by a separately mounted IR radiometer, either of which should be designed to measure the full range of PBL heights that might be experienced. The temperature profiles thus acquired could provide insight into a range of PBL behavior, including structure, stability, and height. Temperature sensitivities of a few tenths of K should be sufficient for quantifying changes and heat fluxes. Atmospheric optical depth could also be measured through the IR radiometer at appropriate wavelengths or, alternately, through conjunction with the lander's or rover's visible wavelength camera.

[181] The inclusion of a sonic anemometer would be a significant step forward for meteorological measurements. Previous hot-wire anemometry has been limited by contamination of the measurements from the presence and thermal effects of the lander itself (sections 4.1.1 and 4.1.2), despite the best attempts to mitigate the effect, as well as being intrinsically too slow to measure turbulent fluctuations of the wind [*Seiff et al.*, 1997; *Hess et al.*, 1972]. A sonic anemometer would allow the capability of resolving the full three-dimensional wind, enhance knowledge of near-surface winds, and be capable of making measurements quickly enough to resolve eddies as well as be able to be placed farther from the lander to minimize thermal contamination from the lander itself of the local atmospheric conditions. To resolve vertical winds adequately (which would have the smallest magnitude of the three directions), an instrumental sensitivity of $\simeq$1–10 cm s^{-1} would be desired.

[182] The coincident and high-frequency measurements of both winds and temperature would yield information about heat and momentum fluxes and the turbulence spectrum [*Laubach and McNaughton*, 1998; *Villalobos*, 1997]. In addition to their intrinsic value, these measurements would also serve as an important constraint upon the development and validation of 1-D and 3-D numerical models of the PBL.

[183] Surface pressure measurements with a sensitivity of $\simeq$10 Pa over a range of 0 to 1000 Pa would be sufficient for detecting and characterizing both large-scale effects (e.g., seasonal pressure variations, tidal and synoptic systems) as well as local phenomena (e.g., dust devils). Measurement of

surface pressure would also provide an important input to and constraint for radiative and turbulent models.

[184] The inclusion of a tunable laser spectrometer would enable measurements of concentrations of water vapor as well as other trace gases, such as CH_4. Ideally it would be located in a position closely related to the sonic anemometer to permit calculation of vapor fluxes as well. Sensitivity to vapor quantities in the 1–10 ppbv range would be sufficient to resolve water and trace gases at previously observed values [*Jakosky*, 1985; *Krasnopolsky et al.*, 2004; *Encrenaz*, 2004]. In particular, measurement of fluxes of water vapor will allow for testing of models of atmospheric mixing that have had to rely on extrapolation of terrestrial theories by orders of magnitude (in air and vapor density) and many tens of K (in temperature) from the regimes for which they were designed and tested [*Tillman et al.*, 1994; *Larsen et al.*, 2002].

[185] This recommendation for an instrument suite would present many enhancements over ones that have been flown or are presently planned for Martian landers and rovers. With careful choice of instrument type and sensor placement (as far away from obstructions and the lander or rover itself), this recommended suite could provide an opportunity to measure quantities and their fluxes together in a way that has not been possible with previous missions. Additionally, this recommended suite could provide a more complete picture of the PBL through measurements of not only the (thermal) forcing of the PBL but also its eddy responses, closing the loop on the drive and response feedback system.

7.3.3. Example Future Orbital Mission Concept: Orbiter-to-Orbiter Radio Occultation

[186] As described in section 4.3.1, the radio occultation method offers a good method for observing the PBL phenomena and characteristics from orbit, despite of limitations such as poor horizontal resolution along the line of sight as well as (in case of the orbiter-to-Earth geometry) limited spatial and diurnal coverage. So far only the orbiter-to-Earth geometry has been used, but the orbiter-to-orbiter geometry has also been studied [e.g., *Kursinski et al.*, 2004, 2009]. This approach, depending on the number of satellites and orbits used, would potentially provide superior latitudinal, longitudinal and diurnal coverage. For instance, the MGS-to-Earth occultations sampled the PBL only twice per sol at two widely separated local times, effectively preventing characterization of the full diurnal cycle on that sol (or small span of sols, due to the slow change in local time sampled). The highly elliptical orbit of the MEx has been better in this respect, but the long period of the MEx orbit reduces the sampling rate. By comparison the original Mars Atmospheric Constellation Observatory concept [*Kursinski et al.*, 2004] comprising three satellites performing mutual microwave occultations would have provided global and full diurnal coverage 12 times per Martian year.

[187] A revised concept, the Mars Astrobiology and Climate Observatory, comprising two satellites and utilizing millimeter waves has been proposed more recently [*Kursinski et al.*, 2008, 2009]. Instead of implementing this concept as a dedicated mission, similar objectives could also be met by combining a smaller subsatellite with a larger orbiter.

TABLE A1. Acronyms and Symbols

	Definition
α	surface albedo
α_1	Kolmogorov spectral constant
ASI/MET	Atmospheric Structure Instrument and Meteorology package (MPF)
E_{KT}	turbulence kinetic energy
η	Kolmogorov dissipation length scale
$\Phi_m, \Phi_h, \Phi_w, \Phi_u, \Phi_\theta$	dimensionless universal functions for vertical variation of velocity and temperature gradients, vertical and horizontal velocities, and temperature
Γ	lapse rate: $-\frac{d\theta}{dz}$
γ	vertical shear of geostrophic wind
G	geostrophic wind velocity
GRS	Gamma Ray Spectrometer (Mod)
h_{CL}	condensation height
HEND	High-Energy Neutron Detector (MOd)
h	depth of PBL
HRSC	High-Resolution Stereo Camera (MEx)
IMP	Imager for Mars Pathfinder (MPF)
IR	Infrared
IRTM	infrared thermal mapper (VO)
I	thermal inertia
κ	von Kármán constant
ℓ	length scale typical of turbulent eddies (mixing length)
L	Monin-Obukhov length scale
Λ	Local Monin-Obukhov length scale
MCS	Mars Climate Sounder (MRO)
MER	Mars Exploration Rover
MET	M Meteorological package (PHX)
MetNet	Meteorological Network: Mars lander and mission concept for atmospheric studies developed by a consortium led by the Finnish Meteorological Institute
MEx	Mars Express
MGS	Mars Global Surveyor
Mini-TES	Miniature Thermal Emission Spectrometer (MER)
MNL	Mars Network lander; see also MetNet
MOC	Mars Observer Camera (MGS)
MOd	Mars Odyssey 2001
MOLA	Mars Orbiter Laser Altimeter (MGS)
MPF	Mars Pathfinder
MRO	Mars Reconnaissance Orbiter
MSL	Mars Science Laboratory
μ	refractive index
n	number density
OMEGA	Observatoire pour la Minéralogie, l'Eau, les Glaces et l'Activité; visible and infrared mapping spectrometer (MEx)
p	atmospheric pressure
PBL	planetary boundary layer
PFS	Planetary Fourier Spectrometer (MEx)
Phobos 2	Phobos and Mars mission launched by Soviet Union
PHX	Phoenix
q	specific humidity
ρ	atmospheric density
RAC	Robotic Arm Camera (PHX)
r_{eff}	effective radius of dust suspended dust particles' size distribution
REMS	Rover Environmental Monitoring Station (MSL)
RH	relative humidity
RO	radio occultation
RSM	remote sensing mast (MSL)
RS	radio science
RTG	radioisotope thermal generator
SPICAM	Spectroscopie Pour l'Investigation des Caractéristiques de l'Atmosphère de Mars (MEx ultraviolet and infrared atmospheric spectrometer)
SSI	Surface Stereo Imager

TABLE A1. (continued)

	Definition
T_f, T_m, T_t	time scales for external processes, development of mean profiles and eddy overturning
θ	atmospheric temperature
θ_0	reference temperature
θ_*	convective temperature scale
Θ	potential temperature
τ	optical thickness
τ_s	horizontal shear stress
TECP	Thermal and Electrical Conductivity Probe (PHX)
TES	Thermal Emission Spectrometer (MGS)
TGM	Trace Gas Mission
THEMIS	Thermal Emission Imaging System (MOd)
T_s	surface temperature
u_*	friction velocity scale
$\vec{V}$	wind speed and direction
VIS	Visual Imaging Subsystem (VO)
VL1	Viking Lander 1
VL2	Viking Lander 2
VL	Viking lander
VMIS	Viking Meteorology Instrument System (VL)
VO	Viking orbiter
w	vertical wind
w_*	convective velocity scale
z_0	surface roughness length (mechanical)
z_{0T}	surface roughness length for thermal properties
Z	altitude above the surface

7.4. Concluding Remarks

[188] In this paper we have sought to provide a comprehensive and timely summary of our knowledge of the atmospheric boundary layer on Mars. It is clear that our knowledge of this part of the Martian environment is already quite advanced. Current modeling techniques are apparently capable of reasonably accurate predictions of the conditions encountered under many circumstances and of successfully representing the impact of the boundary layer on other aspects of the Martian environment and circulation. It is also clear, however, that our knowledge still relies heavily (and somewhat uncomfortably) (1) on exploiting the results of much more detailed and comprehensive investigations of the Earth's atmospheric boundary layer and (2) on extrapolating terrestrial modeling approaches beyond their formally verified parameter ranges. Although the available observations of the Martian PBL have not so far provided strong evidence to invalidate this approach, there remains a clear need for more and detailed observational campaigns to enable more rigorous testing of the full range of boundary layer models for Mars. Because of this and the intrinsic variability of the Martian environment on all space scales and time scales, such measurements should therefore continue to feature strongly in future in situ and remote sounding investigations, even when atmospheric science is not necessarily the prime focus of the mission. The neglect of such future studies of the near-surface Martian environment would not only hold back scientific progress concerning the present and past climate evolution of Mars but could also place future lander missions at a significant and avoidable risk of failure, due to

an inability to anticipate the full range of potential environmental hazards close to the Martian surface.

Appendix A: Acronyms, Abbreviations, and Symbols

[189] Table A1 provides a reference list of acronyms, abbreviations, and mathematical symbols that are used in various places in this paper, together with relevant definitions or explanations. Many of the acronyms and abbreviations refer to specific spacecraft or instrument suites and are in common use by the Mars community. The mathematical symbols are generally defined within the text, but their definitions are reproduced here for the convenience of the reader.

REFERENCES

Alexakis, A. (2009), Stratified shear flow instabilities at large Richardson numbers, *Phys. Fluids*, 21, 054108, doi:10.1063/1.3147934.

Alfonsi, G. (2009), Reynolds-averaged Navier-Stokes equations for turbulence modeling, *Rev. Mech. Appl.*, 62, 040802.

Allison, M., J. D. Ross, and N. Solomon (1999), Mapping the Martian meteorology, in *Fifth International Conference on Mars, July 18–23, 1999, Pasadena CA* [CD-ROM], *LPI Contrib.*, 972, Abstract 6102.

André, J., and P. Lacarrére (1980), Simulation numérique détaillée de la couche limite atmosphérique: Comparaison avec la situation des 2 et 3 Juillet 1977 á Voves, *La Météorol.*, 6(22), 5–49.

André, J., G. De Moor, P. Lacarrére, G. Therry, and R. du Vachat (1978), Modeling 24-hour evolution of mean and turbulent structures of planetary boundary layer, *J. Atmos. Sci.*, 35, 1861–1883.

Atreya, S. K., et al. (2006), Oxidant enhancement in Martian dust devils and storms: Implications for life and habitability, *Astrobiology*, 6, 439–450.

Bagnold, R. A. (1941), *The Physics of Blown Sand and Desert Dunes*, Methuen, New York.

Banerdt, B., et al. (1996), INTERMARSNET phase–A study report, *Eur. Space Agency Sci. Tech. Rep.*, ESA STR (96)2, 158 pp.

Basu, S., J.-F. Vinuesa, and A. Swift (2008), Dynamic LES modeling of a diurnal cycle, *J. Appl. Meteorol. Climatol.*, 47, 1156–1174.

Bertaux, J.-L., et al. (2006), SPICAM on Mars express: Observing modes and overview of UV spectrometer data and scientific results, *J. Geophys. Res.*, 111, E10S90, doi:10.1029/2006JE002690.

Blackadar, A. (1957), Boundary-layer wind maxima and their significance for the growth of nocturnal inversion, *Bull. Am. Meteorol. Soc.*, 38, 283–290.

Blackadar, A. (1962), The vertical distribution of wind and turbulent exchange in a neutral atmosphere, *J. Geophys. Res.*, 67, 3095–3102.

Blumsack, S. L., P. J. Gierasch, and S. R. Wessel (1973), An analytical and numerical study of the Martian planetary boundary layer over slopes, *J. Atmos. Sci.*, 30, 66–80.

Bougeault, P., and J. André (1986), On the stability of the third-order turbulence closure for the modeling of the stratocumulus-topped boundary layer, *J. Atmos. Sci.*, 43, 1574–1581.

Bougeault, P., and P. Lacarrére (1989), Parameterization of orography-induced turbulence in a mesobeta-scale model, *Mon. Weather Rev.*, 117, 1872–1890.

Bougher, S., G. Keating, R. Zurek, J. Murphy, R. Haberle, J. Hollingsworth, and R. T. Clancy (1999), Mars Global Surveyor aerobraking: Atmospheric trends and model interpretation, *Adv. Space Res.*, 23, 1887–1897.

Boynton, W. V., et al. (2004), The Mars Odyssey Gamma Ray Spectrometer instrument suite, *Space Sci. Rev.*, 110, 37–83.

Brutsaert, W. H. (1982), Exchange processes at the Earth-atmosphere interface, in *Engineering Meteorology*, edited by E. Plate, pp. 319–369, Elsevier, Amsterdam.

Burchard, H. (2001), On the q^2l equation by Mellor and Yamada (1982), *J. Phys. Oceanogr.*, 31, 1377–1387.

Cantor, B. A., P. B. James, M. Caplinger, and M. J. Wolff (2001), Martian dust storms: 1999 Mars Orbiter Camera observations, *J. Geophys. Res.*, 106, 23,653–23,687.

Cantor, B., M. Malin, and K. S. Edgett (2002), Multiyear Mars Orbiter Camera (MOC) observations of repeated Martian weather phenomena during the northern summer season, *J. Geophys. Res.*, 107(E3), 5014, doi:10.1029/2001JE001588.

Canuto, V. (1992), Turbulent convection with overshootings: Reynolds stress approach, *J. Astrophys.*, 392, 218–232.

Canuto, V., A. Howard, Y. Cheng, and M. Dubovikov (2001), Ocean turbulence. Part I: One-point closure model-momentum and heat vertical diffusivities, *J. Phys. Oceanogr.*, 31, 1413–1426.

Canuto, V., Y. Cheng, and A. Howard (2005), What causes divergences in local second-order models?, *J. Atmos. Sci.*, 62, 1645–1651.

Canuto, V., Y. Cheng, A. Howard, and I. Esau (2008), Stably stratified flows: A model with no Ri(cr), *J. Atmos. Sci.*, 65, 2437–2447.

Chamberlain, T. E., H. L. Cole, R. G. Dutton, G. C. Greene, and J. E. Tillman (1976), Atmospheric measurements on Mars: The Viking meteorology experiment, *Bull. Am. Meteor. Soc.*, 57, 1094–1104.

Chassefière, E., J. E. Blamont, V. A. Krasnopolsky, O. I. Korablev, S. K. Atreya, and R. A. West (1992), Vertical structure and size distributions of Martian aerosols from solar occultation measurements, *Icarus*, 97, 46–69.

Chassefière, E., P. Drossart, and O. Korablev (1995), Post-Phobos model for the altitude and size distribution of dust in the low Martian atmosphere, *J. Geophys. Res.*, 100, 5525–5539.

Cheng, Y., and V. Canuto (1994), Stably stratified shear turbulence: A new model for the energy dissipation length scale, *J. Atmos. Sci.*, 51, 2384–2396.

Cheng, Y., V. M. Canuto, and A. Howard (2002), An improved model for the turbulent PBL, *J. Atmos. Sci.*, 59, 1550–1565.

Cheng, Y., V. Canuto, and A. Howard (2005), Nonlocal convective PBL model based on new third- and fourth-order moments, *J. Atmos. Sci.*, 62, 2189–2204.

Chicarro, A. F., et al. (1993), Marsnet phase–A study report, *Eur. Space Agency Sci. Tech. Rep.*, ESA STR (93)2, 120 pp.

Christensen, P. R., et al. (2001), Mars Global Surveyor Thermal Emission Spectrometer experiment: Investigation description and surface science results, *J. Geophys. Res.*, 106, 23,823–23,872.

Christensen, P. R., et al. (2003), Miniature Thermal Emission Spectrometer for the Mars Exploration Rovers, *J. Geophys. Res.*, 108(E12), 8064, doi:10.1029/2003JE002117.

Clancy, R. T., B. J. Sandor, M. J. Wolff, P. R. Christensen, M. D. Smith, J. C. Pearl, B. J. Conrath, and R. J. Wilson (2000), An intercomparison of ground-based millimeter, MGS TES, and Viking atmospheric temperature measurements: Seasonal and interannual variability of temperatures and dust loading in the global Mars atmosphere, *J. Geophys. Res.*, *105*, 9553–9572.

Clancy, R. T., M. J. Wolff, and P. R. Christensen (2003), Mars aerosol studies with the MGS TES emission phase function observations: Optical depths, particle sizes, and ice cloud types versus latitude and solar longitude, *J. Geophys. Res.*, *108*(E9), 5098, doi:10.1029/2003JE002058.

Conrath, B. J. (1975), Thermal structure of the Martian atmosphere during the dissipation of the dust storm of 1971, *Icarus*, *24*, 36–46.

Conrath, B. J., J. C. Pearl, M. D. Smith, W. C. Maguire, S. Dason, and M. S. Kaelberer (2000), Mars Global Surveyor Thermal Emission Spectrometer (TES) observations: Atmospheric temperatures during aerobraking and science phasing, *J. Geophys. Res.*, *105*, 9509–9519.

Cot, C. (2001), Equatorial mesoscale wind and temperature fluctuations in the lower atmosphere, *J. Geophys. Res.*, *106*, 1523–1532.

Crozier, W. D. (1964), The electric field of a New Mexico dust devil, *J. Geophys. Res.*, *69*, 5427–5429.

Cuxart, J., P. Bougeault, and J.-L. Redelsperger (2000), A turbulence scheme allowing for meso-scale and large-eddy simulations, *Q. J. R. Meteorol. Soc.*, *126*, 1–30.

Davy, R., P. A. Taylor, W. Weng, and P. Li (2009), A model of dust in the Martian lower atmosphere, *J. Geophys. Res.*, *114*, D04108, doi:10.1029/2008JD010481.

Davy, R., J. A. Davis, P. A. Taylor, C. F. Lange, W. Weng, J. Whiteway, and H. P. Gunnlaugson (2010), Initial analysis of air temperature and related data from the Phoenix MET station and their use in estimating turbulent heat fluxes, *J. Geophys. Res.*, *115*, E00E13, doi:10.1029/2009JE003444.

Deardorff, J. (1972), Theoretical expression for the countergradient vertical heat flux, *J. Geophys. Res.*, *77*, 5900–5904.

Deardorff, J. (1976), Clear and cloud-capped mixed layers–Their numerical simulation, structure and growth and parameterization, in *Seminars on the Treatment of the Boundary Layer in Numerical Weather Prediction*, pp. 234–284, Eur. Cent. for Medium Range Weather Forecasts, Reading, U. K.

Deleersnijder, E., and H. Burchard (2003), Reply to Mellor's comments on "Stability of algebraic non-equilibrium second-order closure models" (Ocean Modelling 3 (2001) 33–50), *Ocean Modell.*, *5*, 291–293.

Deleersnijder, E., and P. Luyten (1994), On the practical advantages of the quasi-equilibrium version of the Mellor and Yamada level 2.5 turbulence closure applied to marine modeling, *Appl. Math. Modell.*, *18*, 281–287.

Deleersnijder, E., E. Hanert, H. Burchard, and H. Dijkstra (2008), On the mathematical stability of stratified flow models with local turbulence closure schemes, *Ocean Dyn.*, *58*, 237–246.

Dellar, P., and R. Salmon (2005), Shallow water equations with a complete Coriolis force and topography, *Phys. Fluids*, *17*, 106601, doi:10.1063/1.2116747.

Delory, G. T., W. M. Farrell, S. K. Atreya, N. O. Renno, A.-S. Wong, S. A. Cummer, D. D. Sentman, J. R. Marshall, S. C. R. Rafkin, and D. C. Catling (2006), Oxidant enhancement in Martian dust devils and storms: Storm electric fields and electron dissociative attachment, *Astrobiology*, *6*(3), 451–462.

Dewan, E. M. (1979), Stratospheric wave spectra resembling turbulence, *Science*, *204*, 832–835.

Dewan, E. M., and R. E. Good (1986), Saturation and the "universal" spectrum for vertical profiles of horizontal scalar winds in the atmosphere, *J. Geophys. Res.*, *91*, 2742–2748.

Douté, S., B. Schmitt, Y. Langevin, J.-P. Bibring, F. Altieri, G. Bellucci, B. Gondet, F. Poulet, and the MEX OMEGA Team (2007), South Pole of Mars: Nature and composition of the icy terrains from Mars Express OMEGA observations, *Planet. Space Sci.*, *55*, 113–133.

Drake, N. B., L. K. Tamppari, R. D. Baker, B. A. Cantor, and A. S. Hale (2006), Dust devil tracks and wind streaks in the North Polar region of Mars: A study of the 2007 Phoenix Mars lander sites, *Geophys. Res. Lett.*, *33*, L19S02, doi:10.1029/2006GL026270.

Ellehoj, M. D., et al. (2010), Convective vortices and dust devils at the Phoenix Mars mission landing site, *J. Geophys. Res.*, *115*, E00E16, doi:10.1029/2009JE003413.

Emanuel, K. A. (1994), *Atmospheric Convection*, Oxford Univ. Press, Oxford, U. K.

Encrenaz, T. (2004), Minor species in the Martian atmosphere from ground-based and PFS Mars Express spectroscopy, paper presented at Semaine de l'Astrophysique Francaise, Soc. Fr. d'Astronomie and d'Astrophysique Paris, 14–18 June.

Farrell, W. M., G. T. Delory, and S. K. Atreya (2006), Martian dust storms as a possible sink of atmospheric methane, *Geophys. Res. Lett.*, *33*, L21203, doi:10.1029/2006GL027210.

Fedorova, A. A., O. I. Korablev, J.-L. Bertaux, A. V. Rodin, F. Montmessin, D. A. Belyaev, and A. Reberac (2009), Solar infrared occultation observations by SPICAM experiment on Mars Express: Simultaneous measurements of the vertical distributions of H_2O, CO_2 and aerosols, *Icarus*, *200*, 96–117.

Fergason, R. L., P. R. Christensen, and H. H. Kieffer (2006), High-resolution thermal inertia derived from the Thermal Emission Imaging System (THEMIS): Thermal model and applications, *J. Geophys. Res.*, *111*, E12004, doi:10.1029/2006JE002735.

Ferrero, E., and N. Colonna (2006), Nonlocal treatment of the buoyancy-shear-driven boundary layer, *J. Atmos. Sci.*, *63*, 2653–2662.

Ferrero, E., and M. Racca (2004), The role of the nonlocal transport in modeling the shear-driven atmospheric boundary layer, *J. Atmos. Sci.*, *61*, 1434–1445.

Ferri, F., P. H. Smith, M. Lemmon, and N. O. Rennó (2003), Dust devils as observed by Mars Pathfinder, *J. Geophys. Res.*, *108*(E12), 5133, doi:10.1029/2000JE001421.

Forget, F., F. Hourdin, R. Fournier, C. Hourdin, O. Talagrand, M. Collins, S. R. Lewis, and P. L. Read (1999), Improved general circulation models of the Martian atmosphere from the surface to above 80 km, *J. Geophys. Res.*, *104*, 24,155–24,176.

Forget, F., et al. (2007), Remote sensing of surface pressure on Mars with the Mars Express/OMEGA spectrometer: 1. Retrieval method, *J. Geophys. Res.*, *112*, E08S15, doi:10.1029/2006JE002871.

Formisano, V., D. Grassi, N. I. Ignatiev, and L. Zasova (2001), IRIS mariner 9 data revisited: Water and dust daily cycles, *Planet. Space Sci.*, *49*, 1331–1346.

Fouchet, T., et al. (2007), Martian water vapor: Mars Express PFS/LW observations, *Icarus*, *190*, 32–49.

Fritts, D. C., and M. J. Alexander (2003), Gravity wave dynamics and effects in the middle atmosphere, *Rev. Geophys.*, *41*(1), 1003, doi:10.1029/2001RG000106.

Galperin, B., and S. Sukoriansky (2010), Geophysical flows with anisotropic turbulence and dispersive waves: Flows with stable stratification, *Ocean Dyn.*, *60*, 1319–1337.

Galperin, B., L. Kantha, S. Hassid, and A. Rosati (1988), A quasi-equilibrium turbulent energy model for geophysical flows, *J. Atmos. Sci.*, *45*, 55–62.

Galperin, B., L. Kantha, G. Mellor, and A. Rosati (1989), Modeling rotating stratified turbulent flows with application to oceanic mixed layers, *J. Phys. Oceanogr.*, *7*, 901–916.

Galperin, B., S. Sukoriansky, and P. Anderson (2007), On the critical Richardson number in stably stratified turbulence, *Atmos. Sci. Let.*, *8*, 65–69.

Garratt, J. R. (1992), *The Atmospheric Boundary Layer*, Cambridge Univ. Press, Cambridge, U. K.

Gerkema, T., J. Zimmerman, L. Maas, and H. van Haren (2008), Geophysical and astrophysical fluid dynamics beyond the tradi-

tional approximation, *Rev. Geophys.*, *46*, RG2004, doi:10.1029/2006RG000220.

Gierasch, P. J., and R. M. Goody (1968), A study of the thermal and dynamical structure of the lower Martian atmosphere, *Planet Space Sci.*, *16*, 615–646.

Girimaji, S. (2000), Pressure-strain correlation modeling of complex turbulent flows, *J. Fluid Mech.*, *422*, 91–123.

Golombek, M. P., et al. (1997), Overview of the Mars pathfinder mission and assessment of landing site predictions, *Science*, *278*, 1743–1748.

Gómez-Elvira, J., and REMS Team (2008), Environmental monitoring station for Mars Science Laboratory, *LPI Contrib.*, *1447*, Abstract 9052.

Grassi, D., M. D. Smith, M. J. Wolff, R. E. Arvidson, V. Formisano, and N. I. Ignatiev (2006), Simultaneous observations of Martian atmosphere by PFS-MEx and MiniTES-MER, paper presented at European Planetary Science Congress, Europlanet, Berlin.

Greeley, R., and J. D. Iversen (1985), *Wind as a Geological Process on Earth, Mars, Venus and Titan*, Cambridge Univ. Press, New York.

Gryanik, V., J. Hartmann, S. Raasch, and M. Schoroter (2005), A refinement of the Millionschikov quasi-normality hypothesis for convective boundary layer turbulence, *J. Atmos. Sci.*, *62*, 2632–2638.

Gunnlaugsson, H. P., et al. (2008), Telltale wind indicator for the Mars Phoenix lander, *J. Geophys. Res.*, *113*, E00A04, doi:10.1029/2007JE003008. [Printed *114*(E3), 2009.]

Haberle, R., H. Houben, R. Hertenstein, and T. Herdtle (1993a), A boundary layer model for Mars: Comparison with Viking lander and entry data, *J. Atmos. Sci.*, *50*, 1544–1559.

Haberle, R. M., J. B. Pollack, J. R. Barnes, R. W. Zurek, C. B. Leovy, J. R. Murphy, J. Schaeffer, and H. Lee (1993b), Mars atmospheric dynamics as simulated by the NASA/Ames general circulation model, *J. Geophys. Res.*, *102*, 13,301–13,311.

Harri, A.-M., et al. (1998), Meteorological observations on Martian surface: Met-packages of Mars-96 small stations and penetrators, *Planet. Space Sci.*, *46*, 779–793.

Harri, A.-M., et al. (1999), Network science landers for Mars, *Adv. Space Res.*, *23*, 1915–1924.

Harri, A.-M., W. Schmidt, H. Guerrero, L. Vazquez, and the MetNet Team (2010), Metnet network precursor mission, *EPSC Abstracts*, *5*, EPSC2010-739.

Hassid, S., and B. Galperin (1983), A turbulent energy model for geophysical flows, *Boundary Layer Meteorol.*, *26*, 397–412.

Hassid, S., and B. Galperin (1994), Modeling rotating flows with neutral and unstable stratification, *J. Geophys. Res.*, *99*, 12,533–12,548.

Heavens, N. G., M. I. Richardson, and A. D. Toigo (2008), Two aerodynamic roughness maps derived from Mars Orbiter Laser Altimeter (MOLA) data and their effects on boundary layer properties in a Mars general circulation model (GCM), *J. Geophys. Res.*, *113*, E02014, doi:10.1029/2007JE002991.

Hébrard, E., P. Coll, B. Marticorena, G. Bergametti, F. Montmessin, and F. Forget (2008), An aerodynamic roughness map derived from Martian rock abundance data and its effects on aeolian erosion thresholds in a MGCM, *LPI Contrib.*, *1447*, Abstract 9057.

Hess, S. L., R. M. Henry, J. Kuettner, C. B. Leovy, and J. A. Ryan (1972), Meteorology experiments: The Viking Mars lander, *Icarus*, *16*, 196–204.

Hess, S. L., et al. (1976), Preliminary meteorological results on Mars from the Viking 1 lander, *Science*, *193*, 788–791.

Hess, S. L., R. M. Henry, C. B. Leovy, J. A. Ryan, and J. E. Tillman (1977), Meteorological results from the surface of Mars: Viking 1 and 2, *J. Geophys. Res.*, *82*, 4559–4574.

Hinson, D. P., and R. J. Wilson (2002), Transient eddies in the southern hemisphere of Mars, *Geophys. Res. Lett.*, *29*(7), 1154, doi:10.1029/2001GL014103.

Hinson, D. P., and R. J. Wilson (2004), Temperature inversions, thermal tides, and water ice clouds in the Martian tropics, *J. Geophys. Res.*, *109*, E01002, doi:10.1029/2003JE002129.

Hinson, D. P., R. A. Simpson, J. D. Twicken, G. L. Tyler, and F. M. Flasar (1999), Initial results from radio occultation measurements with Mars Global Surveyor, *J. Geophys. Res.*, *104*, 26,997–27,012.

Hinson, D. P., G. L. Tyler, J. L. Hollingsworth, and R. J. Wilson (2001), Radio occultation measurements of forced atmospheric waves on Mars, *J. Geophys. Res.*, *106*, 463–1480.

Hinson, D. P., R. J. Wilson, M. D. Smith, and B. J. Conrath (2003), Stationary planetary waves in the atmosphere of Mars during southern winter, *J. Geophys. Res.*, *108*(E1), 5004, doi:10.1029/2002JE001949.

Hinson, D. P., M. D. Smith, and B. J. Conrath (2004), Comparison of atmospheric temperatures obtained through infrared sounding and radio occulation by Mars Global Surveyor, *J. Geophys. Res.*, *109*, E12002, doi:10.1029/2004JE002344.

Hinson, D. P., M. Pätzold, S. Tellmann, B. Häusler, and G. L. Tyler (2008), The depth of the convective boundary layer on Mars, *Icarus*, *198*, 57–66.

Holstein-Rathlou, C., et al. (2010), Winds at the Phoenix landing site, *J. Geophys. Res.*, *115*, E00E18, doi:10.1029/2009JE003411.

Holtslag, A., and B. Boville (1993), Local versus non-local boundary layer diffusion in a global climate model, *J. Clim.*, *6*, 1825–1842.

Holtslag, A., and C. Moeng (1991), Eddy diffusivity and counter-gradient transport in the convective atmospheric boundary layer, *J. Atmos. Sci.*, *48*, 1690–1700.

Hunt, G. E., A. O. Pickersgill, P. B. James, and N. Evans (1981), Daily and seasonal Viking observations of Martian bore wave systems, *Nature*, *293*, 630–633.

Inada, A., et al. (2008), Dust haze in Valles Marineris observed by HRSC and OMEGA on board Mars Express, *J. Geophys. Res.*, *113*, E02004, doi:10.1029/2007JE002893.

Ivanov, A. B., and D. O. Muhleman (2001), Cloud reflection observations: Results from the Mars Orbiter Laser Altimeter, *Icarus*, *154*, 190–206.

Jakosky, B. M. (1985), The seasonal cycle of water on Mars, *Space Sci. Rev.*, *41*, 131–200.

Jakosky, B. M., and C. B. Farmer (1982), The seasonal and global behavior of water vapor in the Martian atmosphere: Complete results of the viking atmospheric water detector on Mars, *J. Geophys. Res.*, *87*, 2999–3019.

Jakosky, B. M., M. T. Mellon, E. S. Varnes, W. C. Feldman, W. V. Boynton, and R. M. Haberle (2005), Mars low-latitude neutron distribution: Possible remnant near-surface water ice and a mechanism for its recent emplacement, *Icarus*, *175*, 58–67.

James, P. B., and B. A. Cantor (2001), Martian north polar cap recession: 2000 Mars Orbiter Camera observations, *Icarus*, *154*, 131–144.

Joshi, M. M., B. N. Lawrence, and S. R. Lewis (1996), The effect of spatial variations in unresolved topography on gravity wave drag in the Martian atmosphere, *Geophys. Res. Lett.*, *23*, 2927–2930.

Kanak, K. M., D. K. Lilly, and J. T. Snow (2000), The formation of vertical Vortices in the convective boundary layer, *Q. J. R. Meteorol. Soc.*, *126*, 2789–2810.

Kantha, L., and S. Carniel (2009), A note on modeling mixing in stably stratified flows, *J. Atmos. Sci.*, *66*, 2501–2505.

Kantha, L., and C. Clayson (1994), An improved mixed-layer model for geophysical applications, *J. Geophys. Res.*, *99*, 25,235–25,266.

Karelsky, K. V., and A. S. Petrosyan (1995), Numerical simulations of the near surface phenomena on Mars, *Adv. Space Res.*, *11*(6), 45–48.

Karelsky, K., A. Petrosyan, and I. Smirnov (2007), A new model for boundary layer flows interacting with particulates in land surface on complex terrain, *Q. J. Hung. Meteorol. Serv.*, *111*(2–3), 149–159.

Kasahara, A. (2003), The roles of the horizontal component of the Earth's angular velocity in nonhydrostatic linear models, *J. Atmos. Sci.*, *60*, 1085–1095.

Kass, D. M., J. T. Schofield, T. I. Michaels, S. C. R. Rafkin, M. I. Richardson, and A. D. Toigo (2003), Analysis of atmospheric mesoscale models for entry, descent, and landing, *J. Geophys. Res.*, *108*(E12), 8090, doi:10.1029/2003JE002065.

Kauhanen, J., T. Siili, S. Järvenoja, and H. Savijärvi (2008), The Mars limited area model and simulations of atmospheric circulations for the Phoenix landing area and season of operation, *J. Geophys. Res.*, *113*, E00A14, doi:10.1029/2007JE003011.

Kieffer, H. H., and T. N. Titus (2001), TES mapping of Mars' north seasonal cap, *Icarus*, *154*, 162–180.

Kieffer, H. H., S. C. Chase, T. Z. Martin, E. D. Miner, and F. D. Palluconi (1976), Martian north pole summer temperatures: Dirty water ice, *Science*, *194*, 1341–1344.

Kieffer, H. H., T. Z. Martin, A. R. Peterfreund, B. M. Jakosky, E. D. Miner, and F. D. Palluconi (1977), Thermal and albedo mapping of Mars during the Viking primary mission, *J. Geophys. Res.*, *82*, 4249–4291.

Kitamura, Y. (2010), Modifications to the Mellor-Yamada-Nakanishi-Niino (MYNN) model for the stable stratification case, *J. Meteorol. Soc. Jpn.*, *88*, 857–864.

Kleinböhl, A., et al. (2009), Mars Climate Sounder limb profile retrieval of atmospheric temperature, pressure, and dust and water ice opacity, *J. Geophys. Res.*, *114*, E10006, doi:10.1029/2009JE003358.

Kok, J. F., and N. O. Renno (2008), Electrostatics in wind-blown sand, *Phys. Rev. Lett.*, *100*, 014501, doi:10.1103/PhysRevLett.100.014501.

Kok, J. F., and N. O. Renno (2009), Electrification of wind-blown sand on Mars and its implications for atmospheric chemistry, *Geophys. Res. Lett.*, *36*, L05202, doi:10.1029/2008GL036691.

Korablev, O. I. (2002), Solar occultation measurements of the Martian atmosphere on the Phobos spacecraft: Water vapor profile, aerosol parameters, and other results, *Sol. Syst. Res.*, *36*, 12–34.

Krasnopolsky, V. A., J. P. Maillard, and T. C. Owen (2004), Detection of methane in the Martian atmosphere: Evidence for life, *Geophys. Res. Abstr.*, *6*, 06169.

Kurbatskiy, A., and L. Kurbatskaya (2006), Three-parameter model of turbulence for the atmospheric boundary layer over an urbanized surface, *Izvestiya Atmos. Oceanic Phys.*, *42*, 439–455.

Kurbatskiy, A., and L. Kurbatskaya (2009), $E - \epsilon - \langle \theta^2 \rangle$ turbulence closure model for an atmospheric boundary layer including the urban canopy, *Meteorol. Atmos. Phys.*, *104*, 63–81.

Kursinski, E. R., et al. (2004), The Mars Atmospheric Constellation Observatory (MACO) concept, in *Occultations for Probing Atmosphere and Climate*, edited by G. Kirchengast, U. Foelsche, and A. Steiner, pp. 393–405, Springer, Berlin.

Kursinski, E., J. Lyons, M. Richardson, W. Folkner, A. Otarola, and D. Ward (2008), The Mars Astrobiology and Climate Observatory (MACO), paper presented at 37th COSPAR Scientific Assembly, Montreal, Que., Canada.

Kursinski, E. R., J. Lyons, C. Newman, M. I. Richardson, D. Ward, and A. C. Otarola (2009), A global observing system for Mars: The dual satellite Mars Astrobiology and Climate Observatory (MACO), *Eos Trans. AGU*, *90*(52), Fall Meet. Suppl., Abstract P54B-11.

Kuzmin, R. O., E. V. Zabalueva, I. G. Mitrofanov, M. L. Litvak, A. V. Rodin, W. V. Boynton, and R. S. Saunders (2007), Seasonal redistribution of water in the surficial Martian regolith: Results from the Mars Odyssey high-energy neutron detector (HEND), *Sol. Syst. Res.*, *41*, 89–102.

Langevin, Y., F. Poulet, J.-P. Bibring, B. Schmidtt, S. Douté, and B. Gondet (2005), Summer evolution of the north polar cap of Mars as observed by OMEGA/Mars Express, *Science*, *307*, 1581–1584.

Larsen, S. E., H. E. Jørgensen, L. Landberg, and J. E. Tillman (2002), Aspects of the atmospheric surface layers on Mars and Earth, *Boundary Layer Meteorol.*, *105*, 451–470.

Laubach, J., and K. G. McNaughton (1998), A spectrum-independent procedure for correcting eddy fluxes measured with separated sensors, *Boundary Layer Meteorol.*, *89*, 445–467.

Launder, B., G. Reece, and W. Rodi (1975), Progress in development of a Reynolds-stress turbulence closure, *J. Fluid Mech.*, *68*, 537–566.

Lefevre, F., and F. Forget (2009), Observed variations of methane on Mars unexplained by known atmospheric chemistry and physics, *Nature*, *460*, 720–723.

Lemmon, M., et al. (2004), Atmospheric imaging results from the Mars Exploration Rovers: Spirit and Opportunity, *Science*, *306*, 1753–1756.

Leovy, C. B., and Y. Mintz (1969), Numerical simulation of the atmospheric circulation and climate of Mars, *J. Atmos. Sci.*, *26*, 1167–1190.

Lewellen, W. (1977), Use of invariant modeling, in *Handbook of Turbulence*, vol. 1, *Fundamentals and Applications*, pp. 237–280, Plenum, New York.

Lilly, D. K. (1962), On the numerical simulation of buoyant convection, *Tellus*, *14*, 148–172.

Listowski, C., et al. (2011), Solar occultation with SPICAM/UV on board Mars Express: Retrieving aerosol and ozone profiles, paper presented at Fourth International Workshop on Mars Atmosphere Modelling and Observations, Cent. Natl. d'Etud. Spat., Paris, 8–11 Feb.

Määttänen, A., and H. Savijärvi (2004), Sensitivity tests with a 1-dimensional boundary layer Mars model, *Boundary Layer Meteorol.*, *113*, 305–320.

Määttänen, A., et al. (2009), A study of the properties of a local dust storm with Mars Express OMEGA and PFS data, *Icarus*, *201*, 504–516.

Malin, M. C., and K. S. Edgett (2001), Mars Global Surveyor Mars Orbiter Camera: Interplanetary cruise through primary mission, *J. Geophys. Res.*, *106*, 23,429–23,570.

Malin, M. C., et al. (1999), Early views of the Martian surface from the Mars Orbiter Camera of Mars Global Surveyor, *Science*, *279*, 1681–1685.

Martin, P. (1985), Simulation of the mixed layer at OWS November and Papa with several models, *J. Geophys. Res.*, *90*, 903–916.

Martínez, G., F. Valero, and L. Vázquez (2009), Characterization of the Martian Convective Boundary Layer, *J. Atmos. Sci.*, *66*, 2044–2058.

McCleese, D. J., et al. (2007), Mars Climate Sounder: An investigation of thermal and water vapor structure, dust and condensate distributions in the atmosphere, and energy balance of the polar regions, *J. Geophys. Res.*, *112*, E05S06, doi:10.1029/2006JE002790.

Mellon, M. T., B. M. Jakosky, H. H. Kieffer, and P. R. Christensen (2000), High-resolution thermal inertia mapping from the Mars Global Surveyor Thermal Emission spectrometer, *Icarus*, *148*, 437–455.

Mellor, G. (1973), Analytic prediction of properties of stratified planetary surface layers, *J. Atmos. Sci.*, *30*, 1061–1069.

Mellor, G. (1975), A comparative study of curved flow and density-stratified flow, *J. Atmos. Sci.*, *32*, 1278–128.

Mellor, G. (2003), Comments on "Stability of algebraic non-equilibrium second-order closure models" by H. Burchard and E. Deleersnjder [Ocean Modelling 3 (2001) 33–50], *Ocean Modell.*, *5*, 193–194.

Mellor, G., and H. Herring (1973), Survey of mean turbulent field closure models, *AIAA J.*, *11*, 590–599.

Mellor, G., and T. Yamada (1974), A hierarchy of turbulence closure models for planetary boundary layers, *J. Atmos. Sci.*, *31*, 1791–1806.

Mellor, G., and T. Yamada (1982), Development of a turbulence closure model for geophysical fluid problems, *Rev. Geophys.*, *20*, 851–875.

Melnik, O., and M. Parrot (1998), Electrostatic discharge in Martian dust storms, *J. Geophys. Res.*, *103*, 29,107–29,117.

Metzger, S. M., J. R. Carr, J. R. Johnson, T. J. Parker, and M. Lemmon (1999), Dust devil vortices seen by the Mars Pathfinder camera, *Geophys. Res. Lett.*, 26, 2781–2784.

Michael, W. H., Jr., D. L. Cain, G. Fjeldbo, G. S. Levy, J. G. Davies, M. D. Grossi, I. I. Shapiro, and G. L. Tyler (1972), Radio science experiments: The Viking Mars orbiter and lander, *Icarus*, 16, 57–73.

Michaels, T. I. (2006), Numerical modeling of Mars dust devils: Albedo track generation, *Geophys. Res. Lett.*, 33, L19S08, doi:10.1029/2006GL026268.

Michaels, T. I., and S. C. R. Rafkin (2004), Large eddy simulation of atmospheric convection on Mars, *Q. J. R. Meteorol. Soc.*, 130, 1251–1274.

Michaels, T. I., and S. C. R. Rafkin (2008), Meteorological predictions for candidate 2007 Phoenix Mars lander sites using the Mars Regional Atmospheric Modeling System (MRAMS), *J. Geophys. Res.*, 113, E00A07, doi:10.1029/2007JE003013.

Mitrofanov, I. G., et al. (2003), Search for water in Martian soil using global neutron mapping by the Russian HEND instrument onboard the US 2001 Mars Odyssey spacecraft, *Sol. Syst. Res.*, 37, 366–377.

Moeng, C., and J. Wyngaard (1989), Evaluation of turbulent transport and dissipation closures in second-order modeling, *J. Atmos. Sci.*, 46, 2311–2330.

Moeng, C., J. Dudhia, J. Klemp, and P. Sullivan (2007), Examining two-way grid nesting for large eddy simulation of the PBL using the WRF Model, *Mon. Weather Rev.*, 135, 2295–2311.

Monin, A. S., and A. M. Obukhov (1954), Osnovnye zakonomernosti turbulentnogo peremeshivanija v prizemnon sloe atmosfery [Basic laws of turbulent mixing in the atmosphere near the ground], *Trudy Geofiz. inst. AN SSSR*, 24, 163–187.

Monin, A., and A. Yaglom (1975), *Statistical Fluid Mechanics*, MIT Press, Cambridge, Mass.

Moores, J. E., M. T. Lemmon, P. H. Smith, L. Komguem, and J. A. Whiteway (2010), Atmospheric dynamics at the Phoenix landing site as seen by the Surface Stereo Imager, *J. Geophys. Res.*, 115, E00E08, doi:10.1029/2009JE003409.

Moudden, Y., and J. McConnell (2005), A new model for multiscale modeling of the Martian atmosphere, GM3, *J. Geophys. Res.*, 110, E04001, doi:10.1029/2004JE002354.

Murphy, J. R., and S. Nelli (2002), Mars Pathfinder convective vortices: Frequency of occurrence, *Geophys. Res. Lett.*, 29(23), 2103, doi:10.1029/2002GL015214.

Nayvelt, L., P. J. Gierasch and K. H. Cook (1997), Modeling and observations of Martian stationary waves, *J. Atmos. Sci.*, 54, 986–1013.

Newman, C. E., S. R. Lewis, P. L. Read, and F. Forget (2002a), Modeling the Martian dust cycle: 1. Representations of dust transport processes, *J. Geophys. Res.*, 107(E12), 5123, doi:10.1029/2002JE001910.

Newman, C. E., S. R. Lewis, P. L. Read, and F. Forget (2002b), Modeling the Martian dust cycle: 2. Multiannual radiatively active dust transport simulations, *J. Geophys. Res.*, 107(E12), 5124, doi:10.1029/2002JE001920.

Nieuwstadt, F. T. M. (1984), The turbulent structure of the stable nocturnal boundary layer, *J. Atmos. Sci.*, 41, 2202–2216.

Odaka, M. (2001), A numerical simulation of Martian atmospheric convection with a two-dimensional anelastic model: A case of dust-free Mars, *Geophys. Res. Lett.*, 28, 895–898.

Odaka, M., K. Nakajima, S. Takehiro, M. Ishiwatari, and Y. Hayashi (1998), A numerical study of the Martian atmospheric convection with a two-dimensional anelastic model, *Earth Planets Space*, 50, 431–437.

Oyama, V., B. Berdahl, and G. Carle (1977), Preliminary findings of Viking gas-exchange experiment and a model for Martian surface chemistry, *Nature*, 265, 110–114.

Pallman, A. J. (1983), The thermal structure of the atmospheric surface layer on Mars as modified by the radiative effect of Aeolian dust, *J. Geophys. Res.*, 88, 5483–5493.

Pettengill, G. H., and P. G. Ford (2000), Winter clouds over the north Martian polar cap, *Geophys. Res. Lett.*, 27, 609–612.

Pollack, J. B., C. B. Leovy, Y. Mintz, and W. Van Kamp (1976), Winds on Mars during the Viking season: Predictions based on a general circulation model with topography, *Geophys. Res. Lett.*, 3, 479–482.

Pollack, J. B., D. Colburn, R. Kahn, J. Hunter, W. Van Camp, C. Carlston, and M. Wolf (1977), Properties of aerosols in the Martian atmosphere, as inferred from Viking lander imaging data, *J. Geophys. Res.*, 82, 4479–4496.

Pollack, J. B., C. B. Leovy, P. W. Greiman, and Y. Mintz (1981), A Martian general circulation experiment with large topography, *J. Atmos. Sci.*, 38, 3–29.

Pope, S. (2005), *Turbulent Flows*, Cambridge Univ. Press, Cambridge, U. K.

Putzig, N. E., and M. T. Mellon (2007), Apparent thermal inertia and the surface heterogeneity of Mars, *Icarus*, 191, 68–94.

Rafkin, S. C. R. (2003), The effect of convective adjustment on the global circulation of Mars as simulated by a general circulation model, in *Sixth International Conference on Mars, July 20–25, 2003, Pasadena CA* [CD-ROM], *LPI Contrib. 1164*, Abstract 3059.

Rafkin, S. C. R., and T. I. Michaels (2003), Meteorological predictions for 2003 Mars Exploration Rover high-priority landing sites, *J. Geophys. Res.*, 108(E12), 8091, doi:10.1029/2002JE002027.

Rafkin, S. C. R., R. M. Haberle, and T. I. Michaels (2001), The Mars regional atmospheric modeling system: Model description and selected simulations, *Icarus*, 151, 228–256.

Rafkin, S. C. R., T. I. Michaels, and R. M. Haberle (2004), Meteorological predictions for the Beagle 2 mission to Mars, *Geophys. Res. Lett.*, 31, L01703, doi:10.1029/2003GL018966.

Rannou, P., S. Perrier, J.-L. Bertaux, F. Montmessin, O. Korablev, and A. Reberac (2006), Dust and cloud detection at the Mars limb with UV scattered sunlight with SPICAM, *J. Geophys. Res.*, 111, E09S10, doi:10.1029/2006JE002693.

Renno, N. O. (2008), A general theory for convective plumes and vortices, *Tellus*, 60A, 688–699.

Renno, N. O., and J. F. Kok (2008), Electrical activity and dust lifting on Earth, Mars and beyond, *Space Sci. Rev.*, 137, 419–434.

Renno, N. O., M. L. Burkett, and M. P. Larkin (1998), A simple thermodynamical theory for dust devils, *J. Atmos. Sci.*, 55, 3244–3252.

Renno, N. O., A. A. Nash, J. Lunine, and J. Murphy (2000), Martian and terrestrial dust devils: Test of a scaling theory using Pathfinder data, *J. Geophys. Res.*, 105, 1859–1865.

Renno, N. O., A.-S. Wong, S. K. Atreya, I. de Pater, and M. Roos-Serote (2003), Electrical discharges and broadband radio emission by Martian dust devils and dust storms, *Geophys. Res. Lett.*, 30(22), 2140, doi:10.1029/2003GL017879.

Renno, N. O., et al. (2004), MATADOR 2002: A pilot field experiment on convective plumes and dust devils, *J. Geophys. Res.*, 109, E07001, doi:10.1029/2003JE002219.

Renno, N. O., et al. (2009), Possible physical and thermodynamical evidence for liquid water at the Phoenix landing site, *J. Geophys. Res.*, 114, E00E03, doi:10.1029/2009JE003362. [Printed 115(E1), 2010.]

Richardson, M. I., A. D. Toigo, and C. E. Newman (2007), PlanetWRF: A general purpose, local to global numerical model for planetary atmospheric and climate dynamics, *J. Geophys. Res.*, 112, E09001, doi:10.1029/2006JE002825.

Ringrose, T. J., M. C. Towner, and J. C. Zarnecki (2003), Convective vortices on Mars: A reanalysis of Viking Lander 2 meteorological data, sols 1–60, *Icarus*, 163, 78–87.

Rippeth, T. (2005), Mixing in seasonally stratified shelf seas: A shifting paradigm, *Philos. Trans. R. Soc. A*, 363, 2837–2854.

Ristorcelli, J. (1997), Toward a turbulence constitutive relation for geophysical flows, *Theor. Comput. Fluid Dyn.*, 9, 207–221.

Rodi, W. (1987), Examples of calculation methods for flow and mixing in stratified fluids, *J. Geophys. Res.*, 92, 5305–5328.

Rodin, A. V., O. I. Korablev, and V. I. Moroz (1997), Vertical distribution of water in the near-equatorial troposphere of Mars: Water vapor and clouds, *Icarus*, *125*, 212–229.

Ruf, C., N. O. Renno, J. F. Kok, E. Bandelier, M. J. Sander, S. Gross, L. Skjerve, and B. Cantor (2009), The emission of non-thermal microwave radiation by a Martian dust storm, *Geophys. Res. Lett.*, *36*, L13202, doi:10.1029/2009GL038715.

Ryan, J., and R. Lucich (1983), Possible dust devils, vortices on Mars, *J. Geophys. Res.*, *88*, 11,005–11,011.

Savijärvi, H. (1991a), Radiative fluxes on a dustfree Mars, *Contrib. Atmos. Phys.*, *64*, 103–111.

Savijärvi, H. (1991b), A model study of the PBL structure on Mars and the Earth, *Contrib. Atmos. Phys.*, *64*, 219–229.

Savijärvi, H. (1999), A model study of the atmospheric boundary layer in the Mars Pathfinder lander conditions, *Q. J. R. Meteorol. Soc.*, *125*, 483–493.

Savijärvi, H., and J. Kauhanen (2008), Surface and boundary layer modeling for the Mars Exploration Rover sites, *Q. J. R. Meteorol. Soc.*, *134*, 635–641.

Savijärvi, H., and A. Määttänen (2010), Boundary layer simulations for the Mars Phoenix lander site, *Q. J. R. Meteorol. Soc.*, *136*, 1497–1505.

Savijärvi, H., and T. Siili (1993), The Martian slope winds and the nocturnal PBL jet, *J. Atmos. Sci.*, *50*, 77–88.

Savijärvi, H., A. Määttänen, J. Kauhanen, and A.-M. Harri (2004), Mars Pathfinder: New data and new model simulations, *Q. J. R. Meteorol. Soc.*, *130*, 669–683.

Schmidt, D. S., R. A. Schmidt, and J. D. Dent (1998), Electrostatic force on saltating sand, *J. Geophys. Res.*, *103*, 8997–9001.

Schofield, J. T., J. R. Barnes, D. Crisp, R. M. Haberle, S. Larsen, J. A. Magalhaes, J. R. Murphy, A. Seiff, and G. Wilson (1997), The Mars Pathfinder Atmospheric Structure Investigation/ Meteorology (ASI/MET) experiment, *Science*, *278*, 1752–1758.

Segschneider, J., B. Grieger, H. U. Keller, F. Lunkeit, E. Kirk, K. Fraedrich, A. Rodin, and R. Greve (2005), Response of the intermediate complexity Mars Climate Simulator to different obliquity angles, *Planet. Space Sci.*, *53*, 659–670.

Seiff, A., and D. B. Kirk (1977), Structure of the atmosphere of Mars in summer at mid-latitude, *J. Geophys. Res.*, *82*, 4364–4388.

Seiff, A., et al. (1997), The atmosphere structure and meteorology instrument on the Mars Pathfinder lander, *J. Geophys. Res.*, *102*, 4045–4056.

Simpson, J., W. Crawford, T. Rippeth, A. Campbell, and J. Cheok (1996), The vertical structure of turbulent dissipation in shelf seas, *J. Phys. Oceanogr.*, *26*, 1579–1590.

Sinclair, P. C. (1973), The lower structure of dust devils, *J. Atmos. Sci.*, *30*, 1599–1619.

Smith, D. E., et al. (2001), Mars Orbiter Laser Altimeter: Experiment summary after the first year of global mapping of Mars, *J. Geophys. Res.*, *106*, 23,689–23,722.

Smith, M. D., J. C. Pearl, B. J. Conrath, and P. R. Christensen (2001a), Thermal Emission Spectrometer results: Mars atmospheric thermal structure and aerosol distribution, *J. Geophys. Res.*, *106*, 23,929–23,945.

Smith, M. D., J. C. Pearl, B. J. Conrath, and P. R. Christensen (2001b), One Martian year of atmospheric observations by the Thermal Emission Spectrometer, *Geophys. Res. Lett.*, *28*, 4263–4266.

Smith, M. D., et al. (2004), First atmospheric science results from the Mars Exploration Rovers Mini-TES, *Science*, *306*, 1750–1753.

Smith, M. D., M. J. Wolff, N. Spanovich, A. Ghosh, D. Banfield, P. R. Christensen, G. A. Landis, and S. W. Squyres (2006), One Martian year of atmospheric observations using MER Mini-TES, *J. Geophys. Res.*, *111*, E12S13, doi:10.1029/2006JE002770.

Smith, P., et al. (1997), The Imager for Mars Pathfinder experiment, *J. Geophys. Res.*, *102*, 4003–4025.

Sorbjan, Z. (2007), Statistics of shallow convection on Mars based on large-eddy simulations. Part 1: Shearless conditions, *Boundary Layer Meteorol.*, *123*, 121–142.

Souza, E. P., N. Renno, and M. A. F. S. Dias (2000), Convective circulations induced by surface heterogeneities, *J. Atmos. Sci.*, *57*, 2915–2922.

Spiga, A. (2011), Elements of comparison between Martian and terrestrial mesoscale meteorological phenomena: Katabatic winds and boundary layer convection, *Planet. Space Sci.*, in press.

Spiga, A., and F. Forget (2009), A new model to simulate the Martian mesoscale and microscale atmospheric circulation: Validation and first results, *J. Geophys. Res.*, *114*, E02009, doi:10.1029/2008JE003242.

Spiga, A., et al. (2007), Remote sensing of surface pressure on Mars with the Mars Express/OMEGA spectrometer: 2. Meteorological maps, *J. Geophys. Res.*, *112*, E08S16, doi:10.1029/ 2006JE002870.

Spiga, A., F. Forget, S. R. Lewis, and D. P. Hinson (2010), Structure and dynamics of the convective boundary layer on Mars as inferred from large-eddy simulations and remote-sensing measurements, *Q. J. R. Meteorol. Soc.*, *136*, 414–428.

Squyres, S., et al. (2003), Athena Mars rover science investigation, *J. Geophys. Res.*, *108*(E12), 8062, doi:10.1029/2003JE002121.

Sreenivasan, K. (1995), On the universality of the kolmogorov constant, *Phys. Fluids*, *7*, 2778–2784.

Stow, C. D. (1969), Dust and storm electrification, *Weather*, *24*, 134–137.

Stull, R. B. (1976), Internal gravity waves generated by penetrative convection, *J. Atmos. Sci.*, *33*, 1279–1286.

Stull, R. B. (1988), *An Introduction to Boundary Layer Meteorology*, Springer, Dordrecht, Netherlands.

Sukoriansky, S., and B. Galperin (2008), Anisotropic turbulence and internal waves in stably stratified flows (QNSE theory), *Phys. Scr.*, *T132*, 014036.

Sukoriansky, S., B. Galperin, and V. Perov (2005a), Application of a new spectral theory of stably stratified turbulence to atmospheric boundary layers over sea ice, *Boundary Layer Meteorol.*, *117*, 231–257.

Sukoriansky, S., B. Galperin, and I. Staroselsky (2005b), A quasi-normal scale elimination model of turbulent flows with stable stratification, *Phys. Fluids*, *17*, 085107.

Sukoriansky, S., B. Galperin, and V. Perov (2006), A quasi-normal scale elimination model of turbulence and its application to stably stratified flows, *Nonlinear Proc. Geophys.*, *13*, 9–22.

Sutton, J. L., C. B. Leovy, and J. E. Tillman (1978), Diurnal variations of the Martian surface layer meteorological parameters during the first 45 sols at two Viking lander sites, *J. Atmos. Sci.*, *35*, 2346–2355.

Takahashi, Y. O., H. Fujiwara, H. Fukunishi, M. Odaka, Y.-Y. Hayashi, and S. Watanabe (2003), Topographically induced north-south asymmetry of the meridional circulation in the Martian atmosphere, *J. Geophys. Res.*, *108*(E3), 5018, doi:10.1029/ 2001JE001638.

Takahashi, Y. O., H. Fujiwara, and H. Fukunishi (2006), Vertical and latitudinal structure of the migrating diurnal tide in the Martian atmosphere: Numerical investigations, *J. Geophys. Res.*, *111*, E01003, doi:10.1029/2005JE002543.

Taylor, P. A., D. C. Catling, M. Daly, C. S. Dickinson, H. P. Gunnlaugsson, A.-M. Harri, and C. F. Lange (2008), Temperature, pressure, and wind instrumentation in the Phoenix meteorological package, *J. Geophys. Res.*, *113*, E00A10, doi:10.1029/ 2007JE003015.

Taylor, P. A., et al. (2010), On pressure measurement and seasonal pressure variations during the Phoenix mission, *J. Geophys. Res.*, *115*, E00E15, doi:10.1029/2009JE003422.

Tennekes, H., and J. Lumley (1972), *A First Course in Turbulence*, MIT Press, Cambridge, Mass.

Thomas, P., and P. J. Gierasch (1985), Dust devils on Mars, *Science*, *230*, 175–177.

Tillman, J. E., L. Landberg, and S. E. Larsen (1994), The boundary layer of Mars: Fluxes, stability, turbulent spectra, and growth of the mixed layer, *J. Atmos. Sci.*, *51*, 1709–1727.

Toigo, A. D., and M. I. Richardson (2002), A mesoscale model for the Martian atmosphere, *J. Geophys. Res.*, *107*(E7), 5049, doi:10.1029/2000JE001489.

Toigo, A. D., and M. I. Richardson (2003), Meteorology of proposed Mars Exploration Rover landing sites, *J. Geophys. Res.*, *108*(E12), 8092, doi:10.1029/2003JE002064.

Toigo, A. D., M. I. Richardson, S. P. Ewald, and P. J. Gierasch (2003), Numerical simulation of Martian dust devils, *J. Geophys. Res.*, *108*(E6), 5047, doi:10.1029/2002JE002002.

Tyler, D., J. R. Barnes, and R. M. Haberle (2002), Simulation of surface meteorology at the Pathfinder and VL1 sites using a Mars mesoscale model, *J. Geophys. Res.*, *107*(E4), 5018, doi:10.1029/2001JE001618.

Tyler, D., J. R. Barnes, and E. D. Skyllingstad (2008), Mesoscale and large-eddy simulation model studies of the Martian atmosphere in support of Phoenix, *J. Geophys. Res.*, *113*, E00A12, doi:10.1029/2007JE003012.

Tyler, G. L., et al. (1992), Radio science investigations with Mars Observer, *J. Geophys. Res.*, *97*, 7759–7780.

Umlauf, L., and H. Burchard (2003), A generic length-scale equation for geophysical turbulence models, *J. Mar. Res.*, *61*, 235–265.

Umlauf, L., and H. Burchard (2005), Second-order turbulence closure models for geophysical boundary layers. A review of recent work, *Cont. Shelf Res.*, *25*, 795–827.

Umlauf, L., H. Burchard, and K. Hutter (2003), Extending the $k - \omega$ turbulence model towards oceanic applications, *Ocean Modell.*, *5*, 195–218.

VanZandt, T. E. (1982), A universal spectrum of buoyancy waves in the atmosphere, *Geophys. Res. Lett.*, *9*, 575–578.

Villalobos, F. J. (1997), Correction of eddy covariance water vapor flux using additional measurements of temperature, *Agric. For. Meteorol.*, *88*, 77–83.

Vincendon, M., Y. Langevin, F. Poulet, J.-P. Bibring, and B. Gondet (2007), Recovery of surface reflectance spectra and evaluation of the optical depth of aerosols in the near-IR using a Monte Carlo approach: Application to the OMEGA observations of high-latitude regions of Mars, *J. Geophys. Res.*, *112*, E08S13, doi:10.1029/2006JE002845.

Violeau, D. (2009), Explicit algebraic Reynolds stresses and scalar fluxes for density-stratified shear flows, *Phys. Fluids*, *21*, 035103.

Webster, P. J. (1977), The low latitude circulation of Mars, *Icarus*, *30*, 626–649.

Weng, W., et al. (2006), Modelling the Martian boundary layer, paper presented at Second Workshop on Mars Atmosphere Modelling and Observations, Cent. Natl. d'Etud. Spat., Granada, Spain, 27 Feb. to 3 March. [Available at http://www-mars.lmd.jussieu.fr/granada2006/abstracts/Weng_Granada2006.pdf.]

Whiteway, J., M. Daly, A. Carswell, T. Duck, C. Dickinson, L. Komguem, and C. Cook (2008), Lidar on the Phoenix mission to Mars, *J. Geophys. Res.*, *113*, E00A08, doi:10.1029/2007JE003002. [Printed *114*(E3), 2009.]

Whiteway, J., et al. (2009a), Phoenix lidar observations of dust, clouds, and precipitation on Mars, in *Lunar Planet. Sci.*, XL, Abstract 2202.

Whiteway, J. A., et al. (2009b), Mars water-ice clouds and precipitation, *Science*, *325*, 68–70.

Wilcox, D. (1988), Reassessment of the scale-determining equation for advanced turbulence models, *AIAA J.*, *26*, 1299–1310.

Wilson, R. J. (1997), A general circulation model of the Martian polar warming, *Geophys. Res. Lett.*, *24*, 123–126.

Wing, D. R., and G. L. Austin (2006), Description of the University of Auckland global Mars mesoscale meteorological model, *Icarus*, *185*, 370–382.

Wolff, M. J., et al. (2006), Constraints on dust aerosols from the Mars Exploration Rovers using MGS overflights and Mini-TES, *J. Geophys. Res.*, *111*, E12S17, doi:10.1029/2006JE002786.

Wolff, M. J., M. D. Smith, R. T. Clancy, R. Arvidson, M. Kahre, F. Seelos, S. Murchie, and H. Savijärvi (2009), Wavelength dependence of dust aerosol single scattering albedo as observed by the Compact Reconnaissance Imaging Spectrometer, *J. Geophys. Res.*, *114*, E00D04, doi:10.1029/2009JE003350.

Wolff, M. J., R. T. Clancy, J. D. Goguen, M. C. Malin, and B. A. Cantor (2010), Ultraviolet dust aerosol properties as observed by MARCI, *Icarus*, *208*, 143–155.

Wolkenberg, P., D. Grassi, V. Formisano, G. Rinaldi, M. D'Amore, and M. Smith (2009), Simultaneous observations of the Martian atmosphere by Planetary Fourier Spectrometer on Mars Express and Miniature Thermal Emission Spectrometer on Mars Exploration Rover, *J. Geophys. Res.*, *114*, E04012, doi:10.1029/2008JE003216.

Wyngaard, J. (2010), *Turbulence in the Atmosphere*, Cambridge Univ. Press, Cambridge, U. K.

Wyngaard, J., and J. Weil (1991), Transport asymmetry in skewed turbulence, *Phys. Fluids*, A3, 155–162.

Ye, Z. J., M. Segal, and R. A. Pielke (1990), A comparative study of daytime thermally induced upslope flow on Mars and Earth, *J. Atmos. Sci.*, *47*, 612–628.

Zeman, O., and J. Lumley (1979), Buoyancy effects in entraining turbulent boundary layers: A second-order closure study, in *Turbulent Shear Flows*, vol. 1, pp. 295–302, Springer, Berlin.

Zent, A. P., M. H. Hecht, D. R. Cobos, G. S. Campbell, C. S. Campbell, G. Cardell, M. C. Foote, S. E. Wood, and M. Mehta (2009), Thermal and Electrical Conductivity Probe (TECP) for Phoenix, *J. Geophys. Res.*, *114*, E00A27, doi:10.1029/2007JE003052.

Zent, A. P., M. H. Hecht, D. R. Cobos, S. E. Wood, T. L. Hudson, S. M. Milkovich, L. P. DeFlores, and M. T. Mellon (2010), Initial results from the Thermal and Electrical Conductivity Probe (TECP) on Phoenix, *J. Geophys. Res.*, *115*, E00E14, doi:10.1029/2009JE003420.

Zilitinkevich, S., V. Gryanik, V. Lykossov, and D. Mironov (1999), Third-order transport and nonlocal turbulence closures for convective boundary layers, *J. Atmos. Sci.*, *56*, 3463–3477.

Zilitinkevich, S., T. Elperin, N. Kleeorin, and I. Rogachevskii (2007), Energy- and flux-budget (EFB) turbulence closure model for stably stratified flows. Part I: Steady-state, homogeneous regimes, *Boundary Layer Meteorol.*, *125*, 167–191.

Zurek, R. W., and S. E. Smrekar (2007), An overview of the Mars Reconnaissance Orbiter (MRO) science mission, *J. Geophys. Res.*, *112*, E05S01, doi:10.1029/2006JE002701.

B. Galperin, College of Marine Science, University of South Florida, St. Petersburg, FL 33701, USA. (bgalperin@marine.usf.edu)

S. E. Larsen, Risø, National Laboratory, Technical University of Denmark, DK-4000 Roskilde, Denmark. (sola@risoe.dtu.dk)

S. R. Lewis, Department of Physics and Astronomy, Open University, Walton Hall, Milton Keynes MK7 6AA, UK. (sf.r.lewis@open.ac.uk)

A. Määttänen, LATMOS, Université de Versailles Saint Quentin, Guyancourt, F-78280 France. (anni.maattanen@latmos.ipsl.fr)

A. Petrosyan, Space Research Institute, Russian Academy of Sciences, Profsoyuznaya 84/32, Moscow 117997, Russia. (apetrosy@iki.rssi.ru)

P. L. Read and L. P. H. T. Rogberg, Atmospheric, Oceanic and Planetary Physics, University of Oxford, Parks Road, Oxford OX1 3PU, UK. (p.read1@physics.ox.ac.uk; p.rogberg1@physics.ox.ac.uk)

N. Renno, Department of Atmospheric, Oceanic and Space Sciences, Space Research Building, University of Michigan, 2455 Hayward St., Ann Arbor, MI 48109-2143, USA. (nrenno@umich.edu)

H. Savijärvi, Department of Physics, University of Helsinki, FI-00014 Helsinki, Finland. (hannu.savijarvi@helsinki.fi)

T. Siili, Earth Observation, Finnish Meteorological Institute, PO Box 503, FI-00101 Helsinki, Finland. (tero.siili@fmi.fi)

A. Spiga, LMD, Université Pierre et Marie Curie, F-75252 Paris, France. (spiga@lmd.jussieu.fr)

A. Toigo, Johns Hopkins University Applied Physics Laboratory, Laurel, MD 20723, USA. (anthony.toigo@jhuapl.edu)

L. Vázquez, Departamento de Matemática Aplicada, Facultad de Informática, Universidad Complutense de Madrid, E-28040 Madrid, Spain. (lvazquez@fdi.ucm.es)